A study of two-dimensional superconductivity at oxide interfaces using waveguide resonators

Saglam, Y.G.

DOI
10.4233/uuid:000cb5bd-28eb-45c9-b0e8-329ca4b5a2cd

Publication date
2023

Document Version
Final published version

Citation (APA)
Saglam, Y. G. (2023). *A study of two-dimensional superconductivity at oxide interfaces using waveguide resonators*. [Dissertation (TU Delft), Delft University of Technology]. https://doi.org/10.4233/uuid:000cb5bd-28eb-45c9-b0e8-329ca4b5a2cd

A Study Of Two-dimensional Superconductivity At Oxide Interfaces Using Waveguide Resonators

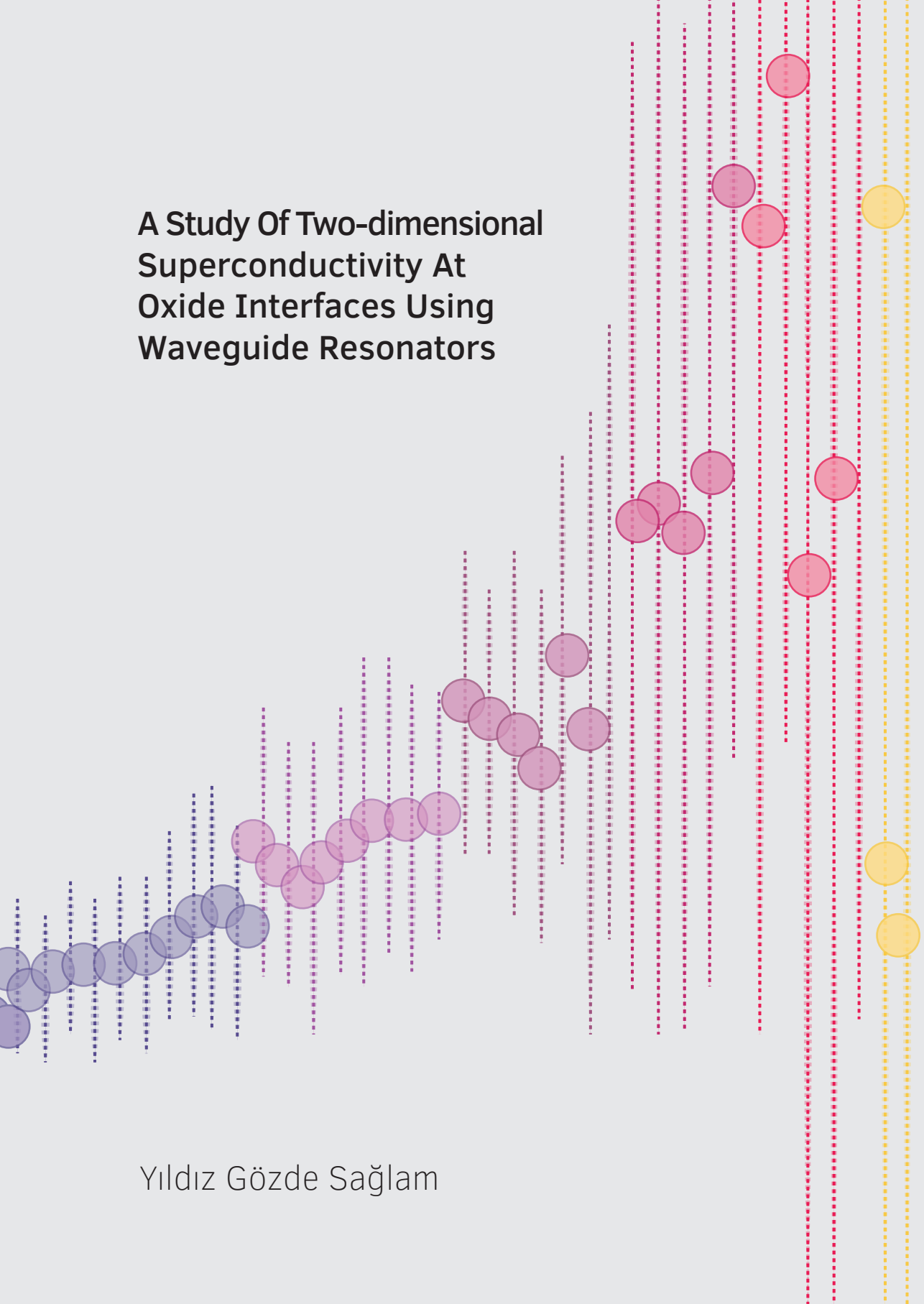

Yıldız Gözde Sağlam

A STUDY OF TWO-DIMENSIONAL SUPERCONDUCTIVITY AT OXIDE INTERFACES USING WAVEGUIDE RESONATORS

Dissertation

for the purpose of obtaining the degree of doctor
at Delft University of Technology,
by the authority of the Rector Magnificus Prof. dr. ir. T.H.J.J. van der Hagen,
chair of the Board for Doctorates,
to be defended publicly on
Wednesday 25 October 2023 at 12:30 o'clock

by

Yıldız Gözde SAĞLAM

Master of Science in Micro and Nanotechnology,
Middle East Technical University, Turkey
born in Ankara, Turkey.

This dissertation has been approved by the promotors.

Composition of the doctoral committee:

Rector Magnificus,	chairperson
Prof. dr. G.A. Steele,	Delft University of Technology, promotor
Prof. dr. A.D. Caviglia ,	Delft University of Technology, University of Geneva, promotor
Independent members:	
Prof. dr. H.S.J. van der Zant	Delft University of Technology
Prof. dr. P.G. Steeneken	Delft University of Technology
Dr. M. Scheffler	Universität Stuttgart, Germany
Dr. W. Loeffler	Leiden University
Prof. dr. Y.M. Blanter	Delft University of Technology, reserve member

Keywords: LAO/STO complex oxides, electronic properties, superconductivity, planar hall effect, coplanar waveguide resonators.

Printed by: Ipskamp Printing, Enschede

Front & Back: The illustration of the superconducting order parameters as a function of external effects. It is inspired from measurement data and designed by Dr. Grazia Tona.

Casimir Series 2023-29

ISBN 978-94-6473-227-6

An electronic version of this dissertation is available at
`http://repository.tudelft.nl/`.

To my father, who would have been happy and proud

CONTENTS

1

INTRODUCTION AND THEORETICAL BACKGROUND

In this chapter, we will provide a broad overview of the properties of $LaAlO_3/SrTiO_3$ interfaces placed along distinct crystallographic directions, such as (001) and (111). We start by mentioning the fundamental characteristics of the well-studied (001)-LAO/STO interface. After that, we will explain the fundamental properties of the (111)-oriented $LaAlO_3/SrTiO_3$ interface, which hosts a conductive interface with exotic behaviors. We will explain the calculation of the superfluid density by using the parameters of a coplanar waveguide resonator. Lastly, an outline of this thesis will be presented.

1

Complex oxides are materials consisting of an oxygen atom and two other metals, usually transition metals, which can then be called a transition metal oxide. Such materials exhibit exciting properties due to the coupling of the electronic charge with its spin and orbital, and the lattice degrees of freedom. The oxide's heterostructures are used in a variety of applications, including computer technology, optoelectronics, sensors, artificial intelligence, data storage, and quantum computing [1]. The possibility of creating artificially engineered materials by growing them at the atomic level is a remarkable opportunity for the study of condensed matter physics. The techniques of growing such materials allow combining various oxide materials to obtain a heterostructure displaying unexpected novel phenomena. The interplay between the degrees of freedom, charge, lattice degrees, spin, and orbitals, yields emerging properties in complex oxides such as high-temperature superconductivity [2], ferroelectricity [3], colossal magnetoresistance [4], and multi ferroelectric behaviour [5]. Among many possible areas of application, complex oxides could be an alternative to silicon-based devices and even constitute advances in certain areas such as electronics and spintronics [6]. It has been already shown that such materials can be used in many different applications, such as data storage, logic devices (hybrid CMOS devices), solar cells, and quantum-based technologies [1, 7, 8]. Among many of the heterostructures, the $LaAlO_3$ and $SrTiO_3$ complex oxide has become one of the most studied systems over the last decades. Almost twenty years ago, Hwang *et al.* showed the possibility of growing $LaAlO_3$ complex oxide on a well-known $SrTiO_3$ material, which brings about a conductive interface [9]. This interface attracted a great deal of attention due to its unexpected novel properties such as superconductivity [10, 11], spin–orbit coupling [12, 13], and ferromagnetism [14, 15]. The superconductivity of the 2D electron system can be modulated by the application of an electric field [16, 17, 18, 19]. This exciting opportunity to modulate the behavior of a superconducting gas allows exploring many different aspects of oxide electronics [20, 21, 22]. Gate tunable superconductivity has been studied for many years and its behavior and origin are still a topic of discussion in the oxide community [23, 24, 25, 26, 27].

These unexpected properties of such interfaces have been studied in over a hundred research papers by using diverse fabrication techniques and by the design of devices such as traditional hall-bars [28], field effect devices [29], SQUIDs [30, 31, 32], and Josephson junctions [33, 34]. One of the good ways to study the superconductivity of a two-dimensional gas is to implement high-frequency resonant circuits at the interface. This can be achieved by making resonators in the radio-frequency regime that include current flowing through the interface. The information about the superfluid density can be extracted from their resonance frequency, providing information that is very difficult to obtain using conventional transport measurements. In the following sections, we will provide a basic introduction to the materials we work within this thesis and the concepts behind superconducting resonators.

1.1. PROPERTIES OF STRONTIUM TITANIUM OXIDE

Here, we will briefly present the fundamental properties of a (001)-oriented $SrTiO_3$ substrate. As shown in Fig. 1.1(a), it has a cubic perovskite structure with a lattice constant of 3.9 Å and is a member of the $Pm\bar{3}m$ space group. The form of $SrTiO_3$ crystal structure consists of alternating planes which are SrO and TiO_2 planes in bulk form. It has a non-polar crystal structure and shows non-magnetic behavior in its bulk form. As the temperature goes down, a cubic to tetragonal structural phase transition occurs around 105 K due to anti-phase rotation of TiO_6 octahedra [35, 36]. As a consequence of this transition, the system goes from a four-fold to a two-fold degenerate state. A structural transition can also happen due to chemical doping, stress, and pressure on the material [37]. At room temperature, STO is an insulating material with a 3.25 eV indirect band gap with paraelectric behavior. In cubic structure form, the Ti atom is surrounded by six oxygen atoms, namely TiO_6 octahedra. The interaction between the Ti and the oxygen atom is stronger than the interaction between two oxygen atoms. Therefore, there is a repulsion between the Ti and O atoms which naturally translates to the crystal field. This crystal field splits the Ti *3d* orbitals into two parts: t_{2g} orbitals and e_g orbitals, which is shown in Fig.1.1 (b). The energy difference between these two sets is ≈ 2 eV and the t_{2g} is located at the lower energy state as composed of three degenerate orbitals as d_{xy}, d_{xz} and d_{yz}. A few decades ago, it was discovered that extra electrons can be added to the *3d*-orbitals by different methods, such as composition change, electron doping, and oxygen removal from the bulk STO material. As a result of adding electrons, the orbitals can have a mixed state which plays a critical role in the physics of STO material. For instance, STO can become a good conductor as a consequence of those changes. The ability to have mixed states by different methods opens up many possibilities for bulk-STO and STO-based heterostructures.

In 1964, Schooley and his colleague announced the superconductor behaviour in the semiconductor STO which marked itself being the first oxide insulator to be superconducting in history [40]. In addition, STO has been found superconductor with extremely low density, with a carrier concentration of $5.5 * 10^{17}$ cm^{-3}. A few years later, Koonce *et al.* published extended data sets showing that the transition temperature of the superconductivity can be tuned by changing the carrier concentration of the material, and follows a 'dome shape'. As is shown in Fig. 1.1 (c), there is a non-monotonic dependence of the critical temperature, which has the highest value around ≈ 450 mK [38]. In bulk form, STO is a paraelectric material. It can change to a ferroelectric or even quantum paraelectric as its temperature decreases. With decreasing temperature, the relative permittivity of the crystal steadily increases from 300 to 20000. At 4K, ϵ saturates around 20000, which is a signature of an intrinsic quantum paraelectric state [41]. Quantum paraelectricity occurs where or when the ferroelectric fluctuations are stabilized by quantum fluctuations. In Figure 1.1 (d), we show the behavior of the dielectric constant of STO as a function of an electric field at various temperatures. For all values of the temperature, the electric field has an effect on the dielectric response. The largest change due to the bias voltage is observed at 4.4 K temperature. $SrTiO_3$ exhibits high-temperature superconductivity, ferroelectricity and quantum paraelectricity under certain conditions. In addition, it is widely used as a substrate for many thin film heterostructures, such as LAO/STO, LTO/STO, $GdTiO_3$, and $NdTiO_3$, due to its convenient

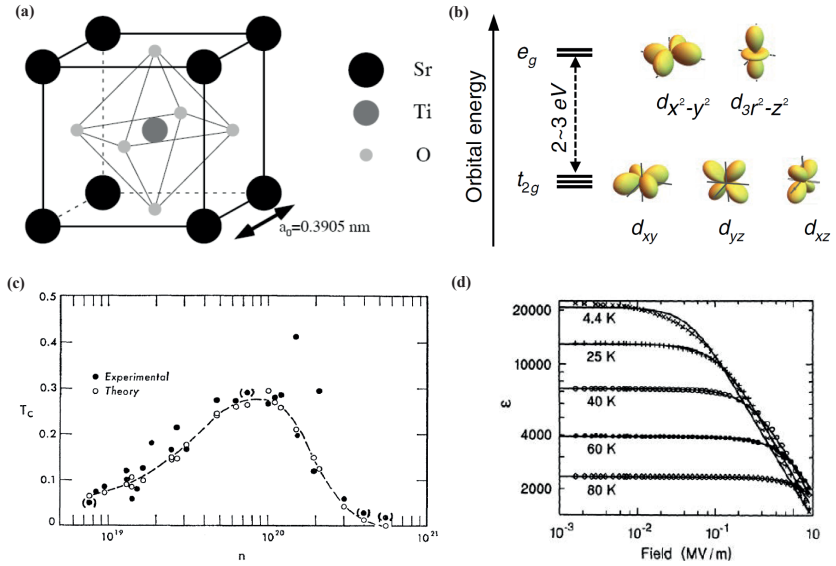

Figure 1.1: (a) Crystal structure of $SrTiO_3$ unit cell. A representation of (001)-oriented STO crystal structure where Ti atom is at the center. The lattice parameter is 0.39 nm. There are 5 atoms per unit cell, which consists of 1 Sr^{+2}, 1 Ti^{+4} and 3 O^{-2} . (b) Schematic of *+3d* orbitals of Ti atom which is seperated by 2 *eV*. Orbitals split as two sets: e_g and t_{2g} due to crytal field. (c) Superconducting transition temperature of bulk $SrTiO_3$ as a function of carrier density, including experimental and theoretical work. The figure is adapted from Ref. [38]. (d) Change in the relative permittivity under the imposition of an electric field for various temperatures. The figure is adapted from Ref. [39].

lattice parameter.

1.2. SUMMARY OF THE PROPERTIES OF A (001)-$LaAlO_3$/$SrTiO_3$ INTERFACE

Nearly two decades ago, Ohtomo and Hwang discovered a conductive two-dimensional system at the interface of $LaAlO_3$/$SrTiO_3$ transition metal oxides [9]. Over the years, countless studies have been reported related to this interface as it displays novel emergent phenomena, such as superconductivity and Rashba spin-orbit coupling. Here, we will try to give a short overview of the properties of this interface, mostly from an electronic correlation perspective. For the $LaAlO_3$/$SrTiO_3$ interface, two different formations can occur, depending on the termination of the STO substrate material. The termination of the substrate plays a critical role in the stacking mechanism, as shown in Figure 1.2. While $SrTiO_3$ is a combination of charge neutral planes $LaAlO_3$ is made up of charged layers like AlO (+1) and LaO (-1). More explicitly, the interface can occur in between two different stackings of ionic planes, such as $(TiO_2)-(LaO)$ and $(SrO)-(AlO_2)$. The very first study of LAO/STO complex oxide shows that the metallicity of the interface depends on

the termination of the STO substrate material, and this statement still holds well [9]. It has been proven that the interface at the $(AlO_2)^-/(SrO)^0$ stacking combination shows no conductivity. In contrast, the interface in between $(LaO)^+/(TiO_2)^-$ shows conductivity and sets criteria for having a conductive interface at LAO/STO complex oxides [16]. When two materials with different polar characteristics are combined, a polar catastrophe is observed due to the diverging electric potential. In order to avoid a polar catastrophy, a charge reconstruction mechanism takes place, which depends on the interface as presented in Figure 1.2. For the TiO_2 terminated STO substrate, the system is stabilized by moving one-half of an electron per unit cell, which travels from the TiO_4 layer [42]. For the SrO terminated substrate, one-half of an electron moves from SrO layer which causes there to be an insulating interface. Another important parameter to obtain a conductive interface is the thickness of the thin film. The interface exhibits conductive behavior if a certain layer of thin film is grown on the substrate material. The critical layer thickness to obtain a conductive interface was reported to be 4 u.c. on 20006 [43]. In addition to a polar catastrophe, there are other possible mechanisms to obtain a conductive interface. One of them is creating oxygen vacancies, which dope the bulk STO material [44]. In the case of an LAO/STO structure, this mechanism is related to the growth conditions of the oxide, such as the oxygen partial pressure and the temperature of the growth process [45, 46]. For instance, one can reduce the oxygen concentration by a post-annealing process, which has been a common technique over the years [47]. There are many other ways to create an extra electron charge at the interface to obtain a conductive two-dimensional interface, but they are outside the scope of this thesis. Interested readers can consult the extensive review [37]. $LaAlO_3$ is a rhombohedral perovskite structure with a lattice constant of 3.79 Å. It is a robust band insulator with a 5.6 eV band gap and a has a polar character. Due to the fact that none of its cations (Al *3s-3p*, +La *5d* states) can access a mixed state, LAO preserves its behavior as an insulator, where electron states associated with defects remain strongly localized. Reyren *et al.* presented the superconductive behavior at the interface which is studied by transport measurements [49]. The electron gas condenses into a two-dimensional superconducting state around $\approx$ 200 mK. In Figure 1.3 (a), the $I-V$ measurements show that above 190 mK, the system leaves its superconducting state and becomes insulating. Moreover, they proved that the application of a magnetic field could suppress the superconductivity at the interface. Later, Caviglia *et al.* proved the possibility of tuning the carrier density at the interface by applying a gate voltage [11] via back gate geometry, which was the first report on this topic. As shown in Fig. 1.3 (b), the system becomes an insulator when the sheet resistance reaches the value 4.5 kΩ. In addition, the transition temperature of the two-dimensional electron gas can be modulated by applying an electric field, which has been reported in different studies [50, 51, 52]. As is shown in Fig. 1.3 (c), T_c has a dome shape as a function of the back-gate voltage and can be tuned up to 300 mK. In the region of large negative voltages, R_{sheet} and T_c both increase, but in the region of large positive voltages, both decrease. This diagram reveals a clear picture of the behaviour of quantum phase transition dependence of the carrier density of the system. The behaviour of the interface is dominated by the Ti *3d* orbitals. During the composition of the interface, a tetragonal crystal field leads to degeneracy of the orbitals by lifting d_{xy} from the d_{xz}, d_{yz} bands. As the heavier d_{xy} band is pushed to a lower energy, the lighter

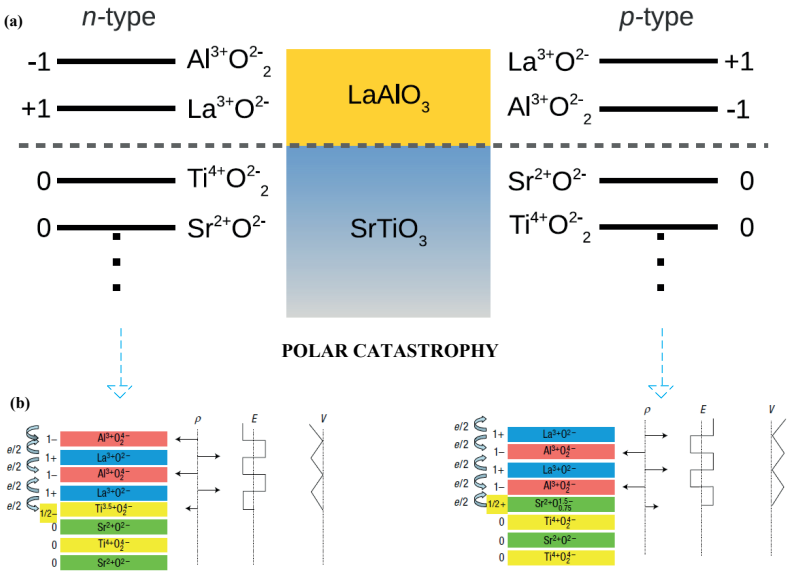

Figure 1.2: (a) Schematic representation of stacking planes for LAO and STO material with a display of stacking layers and the resulting complex oxides. LaO^{+} / $(TiO_2)^{-}$ displays n-type conductivity (conductive interface). $(AlO_2)^{-}$ / $(SrO)^{0}$ displays p-type conductivity (insulating interface). Adapted from the Ref. [48]. (b)The resulting polar catastrophe and electronic reconstruction at the interface brings about a net zero electric field and non-diverging potential.

orbitals stay at a higher energy level. In the ground state, all electrons are expected to remain in the d_{xy} orbital. Studies have shown that the application of an electric field will have an impact on the orbital contribution and Fermi level. The addition of new carriers to the system will raise the Fermi energy above the critical density which coincides with the peak of the superconducting transition temperature. Joshua *et al.* experimentally showed that the population of the different symmetry bands will occur at the universal carrier density value [53]. The superconductivity of (001)-LAO/STO has been studied by using various techniques of measurement and devices over the last decade. The findings of these studies have brought about fruitful scientific discussions about the nature of the pairing mechanism at the interface. LAO/STO interface shows exclusive magneto-transport properties like gate tunable spin-orbit coupling [12, 54]. The large electrostatic tunability of the magnetoconductance is never observed in its constituent materials. In 2010, Caviglia *et al.* report that at the (001)-LAO/STO interface, the breaking of the inversion symmetry causes a strong rashba spin–orbit interaction and its magnitude can be tuned by applying an external field [55, 32].

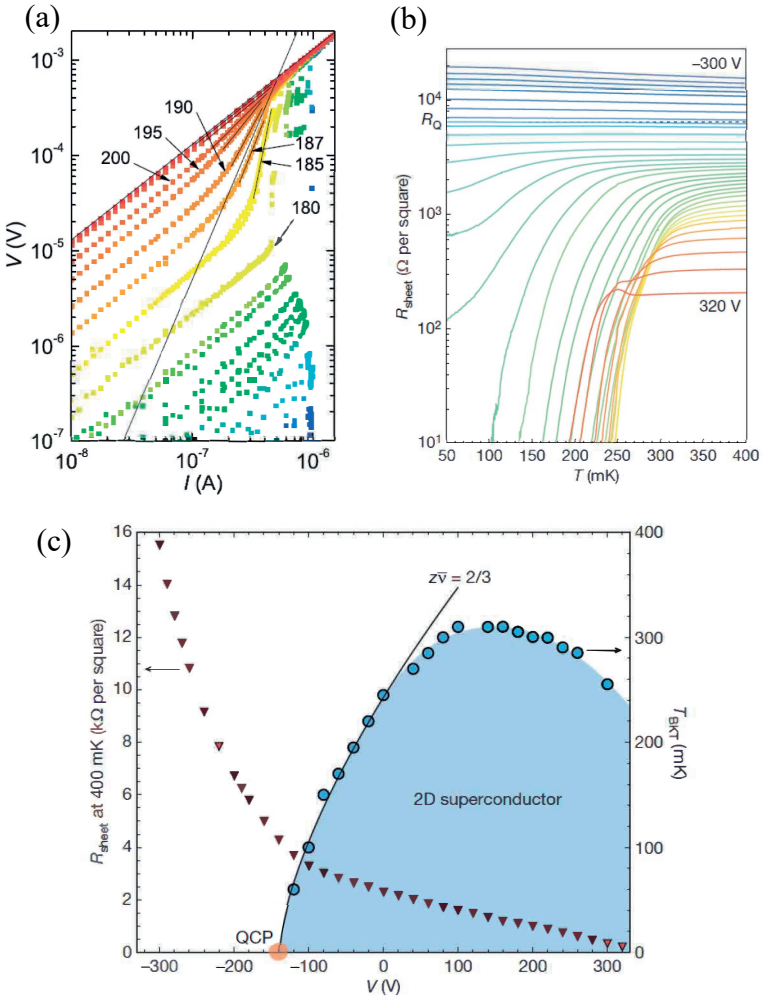

Figure 1.3: Electronic properties of (001)-LAO/STO interface. (a) $V(I)$ characteristics of 8 u.c. LAO/STO heterostructure on a logarithmic scale. The color code is blue 30 mK – red 300 mK. The numbers belong to the indicated curves. Two long black lines show that T_{BKT} is between 187–190 mK. Adapted from the reference [49]. (b) Sheet resistance is plotted as a function of temperature for gate voltages from -300 to 300 V. The dashed line represents the critical sheet resistance value $R_c \approx 4.5$ kΩ. (c) Electronic phase diagram of the LAO/STO interface. On the left side, normal state sheet resistance, and on the right side, T_{BKT} is plotted as a function of the gate voltage. Blue dots indicate the superconducting phase diagram. Adapted from the reference [11].

1

1.3. (111) ORIENTED COMPLEX OXIDES

Perovskites with ABO_3 chemical form display different stacking layers for (001), (110), (111) crystallographic directions [56, 57, 58]. Over the last decade, the attention given to the crystallographic directions of the (110) and (111) transition metal oxides has increased due to their intriguing properties [59]. Herranz *et al.*. showed the possibility of having a conductive interface with high mobility for (110) and (111) LAO/STO complex oxides with distinct lattice structures above a critical thickness of the growth of the LAO layer [58]. Since then, the properties of (110) and (111) oriented interfaces have been studied with electronic and magnetic measurements [60, 61, 62]. In the present thesis, we focus on the (111)-oriented $LaAlO_3/SrTiO_3$, and therefore we will provide a short summary of the properties of this interface. Prior to that, we will explain the (111)-$SrTiO_3$ material as it has a direct impact on the behavior of the interface.

1.3.1. (111)-$SrTiO_3$

The stacking layer of a (111)-oriented $SrTiO_3$ crystal consists of Ti (+4) and SrO_3(−4) alternating layers and show polar characteristics. The bilayer form of Ti^{+4} cations forms a honeycomb lattice structure as displayed in Fig. 1.4 (b). For (111)-STO, the Ti *3d* orbitals are degenerate at the point γ and show equal projections in the z-direction. It has been shown that three t_{2g} bands have the same effective mass, suggesting that quantum confinement will not drive a significant orbital polarization at a possible two-dimensional interface [63]. Thus, it is necessary to mention that the surface orientation of bulk-STO has an important role in the orbital ordering.

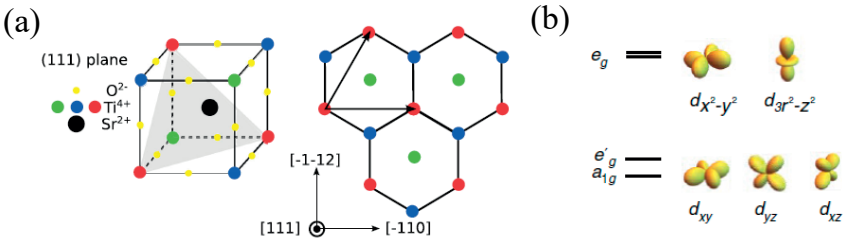

Figure 1.4: (a) Schematic representation of cubic (111)-oriented STO unit cell and (111) orientation is indicated by the gray plane. Arrows are shown for in-plane [$\bar{1}$10] and [$\bar{1}\bar{1}$2] crystallographic directions. Titanium atoms are presented in different colors, which imply different planes. This figure is adapted from [63]. (b) Representation of Ti +*3d* orbitals subband for (111) $SrTiO_3$ substrate. The t_{2g} splits into two: a_{1g} and $e_g^{'}$, which have similar energy levels and are both representative for d_{xy} from d_{xz}, d_{yz} bands. This figure is adapted from [64].

Ti *3d* orbitals exhibit different behaviors for each crystallographic direction. Furthermore, the [$\bar{1}$10] and [$\bar{1}\bar{1}$2] directions leads to a different Fermi surface for the $SrTiO_3$ substrate. The unreconstructed surface could be an interesting platform for the quest for new electronic states and macroscopic properties at the oxide surface due to its hexagonal symmetry [65].

1.3.2. EMERGENT PHENOMENA AT (111)-LAO/STO INTERFACE

A conductive interface was observed when a 9 unit cell of $LaTiO_3$ thin film was grown on a (111)-oriented $SrTiO_3$ substrate by Herranz *et al.*. Since this discovery, the interface has received great attention for its fascinating structural and electronic properties due to its displaying a six-fold symmetry with a superconducting two-dimensional electron gas (2DEG). The appearance of a 2DEG with hexagonal symmetry makes it a system distinct from the (001)-oriented LAO/STO interface which has been studied extensively. In addition, in the (111) direction, both of the perovskites are polar yet still exhibit a conductive interface. (111)-$LaAlO_3$ material has alternating stacking layers of LaO_3^{-3} and AlO^{+3} which is represented in Fig. 1.5 (a). The electronic reconstruction at the interface results in transferring 0.5 e/ $\sqrt{3}$ to Ti^{+4} layer. The electron density extends further into the STO substrate with similar occupancy due to having complementary energy levels [64]. This behavior is different than (001)-LAO/STO as it is more localized and the energy levels of the orbitals are distinctly separated. The interface exhibits clear two-dimensional metallic behaviour and superconducting behaviour below ≈ 120 mK as shown in Fig. 1.5 (b). [66, 67] In addition to that,the critical temperature of the 2DEG is impacted by the thickness of the LAO layer. In Fig. 1.5 (b), it can be seen that the value of T_c is not significantly affected by the level of doping of a system. In addition, it can be concluded that the transport occurs through two sets of electron-like subbands and the carrier density of one of the sets shows a non-monotonic dependence on the conductance of the sample. At a low level of filling, only the first subband is populated and contributes to the transport properties. At a high level of filling, the second subband set starts to contribute and band inversion takes place between the two subbands of t_{2g} due to onsite Coulomb interactions. For both cases, the total carrier density stays constant due to self-consistent Fermi level renormalization. The critical temperature of a (111)-LAO/STO interface is non-monotonic in the applied gate voltage.

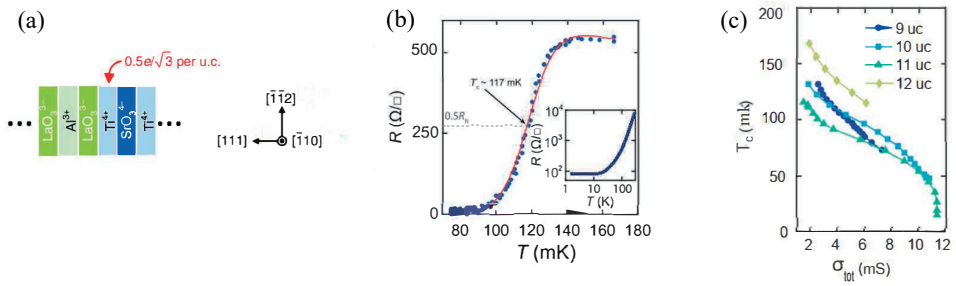

Figure 1.5: (a) The representation of alternating planes for LAO and STO oxides with [1̄10] and [1̄1̄2] directions indicated. This figure is adapted from [64]. (b) The sheet resistance response as a function of temperature with an inset showing the transition down to 1.5 K. Note that this measurement was done with an applied back gate voltage of 30 V. This figure is adapted from [66]. (c) The critical temperature versus sheet conductance for various thicknesses of the LAO layer. This figure is adapted from [68].

Rout *et al.* experimentally showed the link between superconductivity and the behaviour of the spin–orbit coupling in a 14 u.c. LAO/STO interface [67]. They found that the maximum values of the spin–orbit coupling and energy happen at the same voltage where the maximum of T_c was observed. These studies were the first reports about the

111 LAO/STO interface in which the possibility of tuning the system's properties by the application of an electric field was presented. The system hosts superconductivity and spin–orbit coupling with hexagonal symmetry, which brings new possibilities to engineer emerging properties with the complex oxides.

1.4. USING RADIO-FREQUENCY TECHNIQUES FOR MEASURING SUPERFLUID DENSITY IN COMPLEX OXIDES

Superconducting resonators are widely used in various areas of application, such as kinetic inductance detectors, SQUIDs, and qubits. They are fundamental building blocks for quantum electric circuits and can be used as readouts, for coupling, or for detecting information [69]. Previous studies showed that superconducting transmission lines could be used for the direct measurement of the superfluid density parameter. Coplanar waveguide resonators are ideal tools for probing the exotic electronic properties of the LAO/STO interface. In this section, we will explain the use of a coplanar waveguide resonator to measure the superconducting order parameters, in particular, the superfluid density. In this thesis, we study the properties (electronic) of the two dimensional superconducting gas by fabricating coplanar waveguide resonators at the interface itself. The parameter measured by the resonator is the resonance frequency of the transmission line, which is dependent on the capacitance (C) and the inductance (L):

$$f = \frac{1}{2\pi\sqrt{LC}} \tag{1.1}$$

The capacitance depends on the geometrical parameters and the permittivity of the material. Superconducting transmission lines can often have large kinetic inductance contributions, in LAO/STO particular this can be often dominant over geometric inductance. Therefore, the kinetic energy of the Cooper pairs can be studied by the inductance parameter of the resonators. In other words, the calculation of the kinetic inductance can give direct information about the superconducting ground state of the material. The superconducting transmission lines follow an analytic expression for the calculation of the kinetic inductance, which was presented by Watanabe *et al.*in 1994 [70]. In this technique, if the thickness of the superconducting layer of the material is much less than the magnetic penetration depth (the London penetration depth), then the kinetic inductance is enlarged and dominates the magnetic (geometric) inductance. In other words, the contribution of the magnetic inductance to the total inductance could be negligible for superconducting materials. Using the method of conformal mapping, we can calculate the capacitance and inductance of the resonator as follows.

$$C' = 4\varepsilon_0\varepsilon_{\text{eff}}\frac{K(k_0)}{K(k_0')} \ , \ L_g' = \frac{\mu_0}{4}\frac{K(k_0')}{K(k_0)} \tag{1.2}$$

where

$$k_0 = \frac{W}{W+2S} \ , \ k_0' = \sqrt{1-k_0^2} \ , \ \varepsilon_{\text{eff}} = \frac{\varepsilon_r - 1}{2} \ ,$$

$K(x)$ is the complete elliptic integral of the first kind, ε_0 is the vacuum permittivity, ε_r is the dielectric constant of the substrate, and μ_0 is the vacuum permeability. In addition, W is the width of the central strip and S is the gap between the central and ground strip, while ε_{eff} is the effective permittivity of the transmission line. The kinetic inductance of the resonator can be extracted from the measured resonance frequency parameter by Equation 1.1. Subsequently, the superfluid density can be calculated as:

$$L_k = \frac{m_e}{dWq^2n} \tag{1.3}$$

where m_e is the effective mass, $q(=2e)$ is the charge, and n is the planar density of the Cooper pairs, W is the width of the resonator and d is the thickness of the superconductor. For two-dimensional superconductors, n denotes the superfluid density parameter. So, the equation will be

$$L_k = \frac{m^*}{wq^2}\frac{1}{\eta_s} \tag{1.4}$$

In addition to η_s, the Pearl length parameter can also be explained by the following expression:

$$\Lambda = 2W\frac{L_k}{\mu_0}. \tag{1.5}$$

The direct relation between the resonance frequency and the density of the Cooper pairs can be expressed by

$$f_m = \frac{m}{2l}\sqrt{\frac{K(k_0')}{K(k_0)}\frac{Wq^2}{4m_e\varepsilon_0\varepsilon_{\text{eff}}}}\sqrt{n} \tag{1.6}$$

In this thesis, we will use this technique to calculate the superconducting order parameters for the LAO/STO interface. These measurements could reveal information about the superconducting state under an external field without breaking the superconductivity. We aim to design embedded superconducting waveguide resonators at the interface whose resonance frequency can be tuned by electrostatic gating, and reveal the change of the 2DES' superfluid density through a large change of its kinetic inductance.

1.5. OUTLINE OF THIS THESIS

This thesis aims to bring about a new understanding of this topic by measuring the properties of the interface with a new kind of device. With this motivation, we conducted resonator studies of (001) and (111) LAO/STO interfaces. In addition, we have explored the magnetic properties of (111)-LAO/STO by applying an in-plane magnetic field. The structure of this thesis is as follows. Chapter 1 provides a general and short overview of the properties of the LAO/STO interface for different crystallographic directions. In addition, it explains the technique to calculate the superconducting state parameters from resonance measurements. In Chapter 2, we explain the experimental techniques to realize quantum devices with complex oxides, and explain the fundamental fabrication techniques which were used in this work. Then, we will present the measurement setup for both the transport and radio-frequency measurements. In Chapter 3, we explain the implementation of the resonators at the interface of (001)-LAO/STO. The gate tunability of the superconductivity of the 2DEG is demonstrated by the resonator response parameter. We present the electronic phase diagram as a function of the electric field and temperature, where both have a non-monotonic dome shape. In Chapter 4,we will show the extensive study of planar hall effect and anomalous planar hall effect which is tunable by means of applying electric field for (111)-LAO/STO interface. In Chapter 5, we investigate the superfluid density behaviour of the (111)-oriented LAO/STO interface by using radio-frequency measurement techniques.

2

EXPERIMENTAL METHODS

Here, we present fundamental fabrication techniques to release coplanar waveguide resonators at the interface of complex oxides. The challenges and tricks of implementting these devices at the material surface will be explained in detail. Even though the set-up of the assembly of the device for making the measurements will vary for each chapter, the specifics of the packaging of the device for combined DC-transport and microwave measurements are illustrated in detail in this chapter. Lastly, we will explain the details of microwave measurements set-up including the dilution fridge and room temperature set-up.

2.1. INTRODUCTION

In LAO/STO interfaces, a two dimensional superconducting gas is present at the interface of two insulating materials. Due to the nature of heterointerfaces, where the two dimensional superconducting gas lies between two materials, only certain fabrication techniques can be used to place the device at the interface. It is challenging to place a device at the interface without creating any unwanted impact on the substrate material. Until now, LAO/STO interfaces have been studies by various type of devices such as Hall bars, Josephson junctions, and SQUID sensors [33, 71]. Even though advancements in fabrication techniques accelerated over the last decades, only certain fabrication techniques and device designs were used for interfaces. The reason behind is essentially the nature of transition metal oxides and their complex interfaces. There are two different methods to fabricate devices directly at the interface of complex oxides. One of them is the hard-mask technique, which is essentially implementing a patterning on the device prior to the growth of the LAO layer. Another one is starting the fabrication process after the second oxide layer growth is completed. In the work reported in this thesis, we prepared all the presented devices with the top-to-bottom fabrication method, i.e., after the material growth is finished. Even so, we would like to mention that we tried to place devices with the hard-mask technique but obtained better results with the top-to-bottom approach, e.g., fewer problems during growth process. Here, we will give an overview of the main techniques with their specifications which are used in this research.

In the work reported in this thesis, we mainly fabricated coplanar waveguide resonators (CPW) and traditional Hall bars to study the properties of (001) & (111) - oriented LAO/STO interfaces. The specifications for each research study are therefore explained in the corresponding chapters individually. The outline of this chapter is as follows: the first step is the growth of the LAO/STO interface, which is done by pulsed laser deposition. Then, we will explain the details of three main fabrication techniques: lithography, evaporation, and etching. After the fabrication is finished, we will explain the packaging for the device and the cryogenic measurement set-up which is used for Chapter 5.

2.2. MATERIAL GROWTH

Pulsed laser deposition (PLD) is one of the commonly used techniques for material growth used to obtain interfaces from various oxide films. Ever since the 1980s, it has played a crucial role in the advances in designing new materials. Since then, it has been used to deposit a variety of thin films, such as metals, semiconductors and insulators. PLD is the deposition of a physical vapour, where the growth happens layer-by-layer, resulting in high quality epitaxial films. Being able to precisely control the deposition of the material in a layer has allowed achieving very high quality materials in the laboratory environment.

The technique uses a high power ultraviolet laser facing a target placed inside of an ultra-high vacuum chamber. The laser beam results in thermal heating which results in a plasma of the target material. The plasma plume is highly directional due to the vacuum environment inside of the chamber. High-vacuum pumps control the pressure inside of the chamber. The plasma is directed towards the surface of the substrate, as shown in Fig. 2.1. The growth starts to take place when the targeted ions reach the substrate, where

real-time monitoring is possible by reflection high energy electron diffraction (RHEED) intensity oscillations. RHEED plays a key role in monitoring the oxide growth process, which allows one to accurately control the thickness of the layer.

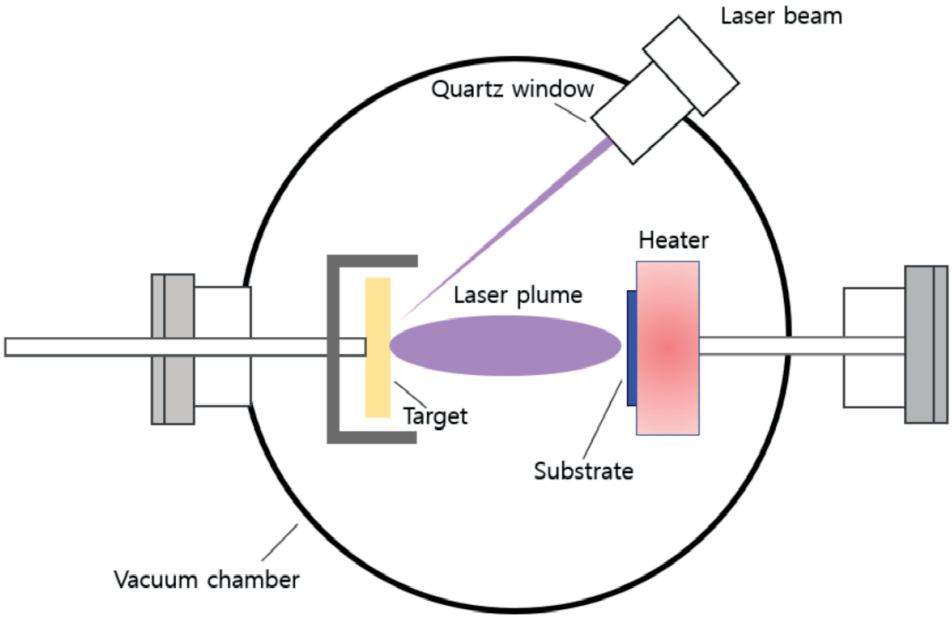

Figure 2.1: Schematic of a pulsed laser deposition system. The illustration shows the fundamental parts of the system: the laser beam, target material, plasma plume and substrate.

We used PLD tehcnique to obtain $LaAlO_3/SrTiO_3$ heterointerfaces TiO_2 rich $SrTiO_3$ substrates(TiO_2-terminated). For each research study, a different samples were grown, therefore the distinctive properties of the growth steps will be explained in detail for each corresponding chapter.

2.3. FABRICATION TECHNIQUES

Prior to any steps of the fabrication, it is very important to clean the sample thoroughly to remove all particles which remain from the growth process. Any remaining dirt or species on the surface could have an impact on the fabrication processes. Hence, the first item of work is cleaning the sample with warm acetone inside of a sonication bath for 30 minutes. Afterwards, the sample is transferred to a beaker full of isopropyl alcohol (IPA) and sonicated for $\approx$ 15–20 minutes. Lastly, the sample is dried by a N_2 gun to remove any liquid from the surface, this is essential to obtain a flat and clean surface. When the sample is inspected via an optical microscope and it is observed that no dirt or big particles remain on the sample, it is finally ready for fabrication. Current technologies in the clean room environment allow one to explore many different techniques to create unique devices. During the course of the years, different designs and techniques have been tested to yield interfaces with desired sample configuration. Even though

each sample can be different from any other, the fundamental techniques are the same for the devices which are presented in this thesis, namely, device patterning, metal deposition, lift-off and argon etching. Here, we will explain the details of these techniques for the samples which have been studied for this thesis.

2.3.1. DEVICE PATTERNING

There are different methods to pattern devices at the interface of LAO/STO complex oxides, such as electron-beam lithography, atomic force microscopy, and ion beam etching [72]. In this research, we used electron beam lithography (EBL), to expose (or generate) nano-scale devices with high resolution. It uses electrons to expose desired patterns on a surface covered with an electron sensitive resist. The lithography processes have four steps: defining the mask (pattern) via drawing software, coating the surface with a polymeric material, exposing the pattern, and the development. We designed a mask which consist of devices, bonding pads and alignment markers. Due to their transparency, markers and bonding references were used as a reference points during fabrication and placement of the chip. Hence, there are two lithography steps executed, as shown in Fig. 2.2, as first one is used for defining markers and bonding pads. The second lithography step is used for patterning the device itself. The spin coating process plays a critical role in the success of the exposure since it affects both the flatness and smoothness of the surface. If the resist is not distributed evenly over the entire surface, it could create uneven parts within a small sample. For lithography, we used a positive photoresist which releases the pattern where it is written during execution. We used Poly-Methly-Methacrylate (PMMA) positive resist, which is a combination of PMMA 495 A6 and PMMA 950 A4 resist type. The first spin-coating layer aims to have a well defined undercut for the lift-off process while the second layer is used for imaging purposes, taking into consideration that LAO is a transparent material. Prior to the spin coating process, the sample is pre-baked for 60 seconds to remove all water particles and bubbles from the surface. We observed that doing this pre-baking improves the spinning process. After the baking is completed, the sample is spin coated first with PMMA 495 A6 then with PMMA 950 A4 resist at 4000 rpm. After each step, the sample is baked at $175°C$ for 10 minutes. In the last step of the coating, it is necessary to create a conductive layer in order to not harm the ebeam lithography machine. Hence, we use a protective coating Electra 92 (AllResist AR-PC 5091) for each lithography step. The Elektra coated sample is spin-coated at 4000 rpm and baked at $110°C$ on a hot plate for 60 seconds. Then, the sample is controlled by an optical microscope and transferred to the lithography machine. Immediately after the exposure is finished, the development process starts with cleaning the electra layer with deionized water (DI) for 60 seconds. The sample is dried by the nitrogen gun prior to the development of the PMMA layer, which is necessary to avoid overdevelopment in the resist. Afterwards, the sample is transferred to a development solution of MIBK:IPA (1:3) for 90 seconds and IPA solution for 60 seconds. Lastly, it is dried by N_2 and inspected with an optical microscope. Another method for developing the PMMA layer is using a cold MIBK:IPA (1:3) solution which is stored in a refrigerator. It has been observed that the cold development method can solve the problem of resist cracks on the sample corners. We used both these methods to release exposed patterns, see **Fig. 2.3**.

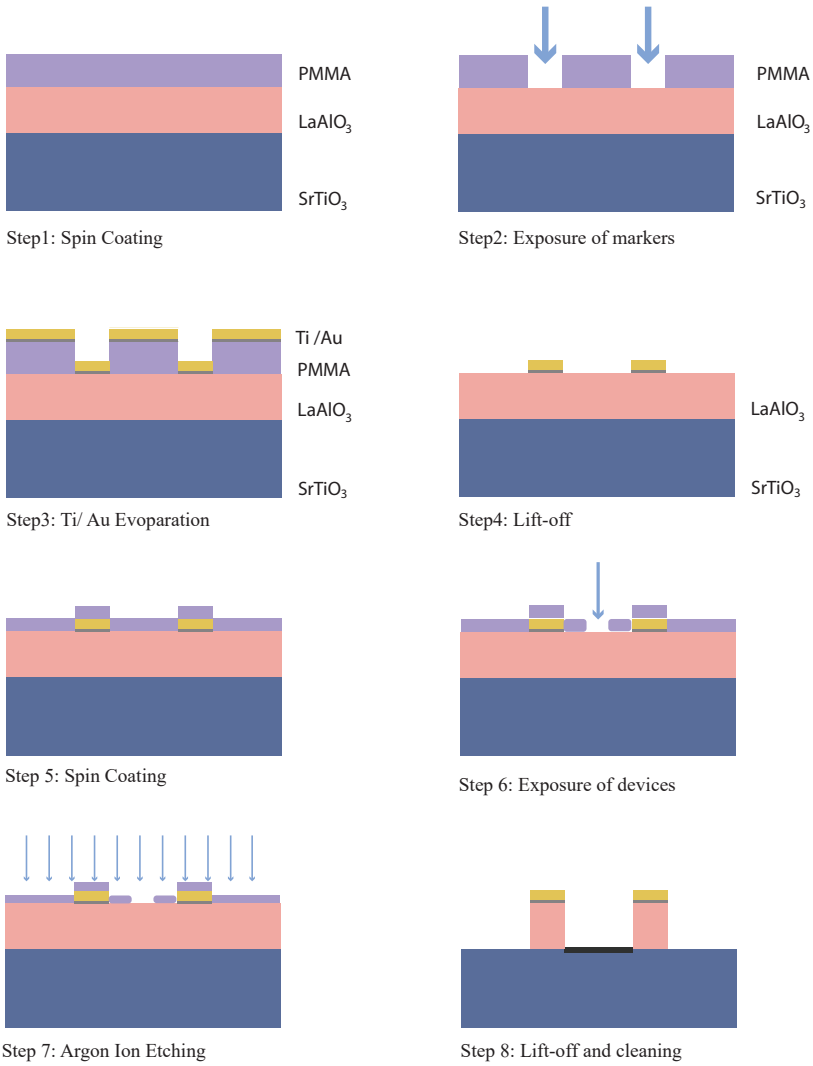

Figure 2.2: **A fabrication sequence for implementing devices at the interface; Steps 1–8** (1) Spin coating of the sample with positive resist.(2) Electron beam lithography to define markers and bonding pads. (3) Metal deposition by physical vapour depositon where both titanium and gold metals are deposited. (4) Lift-off process: Removing the metal and coating material from unwanted areas. (5–6) Same steps as 2 and 3. (7) Argon-ion etching. (8) Lift-off process and sample cleaning with IPA and acetone.

2.3.2. EVAPORATION TECHNIQUE FOR MARKER DEFINITION

Due to their transparency, it is important to create some contrast at the sample for the further experimental steps. For this reason, the alignment markers and bonding pads around the real devices need to be deposited with gold metal so it can be easily seen under a microscope. The gold has perfect visibility though it has poor adhesion to oxide substrates. Therefore, a titanium metal layer of a few nanometers is deposited before depositing the gold metal. The deposition of metals takes place in the main chamber of the AJA International Inc. machine, where the thickness of the metal can be controlled manually. The thickness of the deposition layer can vary depending on the design specifications. For instance, we deposit 3-nm titanium (Ti) and 47-nm gold (Au) metal for a sample in Chapter 5.

In order to remove the metal layer from the sample surface except in the relevant places, we used the lift-off process. Lifting-off deposited metal from the LAO layer is done with an acetone solution. This is a delicate process due to its non-repeatable behaviour. Namely, if the sample is dried with the N_2 gun before removing all undesired materials, it would not be possible to remove the remaining metal later. Unfortunately, many unsuccessful lift-off processes were experienced during this work. After many attemps, we optimized the lift-off process, which is explained as follows:

- Heat up the acetone in water bath marine for 30 minutes in advance
- place the chip on a small sample holder and put holder inside of warm acetone
- place the warm acetone in sonication bath with a small magnet inside of it
- meanwhile, prepare a seperate acetone and warm it
- place the sample holder in the new warm acetone solution and sonicate for 10 minutes
- transfer sample to IPA solution and sonicate for another 5–10 minutes
- after all metal layers come off, dry with N_2 gun

After the lift-off process is completed, the sample is prepared for the second e-beam lithography step, in which the device patterns will be exposed. We followed the same steps that are explained in the section 2.3.1. An optical image of devices after the second lithography step is presented in Fig. 2.3 a–c.

2.3.3. ARGON ION BEAM ETCHING

The last step of the fabrication process is defining the resonator and Hall bar channels by removing the $LaAlO_3$ layer from patterned channels by lithography. The last step of the fabrication is for the purpose of defining the resonators and Hall bar patterns by dry etching. We used the argon ion-beam etching technique, which is an established method for the removal of material from a sample surface. We executed an etching to fully remove the $LaAlO_3$ layer and keep the insulating $SrTiO_3$ surface around the defined devices of the $LaAlO_3/SrTiO_3$ interface. The etching step needs to stop at the point where the LAO layer is completely removed and the STO surface is still insulating. It is very

crucial to not create an oxygen-deficient conducting STO-surface or shunt the q2DEG during the etching process. Our studies show that a 111-oriented LAO / STO interface is more sensitive to the etching process than a (001)-LAO/STO interface is. Therefore, the optimization of the etching recipe played a crucial part during the fabrication of the samples. During the etching process, the chamber gets relatively warm due to ion bombardement. This temperature change could harden the PMMA layer on the sample, which could lead to unsuccessful lifting-off the materials. Our studies showed that if the etching process occurs continously for the desired time, it is very hard to remove the hardened PMMA layer during the lift-off process. Therefore, we implemented small time breaks during the etching of the LAO layer to avoid issues related to the heating of the sample. After the etching is completed, the sample needs to be transferred to warm acetone and sonicate/liff-off to remove all remaining resist from the remaining area. We removed the PMMA layer by following the list in 2.3.2 to achieve a proper cleaning of the resist layers. Once the sample is completely cleaned from PMMA layers and all the remaining residuals, we clean one last time with acetone and IPA in the sonication bath. After this stage, the sample is ready for packaging and measurements.

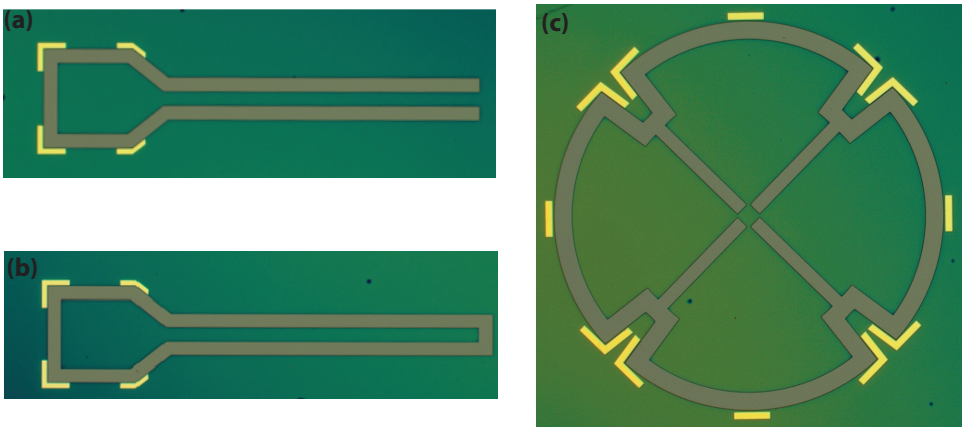

Figure 2.3: **Optical microscope image of coplanar waveguide resonators (both closed end and short end) and van der Pauw device (located at ([$\bar{1}\bar{1}$2]) crystallographic direction).** (a) The closed end resonator (b) The open end resonator with open end (c) The four-point probe device in an cloverleaf shape. These pictures were taken after the second lithography step and earlier before the etching step. Due to the transparency of the LAO layer, the final version of the devices could not be pictured clearly under the microscope.

2.4. MEASUREMENT SET-UP FOR MICROWAVE MEASUREMENTS

For each research chapter, we work with a dedicated measurement set-up, which turn out to be different from each other. Here, we will explain the device packaging and measurement set-up which is customized for the research study of Chapter 5. The details for Chapters 3 & 4 will be explained in the corresponding chapters. After the fabrication is completed in the clean room, the sample is prepared for microwave and transport measurements. Cryogenic dilution fridges have different systems to place the sample in a milli-Kelvin stage. In this set of experiments, all measurements were executed in the Oxford Triton Dilution Refrigerator, where the sample holder is attached to a vacuum lock which cools down the sample holder to 14 mK within 12 hours time slot. We will explain the details of the dilution system in the next section. Here, we will provide the details for the sample's placement inside of the sample holder. In the first place, the sample is integrated to a printed circuit board (PCB) which faciliates the connection between the measuring equipment and the dilution unit. Due to the design of the experiment, we created a PCB having both DC and RF connectors, as shown in Fig. 2.4 (a). This allows performing the measurements one after another without changing the sample's temperature drastically. Another advantage is being able to have access to both devices so as to monitor the behaviour of the sample more accurately, e.g. its electron doping. For electrical contact to devices, two or three wire was connected to each device. Moreover, plenty of Al-wire was placed to ground plane of the sample to ensure good electrical isolation between devices. There are 24 DC and 2RF SMP connectors located on the board, which are connected to the devices using Al wirebonds. In order to place the PCB and bias tee inside of the sample holder, we designed a home-made PCB holder which is attached to the bottom of the sample holder. In Fig. 2.4(c), we present the final configuration of the packaging, which includes the PCB, bias-tee and RF cables. In order to apply an electric field to the devices with our PCB design, bias-tee equipment is implemented behind the PCB holder. The DC source of the bias-tee allows us to send electrical signal during gating application. As the final step, the PCB holder is tightly placed inside of the sample holder and closed with shields. Afterwards, the sample is placed on the vacuum lock which is used for transferring the sample inside of dilution unit. The vacuum load–unload stick facilitates the sample's loading to sub-kelvin stage of the dilution unit. After the sample is loaded to the mixing chamber plate the system is set to cool down to base temperature, which is ≈ 15 mK. Due to the design of the dilution unit, one can cool down the sample without opening the system entirely. This provided many advantages during the course of the work, by allowing fast sample exchange time. After the sample is cooled down to base temperature, the input power parameter is optimized for RF-measurements. We used a vector network analyzer to send and collect the signal from the device. In Figure 2.5, we present the measurement set-up and a picture of the dilution unit most used in this work.

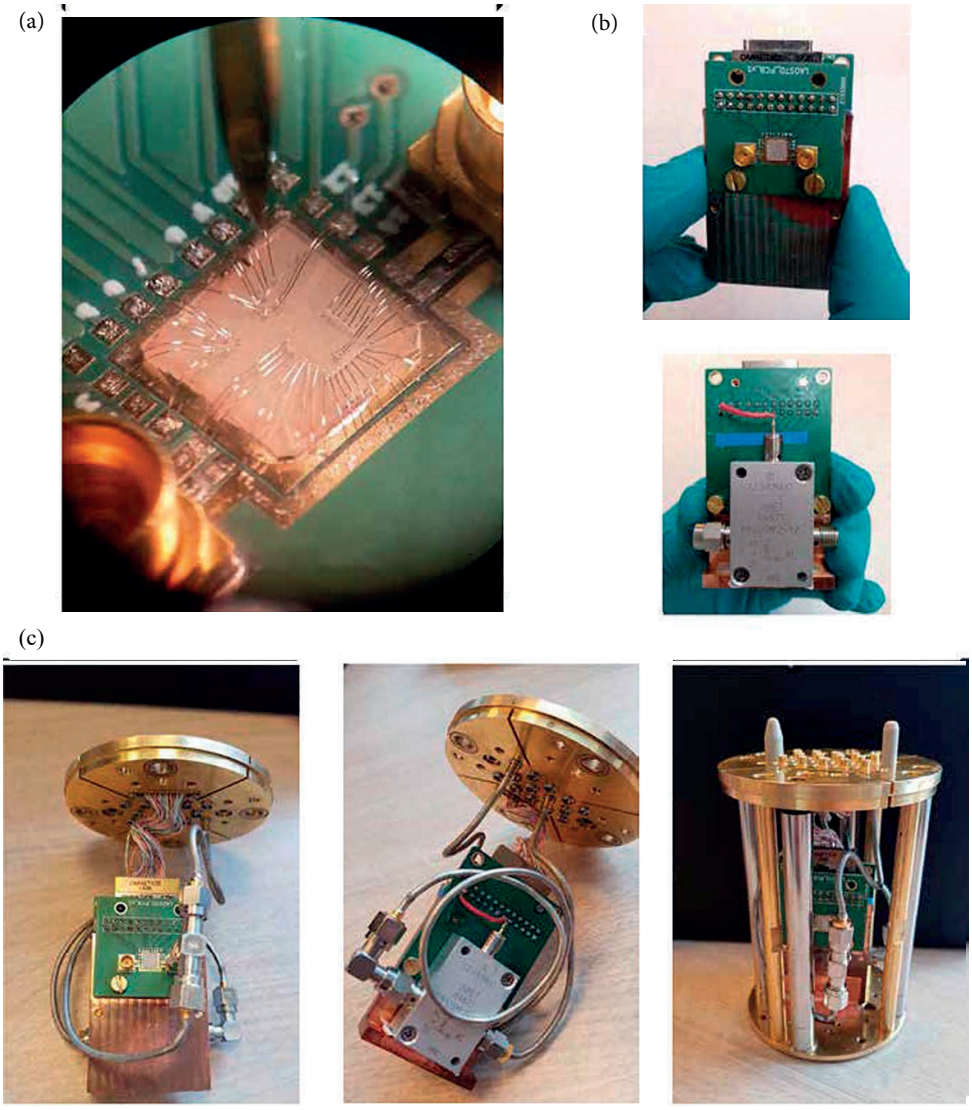

Figure 2.4: **Sample packaging to dilution system puck.** (a)The 5x5 mm LAO/STO sample is placed at the centre of a printed circuit board. The devices are connected to PCB connectors via Al wirebonds (b) Bias-tee is placed on the back of the home-made holder with glue (c) Electrical connection between devices and measurement set-up is provided by semi-flexible RF cables and already built-in DC connectors at the sample puck.

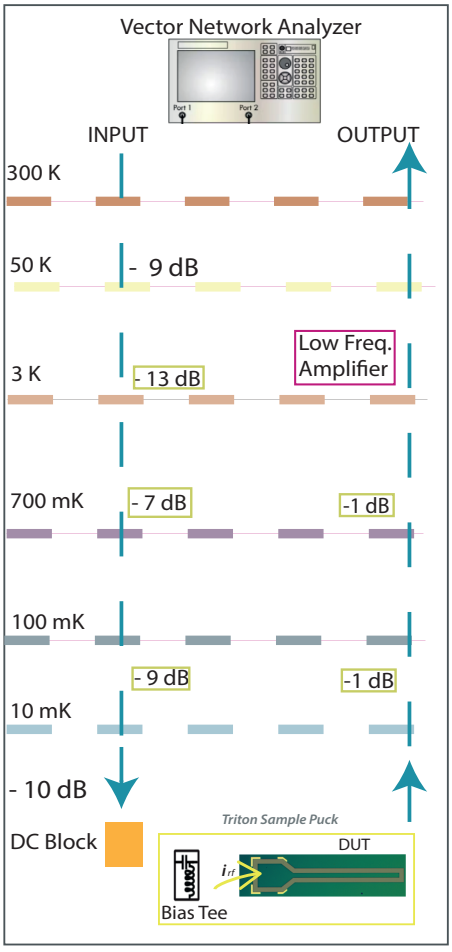

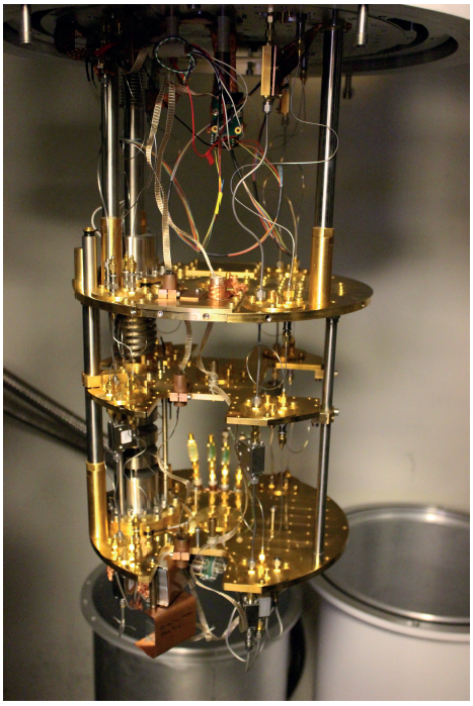

Figure 2.5: **The measurement set-up including a schematic layout of dilution fridge unit and wiring scheme.** The vector network analyzer is used for the microwave measurements. The input signal is sent through the input line and attenuated until it reaches the mounted sample. The output signal is amplified by a low frequency amplifier which is located at the 3K stage.

3

BIMODAL PHASE DIAGRAM OF THE SUPERFLUID DENSITY IN LAO/STO REVEALED BY AN INTERFACIAL WAVEGUIDE RESONATOR

Superconducting coplanar waveguide resonators are powerful tools with high-quality factors and low intrinsic losses. These characteristics make them ideal to probe the superconducting behavior of oxide interfaces as providing a direct measurement of superfluid density. Our study shows that these devices provide a new route to explore exotic behaviors of complex oxides. We will explore the superconducting phase diagram of the 2DES as a function of temperature and electric field effect. Direct measurement of the resonator cavity modes are translated into superfluid density (n_s), critical temperature (T_c) and Pearl length. T_c and n_s follow a dome shape with non-monotonic behaviour. Additionally,the ground state of this two-dimensional electron system is interpreted as a Josephson junction array, where a transition from long- to short-range order occurs as a function of the electronic doping. [1]

[1] Parts of this chapter have been published in Physical Review Letters **122**, 3 (2019) [73].

3.1. INTRODUCTION

The interface between the two wide band-gap insulators $LaAlO_3$ (LAO) and $SrTiO_3$ (STO) hosts a two-dimensional electron system (2DES) [9, 74] that shows superconductivity [49] together with strong spin-orbit coupling [54, 75]. Its low carrier concentration makes this 2DES particularly sensitive to elecrostatic gating, and a superconductor-insulator transition, tunable Rashba splitting, and tunable superconductivity have already been demonstrated [11, 76, 12]. Despite being considered the prototypical correlated 2DES and a platform to realize tunable superconducting devices [33, 77, 18], the nature of its superconducting ground state and dome-shaped phase diagram, observed upon electrostatic doping, is still not understood. This partly stems from the fact that standard magnetotransport measurements do not allow us to directly probe the superfluid density, and so far few approaches have been proposed to overcome such limitation. Bert *et al.* employed a scanning-SQUID technique to measure the penetration depth of the screening supercurrents and extract the superfluid density of the 2DES [30], while, more recently, Singh *et al.* calculated the variations of the superfluid density from the resonance frequency of a RLC circuit containing a lumped LAO/STO element by means of an equivalent-circuit model [78]. The superconducting coplanar waveguide resonators (SCWRs) are powerful tool to probe the superfluid density parameter. SCWRs are cavities for the electromagnetic field where the frequencies of the standing waves are determined by the interplay between the geometry and electromagnetic environment [79, 80]. The formation of quasiparticles in a SCWR causes a downshift of their resonance frequencies because the lower superfluid density increases the kinetic inductance [81].The detection of low number of particles is possible due to kinetic inductance detectability.

3.2. DEVICE FABRICATION AND MEASUREMENT SET-UP DETAILS

The pristine heterostructure is obtained by the pulsed laser deposition of 12 unit cells of crystalline LAO on top of a TiO_2-terminated $SrTiO_3$ substrate. The LAO film is deposited at 840 °C in 6×10^{-5} mbar of pure oxygen on top of a syngle-crystal (001)-$SrTiO_3$ substrate. The laser pulses were supplied by a KrF excimer source ($\lambda = 248$ nm) with an energy density of 1 J cm^{-2} and a frequency of 1 Hz. In order to remove oxygen vacancies, the growth process was followed by an annealing in 300 mbar of oxygen, at 600 °C for 1 hour. The sample was subsequently cooled down to room temperature at a rate of 10 °C min^{-1} in the same oxygen atmosphere. The growth process was monitored in-situ using reflection high-energy electron diffraction (RHEED), which indicated a layer-by-layer growth mode.

The SCWR is fabricated by covering the sample with a protective layer of polymethylmethacrylate (PMMA) which is patterned by Electron Beam Lithography (EBL). After the developing process, the exposed areas are etched by Ar-milling (500 eV, 0.2 mA cm^{-2}) to remove the LAO layer and obtain electrical isolation between the central line of the resonator and the ground plane (GND). Background information regarding to each fabrication step can be found in Chapter 2. After fabrication steps are completed,the sample is glued to an isolated holder with conductive silver paint, which enables to apply electric field to the sample via back-gate geometry.The ground plane and the feed-line share the same electrical ground, so the back-gate voltage (V_{BG}) affects both.

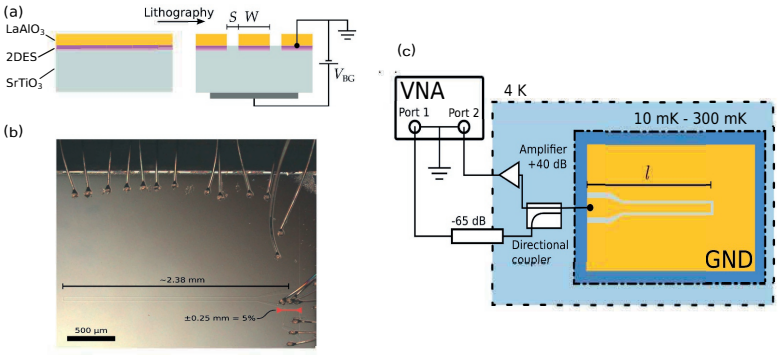

Figure 3.1: (a) Schematics of microwave resonator fabricated at the interface of LAO/STO structure. (b) Optical microscope image of the coplanar waveguid resonator. Aluminium bonds provide an electrical connection to device on the sample. (c) Schematics of the experimental set-up. The input line signal is attenuated -65 dB until it reaches to mK stage. The output signal is amplified by +40 dB from mK stage to room temperature signal line.

3.3. RESULTS

Here, we realize a SCWR by direct patterning of the 2DES at the LAO/STO interface. This approach gives a stronger modulation of the resonance frequency in comparison to lumped-element designs used in previous implementations. The resonance frequencies of the superconducting coplanar waveguide resonators are monitored as a function of the temperature and electrostatic doping where later translated into the Pearl length, transition temperature, superfluid density parameters.

3.3.1. REFLECTION SPECTRUM MEASUREMENTS

As it is shown in Fig. 3.1 (b), the central line has a width (W) of 40 μ m, a nominal length (l) of 2.5 mm and a spacing S of 10 μ m from the GND. One end of the device is isolated from the ground plane while the other one is connected to input line by aluminum wires. The large impedance mismatch between two ends of the resonator line realizes a nearly half-wavelength ($\lambda/2$) resonator. It is crucial to evaluate the actual length of the device for data analysis. We calculated the length by considering the error on the length is almost equal to the size of the contact area,giving l=2.38±0.12 mm which is presented in Fig.3.1(b). The cavity modes of the $\lambda/2$ resonator are measured with a vector network analyzer (VNA) as displayed in Fig.3.1 (c). The power of the signal injected into the SCWR is about −95 dBm. The output signal is attenuated in total +40 dBm. Figure 3.2 (a) represents the response spectrum of the SCWR at T= 11 mK under no electric field effect (V_{BG} = 0 V) case. As it can been seen from spectrum, ten modes can be identified on top of an oscillating background, which stems from interference in the connecting circuitry.

We based our analysis on the modes 2-5 as it is shown in Fig.3.2 (b). The first mode is excluded from our analysis since it is resonance frequency is very close to cutoff frequency of the room temperature amplifier (30 MHz). In addition to that, modes higher than five are also not taken into account due to their lower visibility. Here, the broad-

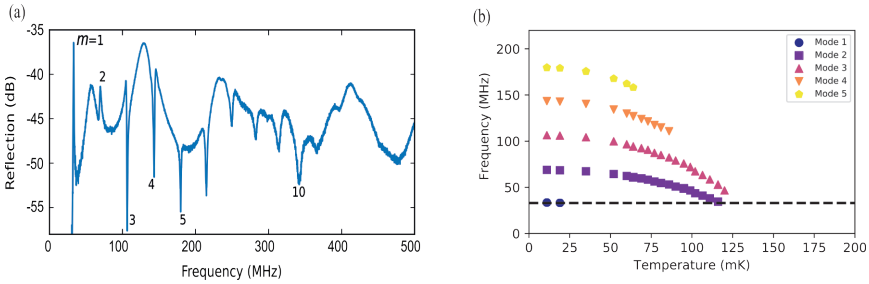

Figure 3.2: Reflection spectrum of the superconducting coplanar waveguide resonator at base temperature. (a) The reflection response of the resonator with $-95\ dBm$ input power and no gate voltage applied, $V_{BG} = 0$,V. (b) Measured response of the resonator as a function of temperature for first five mode. The numbers are obtained from the first five mode of the resonator which is translated from the response spectrum in the left.

ening and weakening of the peaks at higher frequencies are in agreement with previous results of the $SrTiO_3$ substrate [82]. The eigenfrequency (f_m) can be modeled as a parallel RLC circuit as explained in Chapter 1,

$$f_m = 1/(2\pi\sqrt{L_m C})$$

where the inductance and capacitance value changes for each mode of the resonator. [83]. In general, the inductance of a superconducting resonator is a combination of geometric and a kinetic contribution. [70] In our device, the first mode has a total geometric inductance of about 0.16 nH, while the kinetic inductance is about 4 nH at at T= 11 mK case. In this manner, L_m is dominated by the kinetic contribution, similar to what has been observed in other LAO/STO superconducting devices [84, 77]. This allows us to write the following expressions for the Pearl length Λ and the 2D superfluid density n_s in terms of f_m:

$$\Lambda = \alpha \left(m/f_m\right)^2, \tag{3.1}$$

$$n = \beta \left(f_m/m\right)^2, \tag{3.2}$$

where α and β are determined by the following parameters; the line geometry, the dielectric environment and the effective mass of the charge carriers, which are defined as following equations;

$$\alpha = \frac{W}{8dl^2}\frac{K(k_0')}{K(k_0)}\frac{1}{\mu_0\varepsilon_0\varepsilon_{\text{eff}}} \tag{3.3}$$

$$\beta = \frac{16l^2}{W}\frac{K(k_0)}{K(k_0')}\frac{\varepsilon_0\varepsilon_{\text{eff}}}{q^2}m_e \tag{3.4}$$

These formulations prove that with an observation of the magnitude of the resonance frequency of the resonator as a function of T and V_{BG}, it is possible to investigate the superconducting state behavior of 2DES. In addition to that, this technique is a high-sensitivity probe technique due to the nature of the low density of cooper pairs of superconducting gas which leads to having high kinetic inductance. Although it is a sensitive technique, we shall mention the calculated values of the n_s suffer from two main sources of error. First, the two ends of the line are not perfect mirrors and the values of f_m are thus influenced by both the geometry of the launcher and the capacitance of the bonding pad. Second, the size of the bonding wires connecting the line leads to an estimation of its effective length of 2.38±0.12 mm. We thus consider a confidence interval of ±10% for the calculated absolute values of n_s and Λ parameter.

3.3.2. TEMPERATURE DEPENDENCE OF 2DES

In this section, we will explain the temperature dependence of the cavity modes of the microwave resonator from $m = 2$ to $m = 5$ at $V_{BG} = 0$ V. As it is shown in Fig.3.3(a), all modes are evenly spaced and their translation into characteristic parameters are in good agreement. They follow a single pattern as a function of temperature. As we approach the superconducting to insulating transition, the cavity modes started to disappear which comes from the increased power dissipation associated with the formation of quasi-particles. In the normal state, this device shows no resonance peaks, owing to the metallic character of the interface. It is possible to calculate the temperature depen-

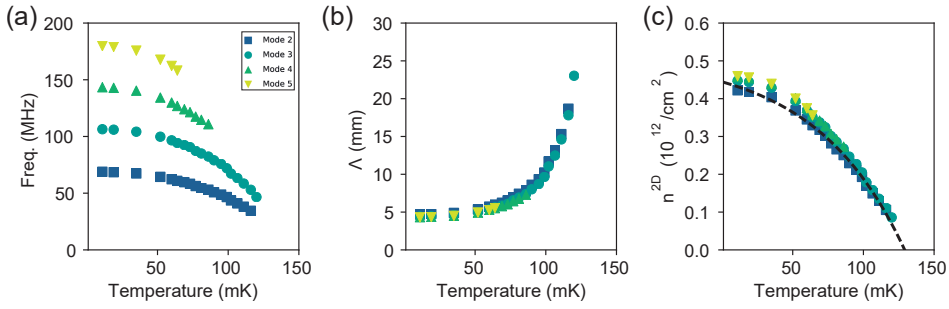

Figure 3.3: Temperature dependence of the superconducting order parameters from resonance frequencies. (a) Frequencies of the cavity modes from $m = 2$ (blue squares) to $m = 5$ (yellow reversed triangles) at $V_{BG} = 0$ V. (b) Pearl length and (c) superfluid density calculated from the data in (a) using Eqs. (3.1) and (3.2). The solid line in (c) is the best fit of Eq. (3.5) for $m = 3$, which gives $T_c = 133 \pm 2$ mK.

dence of Λ and n_s from the frequency of each cavity mode as it is presented in Eqs. (3.1) and (3.2). We display the calculated values for the first four modes in Figs.3.3(b) and 3.3(c), respectively. The pearl length value at base temperature is about $\Lambda(11\text{ mK}) = 4.8 \pm 0.5$ mm which is in good agreement to what was estimated in Ref. [77], and as temperature increase its value goes above 23 mm. On the other hand, superfluid density shows an opposite trend as temperature increases above 120 mK. At base temperature, n_s is about 8.7×10^{13} cm^{-2} and shows a negative slope which becomes more pronounced as we approach to higher temperature values.

In order to understand the behavior of 2DES, we fit the temperature dependence of

n_s with a phenomenological BCS model by following an equation:

$$n = n_0 \left[1 - \left(\frac{T}{T_c} \right)^{\gamma} \right], \tag{3.5}$$

where n_0 is the zero-temperature superfluid density, T_c is the superconducting critical temperature and γ is an exponent which describes the opening of the gap below T_c [85, 30]. The black solid line in Fig.3.3 (c) is the best fit of Eq. (3.5) calculated for the third mode (circles in Fig.3.3). If we consider both the second and third modes, which show the best visibility in temperature, we obtain $\gamma = 1.95 \pm 0.23$ and $\gamma = 1.96 \pm 0.20$, respectively. These results are in fairly good agreement with a clean s-wave BCS scenario, where a value of $\gamma = 2$ is predicted [85]. This is in contrast with previous works reporting $\gamma = 2.8$ [30] and a possible indication of lower disorder in our sample [86].
The critical temperature from microwave resonator data is calculated as $T_c = 133$ mK. We can compare the value with the transport measurements results which are performed by making 4 different wires at the ground plane of the sample as it is explained in the Supplementary Information, 3.5.1. The electrical resistance is current-dependent below 132 mK and shows a sharp transition around 119 mK. Although quantitative analysis is not possible because of not having a dedicated transport device and having inhomogeneous current flow, we can consider the T_c as the temperature at which the electrical resistance at zero bias reaches half of its normal state, obtaining ≈120 mK, in good agreement with the temperature dependence of the SCWR cavity modes. This agreement shows that it is possible to calculate the main characteristics of superconducting system with coplanar waveguide resonators.

3.3.3. ELECTRICAL DEPENDENCE OF 2DES

The experimental configuration enables tuning the superfluid density of 2DES by electric field effect. Here, we will display the response of resonators under field effect for various temperatures. In Figure 3.4(a) and (b) we show two color maps of the spectral response of the SCWR measured at 11 mK and 133 mK as a function of V_{BG}. The spectral response of the resonator over different temperatures for the same voltage regime is displayed in Supplementary Information 3.5.3. At the base temperature, when the gate voltage goes below −20 V the cavity modes rapidly shift to low frequencies and then disappear, while at the positive voltage regime, the response is rather flat with a slightly decreasing trend. In the high temperature (T= 133mK), modes of the resonator became less visible and display a more dome-like response.

In Figure 3.4 (c) it is displayed that the superfluid density shows a pronounced dome-like response for all the modes for various temperatures and even quenched on both ends at 133 mK. This response originates from the modulation of n_s, and a possible contribution to the observed signal from the electric-field dependence of the STO dielectric constant is discussed and ruled out in the Supplementary Information 3.5.2 [87, 88, 82]. Similarly to the analysis reported in Fig.3.3, we calculate the voltage dependence of n_s at different temperatures using Eq. (3.2). Here, we base our analysis on the third mode ($m = 3$), which shows the best visibility over the whole space of parameters, while a complete dataset of the first five modes is reported in the Supplementary Information 3.5.3. The phase diagram of the superfluid density reported in Fig.3.4(c) is characterized by a

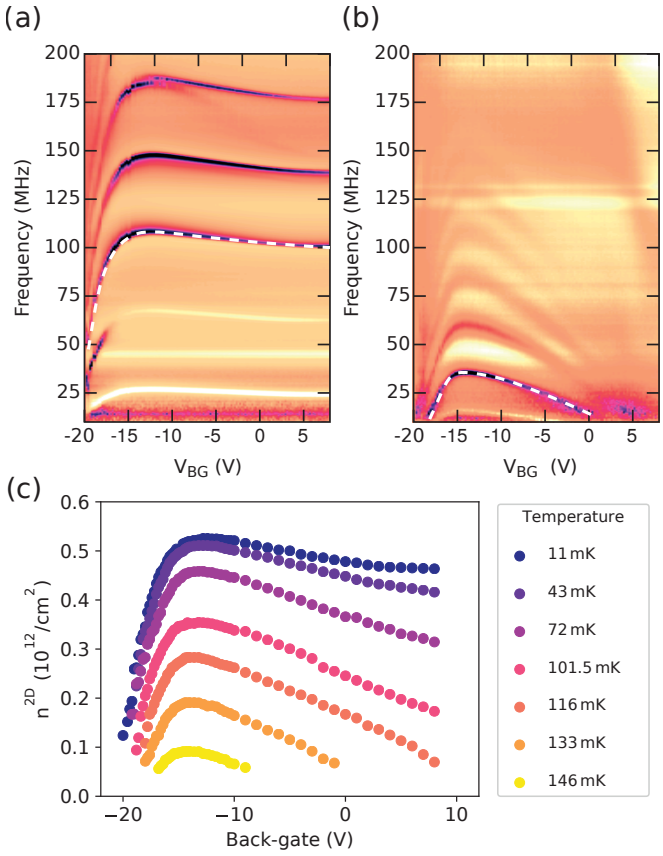

Figure 3.4: Back-gate voltage dependence of coplanar waveguide resonators. (a,b) Reflection amplitude of the SCWR as a function of V_{BG} at 11 mK,(a), and 133 mK(b). The white dashed line is a guide to the eye highlighting $m = 3$. (c) The calculated superfluid density as a function of V_{BG} for various temperatures.

dome-like shape that becomes progressively lower and narrower with increasing temperatures. It peaks at about -12.5 V, where superconductivity is still detected at 146 mK, well above $T_c = 132$ mK calculated from Fig.3.3(c) and indicating that the pristine 2DES is in the over-doped regime. The maximum value of the Cooper pairs density is $n_s \approx 1\times10^{12}\text{cm}^{-2}$, corresponding to an electron density of 2×10^{12} cm^{-2}. This is in agreement with previous experiments [30, 53, 52, 78], supporting the conclusion that only a small fraction of charge carriers participate in the superconductivity.

In Figure 3.5(a) we compare the effect of V_{BG} on n_s at the base temperature and T_c, where the latter was calculated by fitting the data reported in Fig.3.4 with Eq. (3.5). Both of them display a well-defined dome-shape dependence, with a maximum at $V_{BG} \approx -12.5$ V. The different position of their maximal value comes from a progressive shift of the maximum of $n(V_{BG})$ with temperature and is discussed in the Supplementary Material, Sec. 6. Different explanations have been proposed to this peculiar phase diagram.

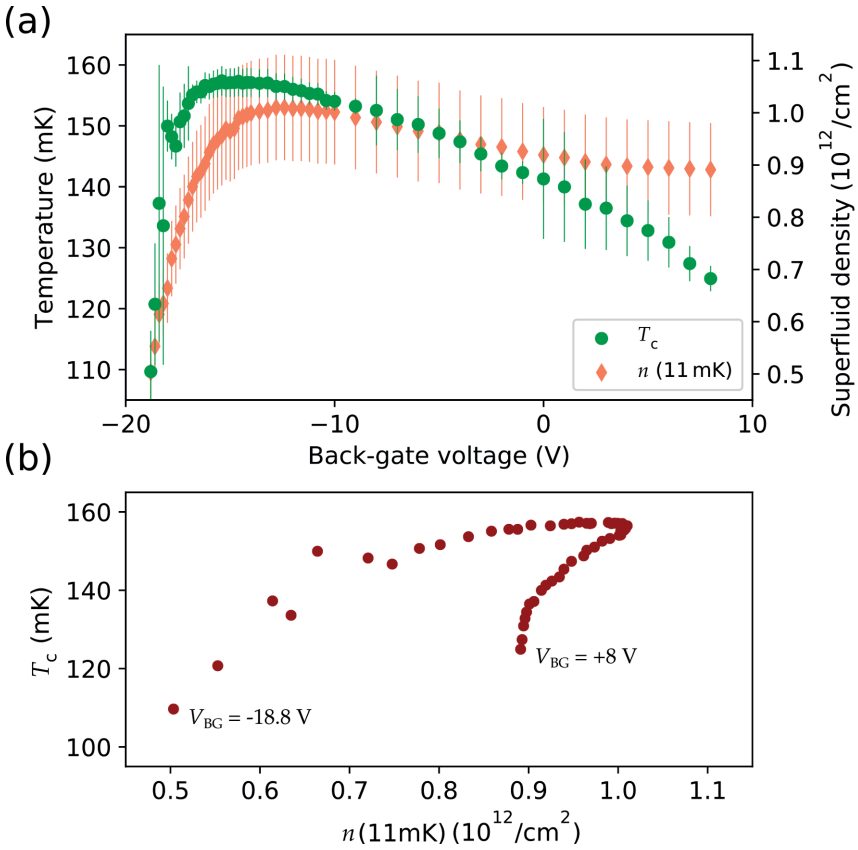

Figure 3.5: Analysis of the superfluid gate dependence. (a) T_c and n(11 mK) as a function of V_{BG}. T_c is calculated by fitting the data from Fig.3.4(c) with Eq. (3.5). (b) Critical temperature as a function of the superfluid density at 11 mK

The peak of the T_c has been ascribed to the Lifshitz transition, where the over-doped regime is a consequence of the onset of a population of d_{xz}, d_{yz} bands [53], to low-density carriers located in a high-mobility band showing non-monotonic population under field-effect due to the interplay of orbital effects and correlations [52], or a combination between the multi-band nature of this 2DES, electronic correlations, and disorder [78, 27]. The interplay between n(11 mK) and T_c can be further investigated considering the T_c–n(11 mK) plot in Fig.3.5(b). An upper and lower branch appear, corresponding to the over- and under-doped condition and connected at $V_{BG} \approx -12$ V (optimal doping). A similar bimodal distribution was also reported by Bert *et al.* (grey dataset of Fig. 3 in Ref. [30]) and ascribed to inhomogeneities that locally suppress n_s in the over-doped regime. In our case this interpretation is at variance with the results from Fig.3.3(c), where the critical exponent $\gamma \approx 2$ indicates low disorder.

3.3.4. BIMODAL PHASE DIAGRAM

The data presented in this work allows one to view the superconducting phase as the ground state of a Josephson junction array. For zero gate voltage, DC-transport measurements show that increasing the current at the device produces dissipation above a temperature dependent threshold (see Supp. Inf. 3.5.1). Upon further increase of I, one observes a steep rise in the resistance R beyond a second threshold, and R ultimately levels off to its normal state value. In the Josephson junction language a BKT-like transition takes place at the lower threshold value $I_{c1} = E_J/(\varepsilon_v \Phi_0)$, where I_{c1} represents the typical maximum supercurrent of a junction, E_J is the Josephson coupling and $\Phi_0 = h/(2e)$ is the flux quantum [89]. The dielectric constant, ε_v, jumps from a finite value to infinity at the transition (strictly speaking this only holds at $T = 0\,\mathrm{K}$) and dissipation sets in above I_{c1}. For still larger values of the current, individual junctions in the array can sustain phase coherence (short-range order) as long as $I<I_{c2} = E_J/\Phi_0$. For $I > I_{c2}$, the array eventually crosses over to the normal state. In the intermediate regime, $I_{c1} < I < I_{c2}$ one may then define a bare (unrenormalized) density of Cooper pairs n_0 such that [89],

$$n_0 = \frac{2m_e}{2\pi\hbar^2} I_{c2}\Phi_0 \tag{3.6}$$

From Fig. 3.3(d) we determine $\frac{I_{c2}(92\ \mathrm{mK})}{I_{c2}(109\ \mathrm{mK})} = 1.8$. This number is in line with the ratio that one can extract from the temperature dependence of the cavity modes in Fig. 3.3(c), which is $\frac{n_0(92\ \mathrm{mK})}{n_0(109\ \mathrm{mK})} = 1.79$. From Fig. 3.3(d) we see that for increasing temperatures I_{c1} and I_{c2} are no more distinguishable and T_c goes to zero together with n_s. The temperature dependence of n_s reported in Fig. 3.3(c) (overdoped condition) can be thus interpreted as a regime where the superconducting islands are large enough to sustain long-range coherence and $n(T)$ follows the simple BCS model of Eq. (3.5), that in this case was found compatible with a clean s-wave superconductor. In the under-doped condition the lowered electron density makes the superconducting puddles lose connection, resulting in a transition dominated by short-range order. This picture explains the two branches of Fig. 3.5(b), originating from the different nature of the ground state in the two regimes, in agreement with recent experimental results [90, 91]. We may now justify the fact that the transport properties of the 2DEG in this device can be related to their counterpart in Josephson junction networks.

3.4. CONCLUSION

In conclusion, we studied the superfluid density at the (001)-oriented LAO/STO interface by means of a coplanar waveguide resonator patterned into the heterostructure itself. With no gate applied, the temperature dependence of the superfluid density is in good agreement with a clean s-wave BCS superconductor, while under field effect both the critical temperature and the superfluid density show a dome-shaped phase diagram, leading to a multi-valued relationship between them. We find that both the critical temperature and superfluid density display a domelike shape as a function of the back-gate voltage, which are not monotonically related. This non-monotonic behavior arises from the ground state of the system, which is identified as a Josephson junction array shifting from short- to long-range order while driving the system from the underdoped to overdoped condition. These studies show that the new way of accessing the superconducting

state will help us map the phase diagram of complex oxides.

3.5. SUPPLEMENTARY INFORMATION

3.5.1. DC V–I MEASUREMENTS

In Figure 3.6 we show a series of voltage vs current curves measured at different temperatures at zero back-gate voltage. The data reported in Figure 2(d) in the main text were calculated as the ratio between measured voltage and applied current. These data were acquired by wire-bonding the ground plane of the LAO-STO sample with four aligned contacts, as schematically shown in the panel (b) of the figure.

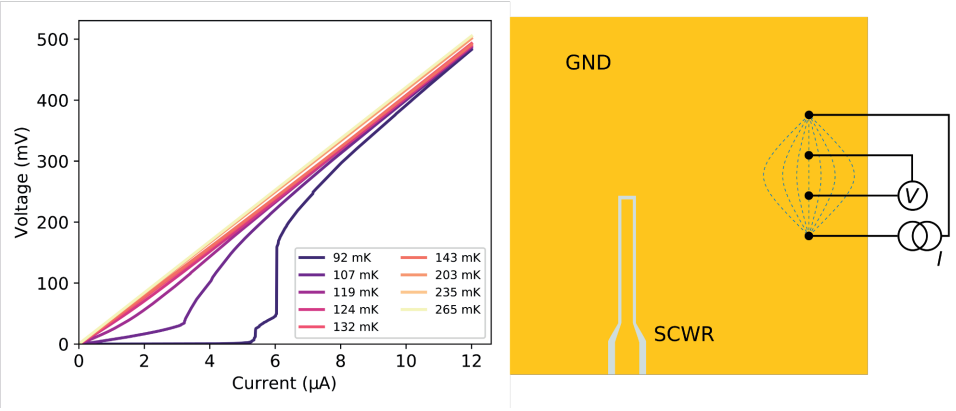

Figure 3.6: (a) Voltage-current relationship as a function of temperature measured by wire bonding the ground plane. (b) Schematic drawing of the measurement configuration. The blue dashed lines indicates the current flow in the ground plane (GND) surrounding the superconducting coplanar waveguide resonator (SCWR)

3.5.2. CONTRIBUTION OF THE FIELD-DEPENDENT DIELECTRIC CONSTANT OF $SrTiO_3$

A different explanation for the observed shift of the cavity modes as a function of the backgate voltage reported in Fig. 3.4 (a) and (b) in the main text may involve the electric-field dependence of the dielectric constant of the $SrTiO_3$ substrate. This would lead to a variation in the resonance frequencies of the resonator due to a different capacitance instead of kinetic inductance. It was recently reported high tunability (> 200%) in CPWs fabricated on top of $SrTiO_3$ substrate upon the application of small voltages (below 15V) [82]. This result was based on the tuning of the dielectric constant of the STO between the line and the ground plane by field-effect. However, in our case he maximum back-gate voltage (−20 V) corresponds to an electric field of about 0.4 kV /cm, which is too small to be the origin of the observed frequency shift [87]. To confirm this we fabricated a superconducting Molybdenum-Rhenium coplanar waveguide on top of a $SrTiO_3$ (001) substrate and applied a field effect in the back-gate geometry. In this case the superfluid density is much higher than the 2DES in LAO/STO, and response from V_{BG} would mean

that the substrate contribution is not negligible. As shown in Fig.3.7, upon the application of a back-gate voltage of 20 V a barely visible frequency shift of the cavity modes was detected, meaning that the contribution from the field-dependent dielectric constant of the substrate can be neglected.

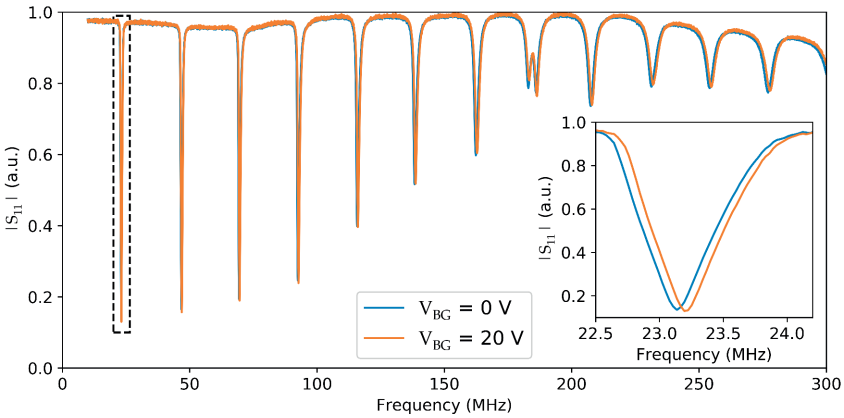

Figure 3.7: Spectrum showing the cavity modes of a superconducting Molybdenum-Rhenium coplanar waveguide patterned on top of a substrate of (001)-$SrTiO_3$ for V_{BG} =0 V and 20 V. The inset shows a magnification of the region inside the dashed line (first mode).

3.5.3. VOLTAGE AND TEMPERATURE DEPENDENCE OF THE FIRST FIVE CAVITY MODES

Figure 3.8 shows the value of the resonance frequencies of the cavity modes from m=1 to m=5 extracted from the raw data, as the ones presented in Fig.3.4(a) and (b) in the main text. The first mode lies below the cut-off frequency of the amplifier (see Figure 2(a) in the main text) and is thus affected by a systematic error. All the modes show a similar dependence from back-gate voltage and temperature, however the third mode has the best visibility in the whole space of parameters and was employed to perform the analysis reported at the main text.

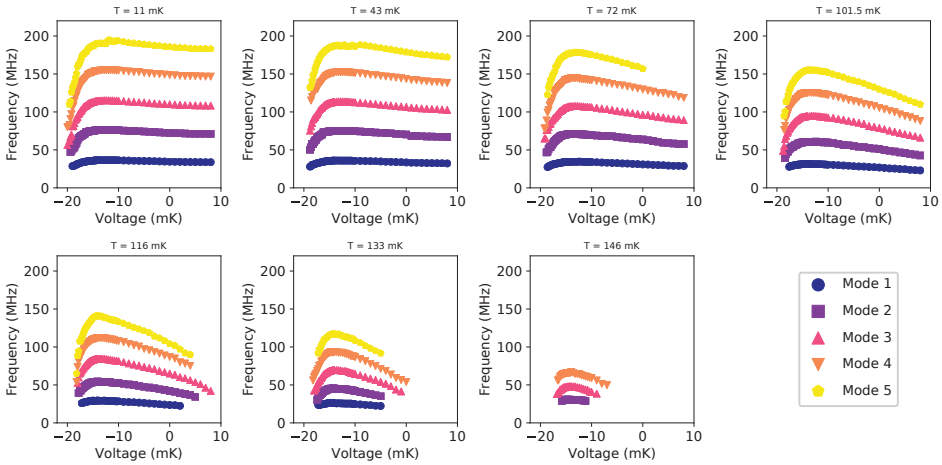

Figure 3.8: Resonance frequencies of the five lowest cavity modes as a function of V_{BG} for different temperature values

3.5.4. TEMPERATURE DEPENDENCE OF THE OPTIMAL DOPING CONDITION

In Figure 3.9 we show the interplay between temperature and back-gate voltage in determining the optimal doping condition, which is evaluated from the data reported in Fig. 3(c) of the main text. The optimal doping is defined as the maximum value of n_s as a function of V_{BG} for a given temperature. The value of the back-gate voltage corresponding to the optimal doping condition shifts downward with increasing temperature, similarly to what the maximal superfluid density does. Such a temperature dependence is typical when considering n_s, but it is not expected when considering V_{BG}, at least within this range of temperatures where the dielectric properties of the $SrTiO_3$ substrate are constant. The purple star marker indicates the maximal critical temperature extracted from Fig.3.5(a) in the main text. This shows a good agreement between the voltage sweeps at fixed temperature and the critical temperatures extracted from the fits of the data.

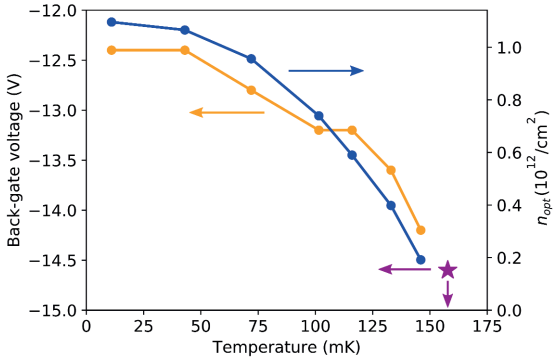

Figure 3.9: Comparison between the temperature dependence of the value of V_{BG} maximizing n_s (orange line) and the corresponding n_s (blue line) extracted from the data of Fig. 3. The purple star indicates the highest T_c, extracted from Fig. 4(a), and the corresponding V_{BG}

4

A Study of the Planar Hall Effect for (111)-$LaAlO_3$ and $SrTiO_3$

Quantum materials can display physical phenomena rooted in the geometry of electronic wavefunctions. The corresponding geometric tensor is characterized by an emergent field known as Berry curvature (BC). Large BCs typically arise when electronic states with different spin, orbital or sublattice quantum numbers hybridize at finite crystal momentum. In all materials known to date, the BC is triggered by the hybridization of a single type of quantum number. Here, we report the discovery of the first material system having both spin and orbital-sourced BC: $LaAlO_3/SrTiO_3$ interfaces grown along the [111] direction. We detect independently these two sources and directly probe the BC associated to the spin quantum number through measurements of an anomalous planar Hall effect. The observation of a nonlinear Hall effect with time-reversal symmetry signals large orbital-mediated BC dipoles. The coexistence of different forms of BC enables the combination of spintronic and optoelectronic functionalities in a single material.[1] *[92]*

[1] Parts of this chapter have been published in Nature Materials **5**, 576 (2023)

4.1. INTRODUCTION

When moving along closed paths, electrons can accumulate a geometric Berry phase related to the flux of a field, called Berry curvature, encoding the geometric properties of the electronic wavefunctions. In magnetic materials adiabatic motion of the electrons around the Fermi surface provides such a Berry phase. It is directly observable since it governs the intrinsic part of the anomalous Hall conductivity [93, 94]. Anomalous Hall effect measurements therefore represent a charge transport footprint of the intrinsic geometric structure of the electronic wavefunctions. In non-magnetic materials the BC field is forced to vanish by symmetry when summed over the occupied electronic states. However, local concentrations of positive and negative BC in momentum space are allowed by acentric crystalline arrangements [95]. This segregation of BC in different regions of momentum space appears whenever electronic states with different internal quantum numbers are coupled to each other by terms that depend linearly on the crystalline momentum k. In these regions the electronic bands typically resemble the dispersion relations of relativistic Dirac or Weyl fermions. The spin-orbit linear in k coupling between different spin states shapes the Dirac cones at the surfaces of three-dimensional topological insulators [96, 97] and the Weyl cones of topological semimetals [98]. Couplings between different atomic orbital and sublattice states give rise instead to the (gapped) Dirac cones of transitional metal dichalcogenides and graphene. Conceptually speaking, the appearance of BC beyond this Dirac/Weyl paradigm is entirely allowed. The fundamental conditions for the occurrence of BC only involve the crystalline geometry of a material, with no restrictions on the specific properties of its low-energy electronic excitations. Achieving this challenge is of great interest. First, it could in principle result in the coexistence of different mechanisms of BC generation. This could be used, in turn, to endow a single material system with different Berry curvature-mediated effects, as for instance spin- and orbital-Hall effects. Second, searching for BCs without Dirac or Weyl cones might allow the design of materials with interplay of correlated and topological physics – an unexplored frontier in condensed matter physics.

Here, we reach these two milestones in the two-dimensional electron system (2DES) confined at a (111)−oriented oxide interface with a high-temperature trigonal crystalline structure. This model system satisfies the crystalline symmetry properties for a non-vanishing BC. The combination of spin-orbit coupling, orbital degrees of freedom associated with the low-energy t_{2g} electrons, and crystal fields leads to the coexistence of a spin-sourced and an orbital-sourced BC. The two sources are independently probed using two different charge transport diagnostic tools. The observation of the BC-mediated anomalous planar Hall effect [99, 100] grants direct access to the spin-sourced BC whereas nonlinear Hall transport measurements in time-reversal symmetric conditions [101, 102] detect an orbital-mediated Berry curvature dipole – a quantity measured so far only in gapped Dirac systems [101, 102, 105, 106, 107, 108, 109, 110, 111, 103, 104] and three-dimensional topological semimetals [112, 113, 114, 115, 116, 117]. We identify (111) $LaAlO_3$ / $SrTiO_3$ heterointerfaces as an ideal material system because its two-dimensional electron system features many-body correlations and a two-dimensional superconducting ground state [118, 119, 120, 121, 122].

4.2. EXPERIMENTAL DETAILS

SAMPLE GROWTH

The 9 unit cells (u.c.) thick $LaAlO_3$ crystalline layer is grown on the TiO-rich surface of a (111)−oriented $SrTiO_3$ substrate, from the ablation of a high purity (> 99.9%) $LaAlO_3$ sintered target by pulsed laser deposition (PLD), using a KrF excimer laser (wavelength 248 nm). We perform real-time monitoring of the growth by following the intensity oscillations, in a layer-by-layer growth mode, of the first diffraction spot using reflection high-energy electron diffraction (RHEED), as shown in Figure 4.1 (a). This allows us to stop the growth at precisely the critical thickness of 9 unit cells of $LaAlO_3$ [123] necessary for the (111)−$LaAlO_3$/$SrTiO_3$ 2DES to form. The $SrTiO_3$(111) substrate was first heated to 700°C in an oxygen partial pressure of 6×10^{-5} mbar. The $LaAlO_3$ layer was grown in those conditions at a laser fluence of 1.2 J cm^{-2} and at a laser repetition rate of 1 Hz. Following the growth of the $LaAlO_3$ layer, the temperature is ramped down to 500°C before performing a one-hour-long *in situ* annealing in a static background pressure of 300 mbar of pure oxygen, in order to recover the oxygen stoichiometry of the reduced heterostructure. Finally the sample is cooled down at -20°C min^{-1}, and kept in the same oxygen environment at zero heating power for at least 45 minutes.

DEVICES FABRICATION.

The (111) $LaAlO_3$/$SrTiO_3$ blanket films were lithographically patterned into two Hall bars (with dimensions: $W = 40$ μm, $L = 180$ μm), oriented along the two orthogonal crystal axis directions $[\bar{1}10]$ and $[\bar{1}\bar{1}2]$. The Hall bars are defined by electron beam lithography into a PMMA resist, which is used as a hard mask for Argon ion milling which can be seen in Figure 4.1 (c). The dry etching duration is calibrated and timed to be stopped precisely when the $LaAlO_3$ layer is fully removed, in order to avoid the creation of an oxygen-deficient conducting $SrTiO_{3-\delta}$ surface. This leaves an insulating $SrTiO_3$ matrix surrounding the protected $LaAlO_3$/$SrTiO_3$ areas, which host a geometrically confined 2DES.

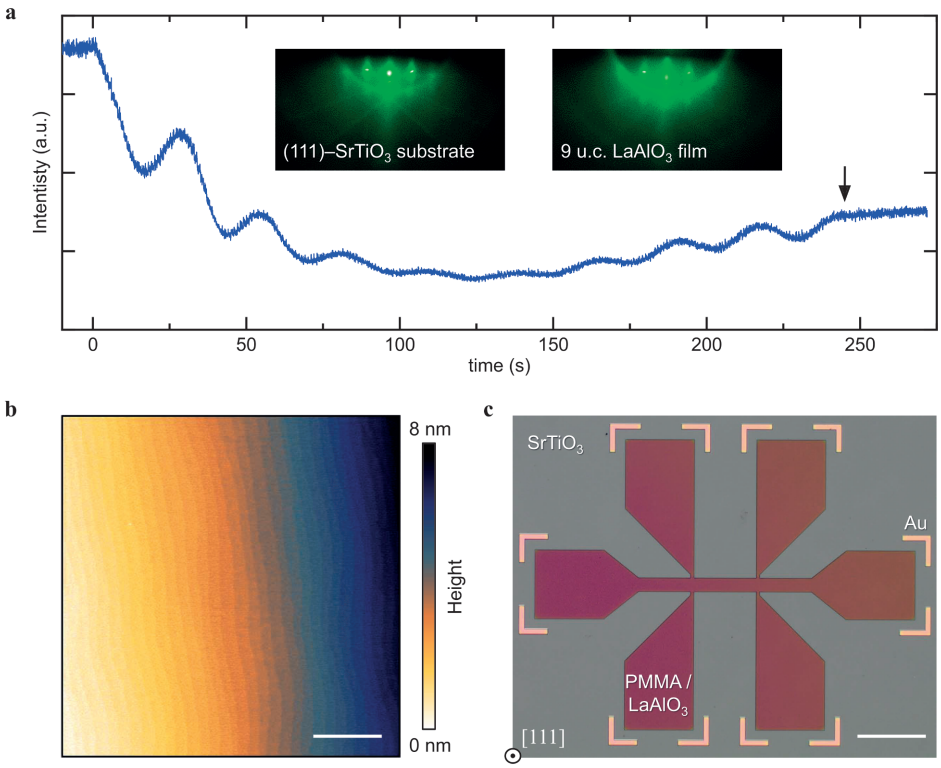

Figure 4.1: Growth, structural characterization and device fabrication of (111)−$LaAlO_3$/$SrTiO_3$ 2DES. (a), *In situ* real-time RHEED monitoring of the layer-by-layer PLD growth of a 9 u.c. $LaAlO_3$ film on a (111)−oriented $SrTiO_3$ substrate. Insets: RHEED patterns acquired prior to (left) and following the film growth (right), highlighting the high crystalline quality of the epitaxial $LaAlO_3$ film. The vertical arrow marks the end of the growth (at 245 s). (b), Atomic force microscopy image of a 9 u.c. thick $LaAlO_3$ film on $SrTiO_3$(111). The film's topography reproduces the characteristic atomically sharp steps-and-terraces structure of the substrate's vicinal surface. Horizontal scale bar: 1 μm. (c), Optical micrograph of a patterned PPMA resist hard mask on a 9 u.c. blanket film of $LaAlO_3$/$SrTiO_3$ (prior to the Ar ion milling step) which ultimately defines the Hall bar device area where the 2DES subsists. Pre-patterned gold markers are used to signify the position of the Hall bars' contact pads, as the optical contrast between the etched area (bare substrate) and the crystalline $LaAlO_3$/$SrTiO_3$ devices is extremely low. Scale bar: 200 μm.

4.3. RESULTS

The samples are lithographically patterned into Hall bars oriented along the two orthogonal principal in-plane crystallographic directions: the $[\bar{1}10]$ and $[\bar{1}\bar{1}2]$ axis as shown in Fig. 4.2(a). The sheet conductance and carrier density of the 2DES are controlled by electrostatic field effects in a back-gate geometry as presented at Fig. 4.2(b). We source an oscillating current (I^{ω}) with frequency $\omega/2\pi$ along each Hall bar, and concomitantly measure the longitudinal response as well as the first or second harmonic transverse voltages in a conventional lock-in detection scheme (see Fig. 4.2a).

The non-trivial geometric properties of the electronic waves in the 2DES derive entirely from the triangular arrangement of the titanium atoms at the (111)$-LaAlO_3/SrTiO_3$ interface (see Fig. 4.2c). Together with the $\mathscr{M}_{\bar{1}10}$ mirror line symmetry, this yields a $\mathscr{C}_{3v}$ crystallographic point group symmetry. As a result of this trigonal crystal field and the concomitant presence of spin-orbit coupling, the entire d-orbital manifold of the Ti atoms located at the center of the surface Brillouin zone (BZ) is split into five distinct Kramers pairs (Supplementary Note I). The energy bands of the pairs are shifted in momentum due to spin-orbit coupling. In their simplest form, they acquire a parabolic dispersion reminiscent of a Rashba 2DES (see Fig. 4.2d). However, the trigonal crystal field brings about a specific hexagonal warping [124, 125] that has a twofold effect. First, for each time-reversal related pair of bands, the Fermi lines acquire an hexagonal “snowflake" shape [126]. Second, and most important, the spin texture in momentum space acquires a characteristic out-of-plane component [127, 128], with alternating meron and antimeron wedges respecting the symmetry properties of the crystal (see Fig. 4.2(e)). This unique spin-momentum locking enables a non-vanishing local BC entirely generated by spin-orbit coupling (Supplementary Note I). The local BC of the spin-split bands of each pair cancel each other at the same crystal momentum. However, there is a region of crystal momenta populated by a single spin band. In this region – the annulus between the two Fermi lines of the system – alternating positive and negative regions of non-vanishing BC are present which is shown in Fig. 4.2(f). Apart from the spin channel, an inherently different source of BC exists. In systems with orbital degrees of freedom, lack of crystal centrosymmetry yields coupling that are linear in k, and mix different atomic orbital states. These orbital Rashba couplings [129] are independent of the presence of spin-orbit coupling. Precisely as its spin counterpart, the orbital Rashba coupling can generate a finite BC [130], but only when all rotational symmetries are broken (see Methods section and Supplementary Note I). With a reduced $\mathscr{C}_s$ symmetry, low-lying t_{2g} orbitals are split into three non-degenerate levels. The corresponding orbital bands then realize a gapped Rashba-like spectrum with protected crossings along the mirror-symmetric lines of the two-dimensional Brillouin zone (BZ) (see Fig. 4.2g). These characteristics result in the appearance of dipolar BC hot-spots and singular pinch points (see Fig. 4.2h). Such orbital sources of Berry curvature are fully active at (111) oxide interfaces thanks to reduced low-temperature symmetries. The cubic-to-tetragonal structural phase transition [131, 132] occurring at 110 K breaks the threefold rotational symmetry along the [111]direction. In addition, the tetragonal to locally triclinic structural distortions at temperatures below $\simeq$ 70 K together with the ferroelectric instability [133] below 50 K is expected to strongly enhance the orbital Rashba strength.

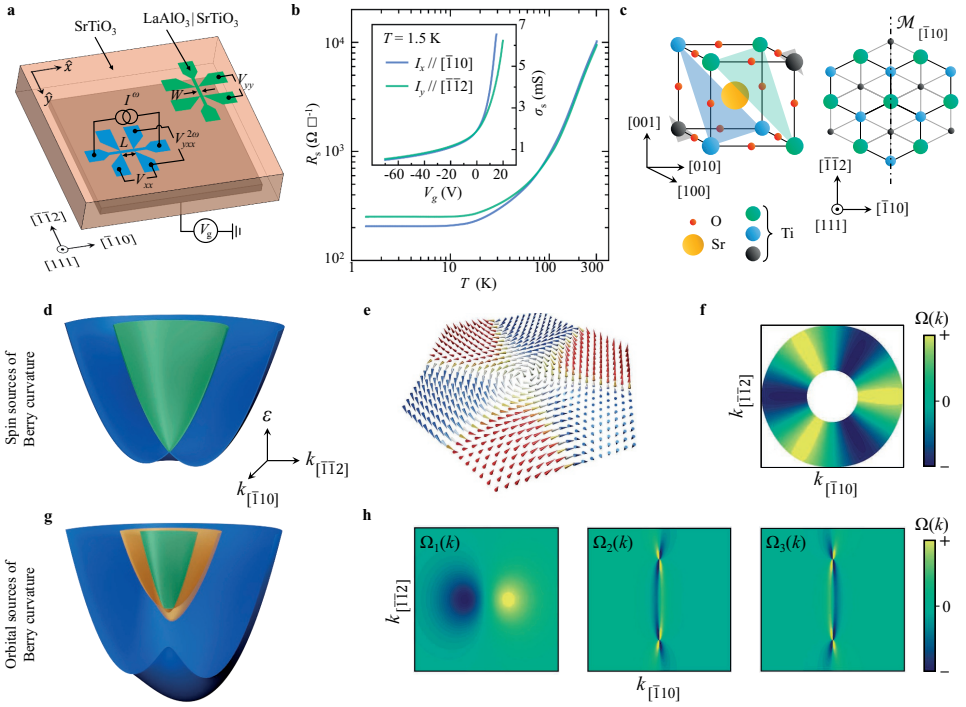

Figure 4.2: **Crystal and model band structures of the (111)−$LaAlO_3$/$SrTiO_3$ 2DES, and basic electrical characterization.** **a**, Schematic layout of the electrical measurement configurations of two Hall bars, hosting a 2DES, and oriented along the $[\bar{1}10]$ and $[\bar{1}\bar{1}2]$ crystallographic axis. W is the width of the channel and L is the distance between the longitudinal voltage probes. V_g stands for the high-voltage source used to tune the 2DES band occupation (Fermi energy) in a back-gate geometry. **b**, Sheet resistance, R_s, versus temperature, T, of the 2DES for the $[\bar{1}10]$ and $[\bar{1}\bar{1}2]$ Hall bar devices, showing a nearly isotropic metallic character. Inset: Sheet conductance, $\sigma_s = R_s^{-1}$, as a function of back-gate voltage, V_g, showing gate-tunability of the 2DES at 1.5 K. **c**, Left: schematic representation of an $SrTiO_3$ perovskite cubic unit cell displaying the nonequivalent (111) titanium planes (shaded areas). Right: top view along the [111] crystallographic direction, of the same unit cell, showing only the Ti atoms. The dash-dotted line indicates the mirror line $\mathscr{M}_{[\bar{1}10]}$. **d**, Schematics of a single pair of spin-split bands forming a Kramers pair at the Γ point up to the Fermi level. **e**, Each spin band is characterised by a non-trivial spin texture with an out-of-plane spin components induced by the effect of trigonal warping. **f**, Exclusion plot of the Berry curvature Ω_k over the Fermi surfaces of the two spin sub-bands. **g**, Schematics band structure of spin-orbit free orbital bands corresponding to t_{2g} electrons subject to a $\mathscr{C}_s$ crystal field. At the center of the BZ all levels are split. The orbital Rashba coupling $\propto \alpha_m$ leads to mirror-symmetry-protected crossings.

The orbital-sourced BC is expected to be very stiff in response to externally applied in-plane magnetic fields due to the absence of symmetry-protected orbital degeneracies. In contrast, the spin-sourced BC is significantly more susceptible to planar magnetic fields. As shown in Fig. 4.3(a,b), an in-plane magnetic field is capable of generating a BC hot-spot within the Fermi surface annulus. This BC hot-spot corresponds to a field-induced avoided level crossing between the two spin-split bands that occurs whenever the applied magnetic field breaks the residual crystalline mirror symmetry. The momentum-integrated net Berry curvature is then non-zero (Supplementary Note II), and yields a transverse Hall conductance satisfying the antisymmetric property $\sigma_{xy}\rho_{yx} = -1$, even in the absence of any Lorentz force. This effect, theoretically predicted in Refs. [99, 100] and known as the anomalous planar Hall effect (APHE), is different in nature with respect to the conventional planar Hall effect, which is instead related to the anisotropy in the longitudinal magnetoresistance and thus characterised by a symmetric response $\sigma_{xy}(B) = \sigma_{xy}(-B)$. Figure 4.3(c) shows the transverse (Hall) resistance measured with a current applied along the $[\bar{1}\bar{1}2]$ crystal direction and with collinear current and magnetic field. This ensures a vanishing symmetric planar Hall effect [99]. At fields well-below 4 T, a small signal increasing linearly with the field strength is detected. This feature can be attributed to an out-of-plane misalignment of the magnetic field smaller than 1.5° (Supplementary Note III). Above a magnetic field threshold instead, a large transverse Hall signal sharply emerges (see also Extended Data Fig. 4.8. At even larger fields this response saturates. Electrostatic gating is found to decrease the magnetic field threshold and promotes a non-monotonic evolution of the response amplitude (Fig. 4.3(d,e)). The experimental features of this Hall response can be captured by onsidering a single pair of spin-split bands coupled to the external field by the Zeeman interaction. In this picture, the sudden onset of the transverse response is associated to the appearance of the BC hot-spot inside the Fermi surface annulus occurring at a critical magnetic field strength (Supplementary Note II). Magnetoconductance measurements in the weak antilocalization regime (Extended Data Figs. 4.9, 4.10 show that the onset of the transverse Hall signal coincides precisely with the appearance of the spin-sourced BC hot-spot. The non-monotonic behavior of the transverse response as a function of electrostatic gating and magnetic field strength can be also ascribed to the BC origin of the Hall response. The angular dependence of the transverse resistance as shown in Fig. 4.3(f) indicates a vanishing transverse linear conductivity when the planar magnetic field is along the $[\bar{1}10]$ direction, due to the mirror symmetry $\mathscr{M}_{[\bar{1}10]}$. This is independent on whether the driving current is along the $[\bar{1}10]$ or the $[\bar{1}\bar{1}2]$ direction. Note that the two angular dependencies are related to each other by a 180° shift in agreement with the Onsager reciprocity relations [134].

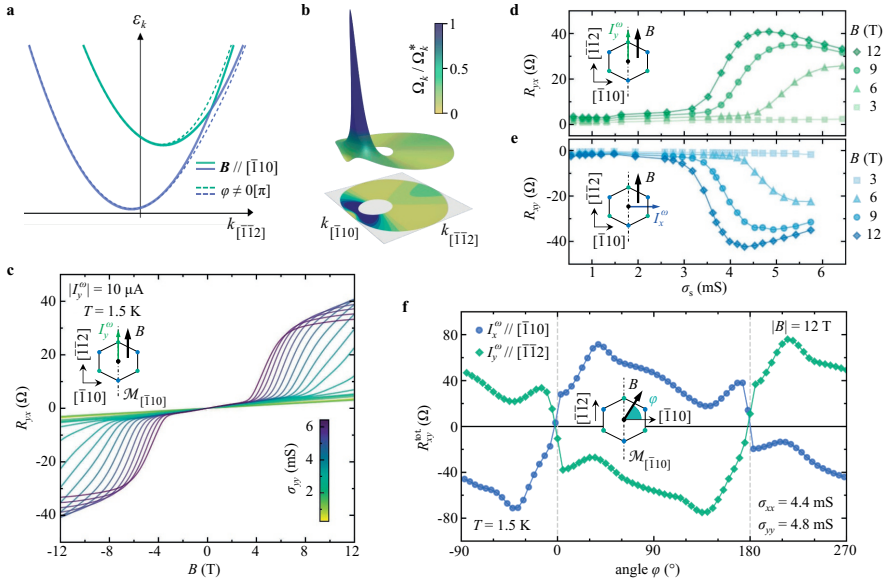

Figure 4.3: **Anomalous planar Hall response of the 2DES induced by the spin-sourced Berry curvature. a**, Schematic energy dispersion of the spin-split bands along the mirror line of the Brillouin zone $k_{[\bar{1}10]} = 0$ in the presence of a planar magnetic field. When the latter is oriented along the $[\bar{1}10]$ direction there is a mirror-symmetry protected crossing of the spin-split bands that evolves into an anticrossing for other directions of the magnetic field. The angle φ is defined by the orientation of the magnetic field w.r.t. the $[\bar{1}10]$ crystallographic direction (*c.f.* schematic inset in panel **f**). **b**, Sketch of the spin-sourced Berry curvature normalised magnitude $\Omega_k/\Omega_k^{\star}$ when the magnetic field is directed along the $[\bar{1}\bar{1}2]$ direction. When the anticrossing point enters the Fermi surface annulus, the integral of the curvature is strongly enhanced and the anomalous planar Hall response reaches its maximum. **c**, Experimentally measured field-antisymmetric planar Hall resistance $R_{xy} = V_{xy}^{\omega}/I_x^{\omega}$ at $T = 1.5$ K, with I_y^{ω} along $[\bar{1}\bar{1}2] \parallel B$ (see inset schematic), for different sheet conductance values σ_{yy} indicated by the inset colored scale bar. **d**, Corresponding dependence of R_{yx} versus σ_{yy} showing a non-monotonic behavior for fixed values of $B > 3$ T, and an onset above a threshold value of σ_{yy}. **e**, Dependence of the field-antisymmetric contribution R_{xy} versus σ_{xx} for I_x^{ω} along $[\bar{1}10] \perp B$ (see Extended Data Fig. 4.6). **f**, In-plane angular dependence of the raw total transverse resistance response $R_{xy}^{tot.}$, *i.e.* not field-(anti)symmetrised, for the two Hall bar devices at $B = 12$ T. The planar Hall response obeys Onsager relation $R_{xy}(B) = R_{yx}(-B)$, as seen by the near identical angular dependence upon imposing a $\pm\pi$ translation to either curve. Remarkably, $R_{xy}^{tot.}$ goes to zero at $\varphi = 0°$ and $\varphi = 180°$, *i.e.* when the mirror symmetry is preserved even in the presence of an external magnetic field.

The absence of linear conductivity makes this configuration the ideal regime to investigate the presence of nonlinear transverse responses, which are symmetry-allowed when the driving current is collinear with the magnetic field (Supplementary Note II). We have therefore performed systematic measurements of the second harmonic, *i.e.* at 2ω, transverse responses (see Fig. 4.4 a,b) by sourcing the a.c. current along the $[\bar{1}10]$ direction.

We have subsequently disentangled the field-antisymmetric $R^{2\omega}_{y,as} = \left[R^{2\omega}_{y}(B) - R^{2\omega}_{y}(-B)\right]/2$, and the field-symmetric contributions $R^{2\omega}_{y,sym} = \left[R^{2\omega}_{y}(B) + R^{2\omega}_{y}(-B)\right]/2$, since they originate from distinct physical effects. In particular, the antisymmetric part contains a semiclassical contribution that only depends upon the conventional group velocity of the carriers at the Fermi level (Supplementary Note II). Conversely, the symmetric part originates from the anomalous velocity term of the carriers. It is a purely quantum contribution and can be expressed in terms of a Berry curvature dipole (BCD). We observe the following features in Fig. 4.4a,b. The semiclassical antisymmetric contribution has a sudden onset above a characteristic magnetic field (see Fig. 4.4a) that is sensitive to gating (see Fig. 4.4c). The gate dependence displays a monotonic growth consistent with its physical origin. On the contrary, the symmetric contribution displays the typical non-monotonous gate and field amplitude dependence (see Fig.4.4d) of BC-mediated effects. The gate dependence of the nonlinear symmetric contribution obtained by sourcing the current along the $[\bar{1}\bar{1}2]$ direction is instead strongly suppressed and featureless (see Fig.4.4e). This is consistent with a $[\bar{1}10]-$ oriented BCD, which gives a vanishing response in this configuration. We note that the symmetric nonlinear transverse resistance has a characteristic quadratic current-voltage ($I^{\omega} - V^{2\omega}$), which, combined with the response at double the driving frequency, establishes its second-order nature (see Fig. 4.4f).

The fact that only the symmetric contribution persists even in the zero-field limit (see Fig. 4.4a,b) indicates the presence of a finite BCD in the absence of externally applied magnetic fields, and thus of a nonlinear Hall effect in time-reversal symmetric conditions. To support the existence of a finite BCD with time-reversal symmetry, we have evaluated individually the dipole originating from the spin-sourced BC and the dipole related to the orbital-sourced BC (see the Methods section). Figure 4.5a shows that in all the parameter space of our low-energy theory model, the spin-sourced BCD is two order of magnitudes smaller than the orbital-sourced BCD. The latter exceeds the inverse characteristic Fermi wavenumber ${k_F}^{-1} \sim 0.5$ nm. Beside the intrinsic contribution to the BCD, the nonlinear Hall response with time-reversal symmetry also contains disorder-induced contributions [135, 102] due to nonlinear skew and side-jumps scattering.

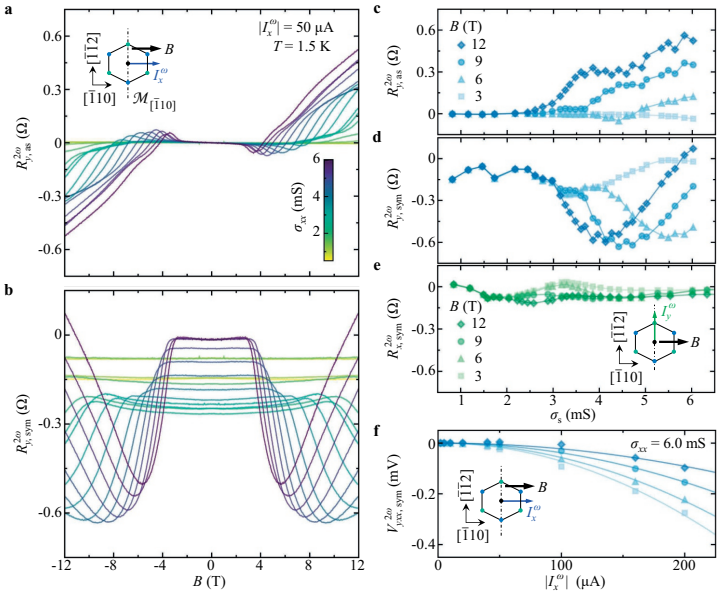

Figure 4.4: **Nonlinear Hall response of the 2DES in a planar magnetic field.** **a**,**b**, Field-antisymmetric, $R^{2\omega}_{y,as}$ (**a**), and field-symmetric $R^{2\omega}_{y,sym}$ (**b**) second harmonic transverse resistance responses, for I^ω_x along $[\bar{1}10] \parallel B$, and for different values of the sheet conductance σ_{xx}. **c**, **d**, Corresponding dependence of $R^{2\omega}_{y,as}$ and $R^{2\omega}_{y,sym}$, respectively, versus σ_{xx} for different values of the in-plane magnetic field B. The field-symmetric nonlinear transverse resistance displays a strong non-monotonic response, attributed to a Zeeman-induced Berry phase contribution. **e**, Field-symmetric second harmonic transverse resistance response, $R^{2\omega}_{x,sym}$, for I^ω_y along $[\bar{1}\bar{1}2] \perp B$ versus sheet conductance σ_{yy} at fixed values of the planar magnetic field (see also Extended Data Fig.4.7). The full scale ordinate axis is chosen to be the same as for panel **d**, for better comparison. **f**, Field-symmetric nonlinear transverse second harmonic voltage $V^{2\omega}_{yxx,sym}$ versus the a.c. current amplitude I^ω_x, at fixed values of B (see Extended Data Fig. 4.11). Solid lines are quadratic fits.

We experimentally access such contributions by measuring the longitudinal signal $V^{2\omega}_{yyy}$ that is symmetry-allowed but does not possess any intrinsic BCD contribution. As displayed in Fig. 4.5b, the strong difference in amplitude between the longitudinal signal and the transverse $V^{2\omega}_{yxx}$ signal over a large driving current range proves both the absence of threefold rotation symmetry and a nonlinear Hall effect completely dominated by the intrinsic BCD. The anisotropy between longitudinal and transverse nonlinear signals also allows us to exclude a leading role played by thermoelectric effects due to Joule heating (see also inset of Fig. 4.5b). We further observe that both the longitudinal $V^{2\omega}_{xxx}$ and transverse $V^{2\omega}_{xyy}$ responses have an amplitude comparable with the longitudinal signal $V^{2\omega}_{yyy}$, thus suggesting their disorder-induced nature. We point out that the finite amplitudes of $V^{2\omega}_{xxx}$ and $V^{2\omega}_{xyy}$ imply $\mathscr{M}_{\bar{1}10}$ symmetry breaking (Supplementary Note II). This can be related to the mirror breaking arrangements of the oxygen atoms caused by the antiferrodistortive octahedron rotations. It might be also due to the presence of structural domain patterns appearing at the cubic-to-tetragonal structural transition. We have systematically verified the occurrence of a sizeable nonlinear transverse response over the full range of sheet conductances, and concomitantly observed a large difference between the two nonlinear transverse conductivity tensor component χ_{yxx} and χ_{xyy}, as seen in Fig. 4.5c. This further proves a main intrinsic BCD contribution to the nonlinear Hall response. By further evaluating the momentum relaxation time, τ (Supplementary Note II), we can estimate the size of the Berry curvature dipole using (see Methods section):

$$D_x = \frac{2\hbar^2}{e^3\tau}\,\chi_{yxx}\,. \tag{4.1}$$

The resulting BCD (see Fig. 4.5d) is two order of magnitudes larger than the dipole observed in systems with massive Dirac fermions, such as bilayer WTe_2 [106, 105] and – over a finite density range – a factor two larger than the dipole observed in corrugated bilayer graphene [107]. We attribute the large magnitude of the effect to the fact that the orbital-sourced BC is naturally equipped with a large dipolar denisty due to the presence of singular pinch points and hot-spots with dipolar arrangements. We also monitored the temperature dependence of the transverse conductivity tensor components χ_{yxx} and χ_{xyy} (see Fig. 4.5e) and the corresponding behavior of the BCD D_x (see Fig. 4.5f). All these quantities rapidly drop approaching 30 K, *i.e.* the temperature above which the strong polar quantum fluctuations of $SrTiO_3$ vanish. This further establishes the orbital Rashba coupling as the physical mechanism behind the orbital-sourced BC.

The pure orbital-based mechanism of BCD featured here paves the way to the atomic scale design of quantum sources of nonlinear electrodynamics persisting up to room-temperature. Oxide-based 2DES could be for instance combined with a room-temperature polar ferroelectric layer, triggering symmetry lowering and thus inducing orbital Rashba coupling, by interfacial design. This and other alternative platforms combining a low symmetric crystal with orbital degrees of freedom and polar modes, including room-temperature polar metals [136] and conducting ferroelectric domain walls, are candidate oxide architectures to perform operations such as rectification [137] and frequency mixing. Moreover, multiple sources of Berry curvature can be implemented for combined optoelectronic and spintronic functionalities in a single material system: photogalvanic currents due to the orbital-sourced BC can be employed to create spin-Hall voltages ex-

ploiting the spin-sourced BC. Our study also establishes a general approach to generate topological charge distributions in strongly correlated materials, opening a vast space for exploration at the intersection between topology and correlations.

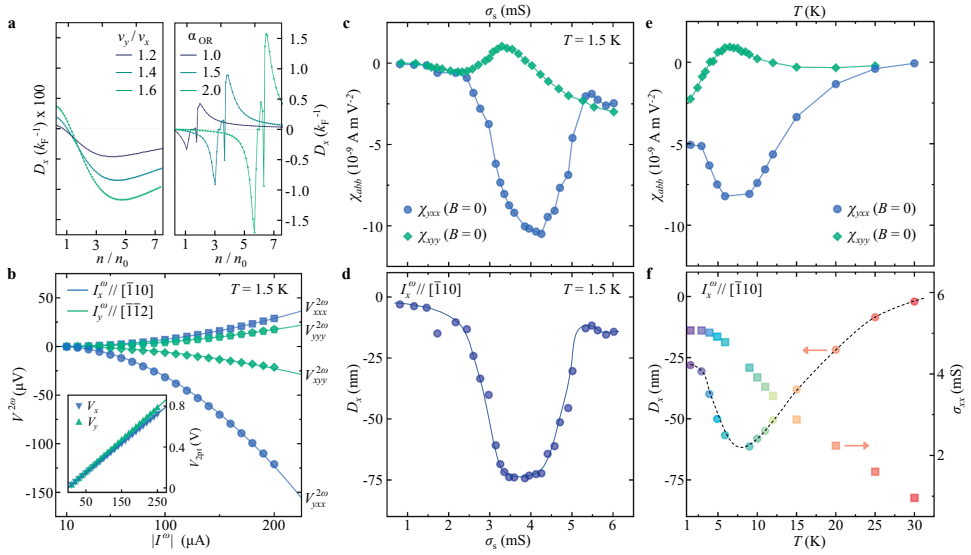

Figure 4.5: **Berry curvature dipole under time-reversal symmetric conditions a**, Calculated spin-sourced and orbital-sourced Berry curvature dipole as a function of the sheet carrier density. The spin-sourced dipole (left panel) has been evaluated for different strength of the rotational symmetry breaking distortion $\propto v_y/v_x$ (see Methods section), whereas the orbital-sourced dipole (right panel) has been computed varying the strength of the orbital Rashba coupling α_{OR}. In both cases, the dipole has a strongly non-monotonic behavior, goes to zero for large densities, and is directed along the [$\bar{1}$10] direction. The orbital-sourced dipole is two order of magnitude larger in all the density range. **b**, Measured $I^\omega - V^{2\omega}$ characteristics at zero magnetic field. Longitudinal $V^{2\omega}_{xxx(yyy)}$ and transverse $V^{2\omega}_{yxx(xyy)}$ voltage drops versus the a.c. excitation bias $|I^\omega|$ for $I^\omega_{x(y)}$ along [$\bar{1}$10] ([$\bar{1}\bar{1}$2], respectively) at $\sigma_{xx} \approx \sigma_{yy} \approx 4.5-4.6$ mS. Solid lines are quadratic fits. Inset: Linear two-terminal $I-V$ characteristics highlighting the Ohmic behaviour of the electrical contacts to the 2DES. Solid lines are linear fits. **c**, Sheet conductance dependence of the measured nonlinear transverse conductivity tensor elements χ_{yxx} and χ_{xyy} for I^ω sourced along the two orthogonal in-plane principal crystallographic directions. **d**, Berry curvature dipole's magnitude, D_x, under time-reversal symmetric conditions ($B = 0$). The BCD estimated after Eq. (1) is found to peak strongly at intermediate doping levels, where it reaches a maximum value of nearly -75 nm. **e**, Temperature dependence of the nonlinear transverse conductivities χ_{yxx} and χ_{xyy}. The two quantities go to zero as the temperature increases and strontium titanate recovers a higher (non-polar tetragonal) crystal symmetry. Concomitantly, the BCD is forced to vanish by symmetry. **f**, Temperature dependence of the BCD, D_x (left axis), and corresponding change in sheet conductance $\sigma_{xx}(T)$ of the 2DES (right axis). Solid and dashed lines in panels **d** and **f** are guides to the eye.

4.4. EXTENDED DATA FIGURES

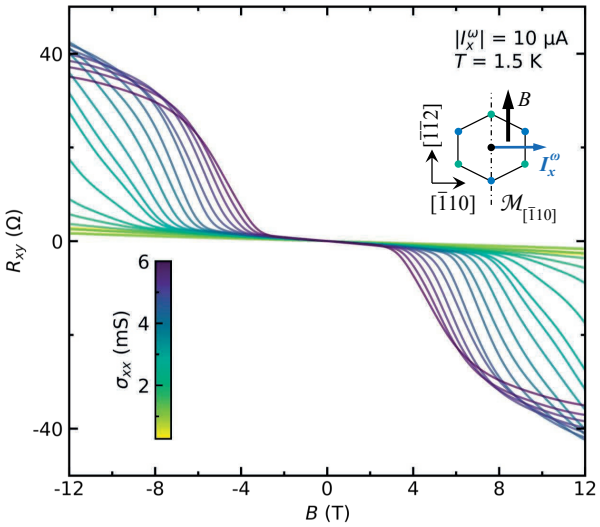

Figure 4.6: **Hall effect in a planar magnetic field.** Experimentally measured field-antisymmetric transverse magnetoresistance $R_{yx} = V_{yx}^{\omega}/I_y^{\omega}$ at T = 1.5 K, with I_x^{ω} along $[\bar{1}10] \perp B$ (see inset schematic), for varying sheet conductance values σ_{xx} (indicated by the inset colored scale bar), and tuned via electrostatic field effect in a back-gate geometry.

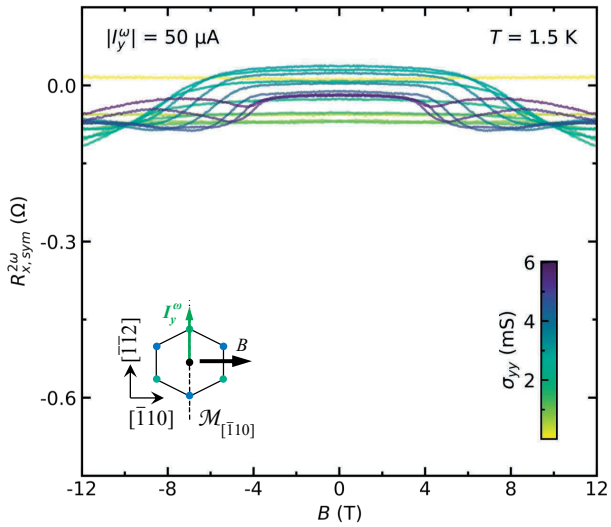

Figure 4.7: **Nonlinear Hall response in a planar magnetic field.** Experimentally measured field-symmetric nonlinear transverse magnetoresponse $R^{2\omega}_{x}$ at T = 1.5 K with I^{ω}_{y} along [$\bar{1}\bar{1}$2] $\perp B$ (see inset schematic), for varying sheet conductance values σ_{yy} (indicated by the inset colored scale bar). The full scale ordinate axis is chosen to be the same as for panel **b** of Fig. 4.4, for better comparison, and highlights the comparatively small nonlinear Hall response when the current is sourced along the $\mathcal{M}_{\bar{1}10}$ mirror line corresponding to a symmetry demanded zero BCD.

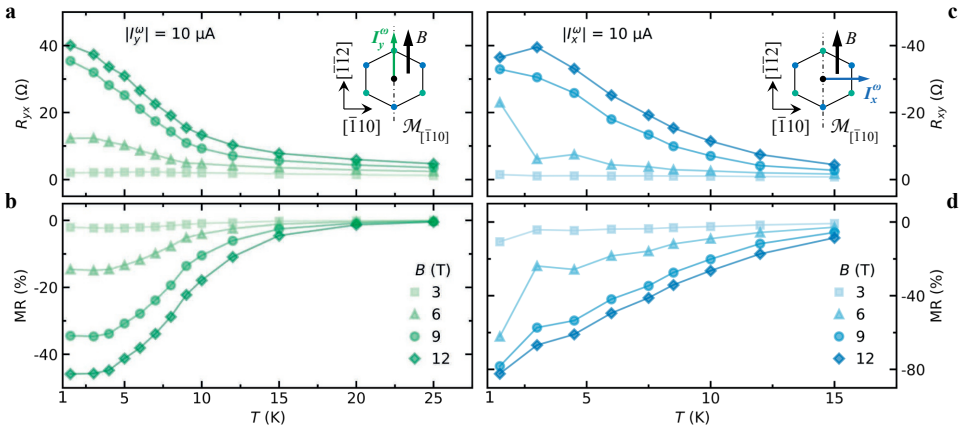

Figure 4.8: **Temperature dependence of the Hall and longitudinal magnetoresistances in a planar magnetic field.** Temperature dependent planar Hall resistance (**a**,**c**) and longitudinal MR (**b**,**d**) in the linear response regime for various strength of the in-plane magnetic field (and at fixed gate-voltage), with I^{ω}_{y} along [$\bar{1}\bar{1}$2] $\parallel B$ (**a-b**) and I^{ω}_{x} along [$\bar{1}$10] $\perp B$ (**c-d**). Both R_{yx} and R_{xy}, as well as the corresponding longitudinal MR, asymptotically go to zero as the temperature increases toward strontium titanate's nonpolar tetragonal phase (above ≈ 30 K).

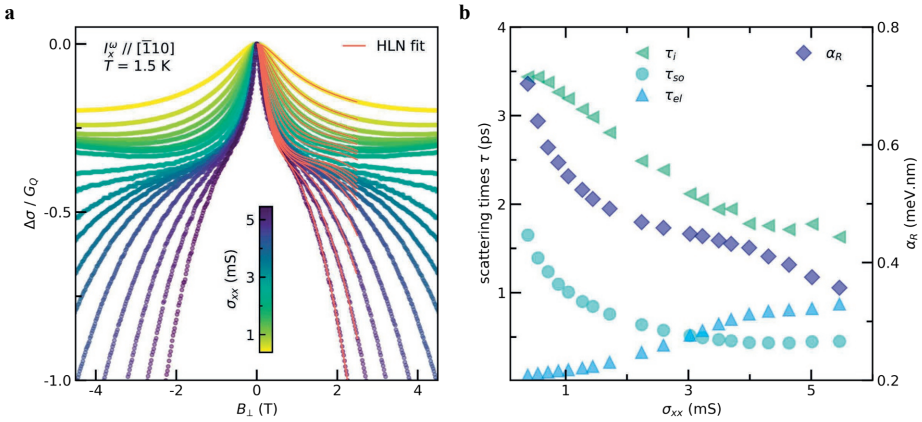

Figure 4.9: **Weak antilocalization regime and Rashba spin-orbit coupling. a**, Gate-modulated magnetoconductance curves (normalized to the quantum of conductance G_Q) for I_x^{ω} along $[\bar{1}10]$ (see also Supplementary Note III for WAL measurements along $[\bar{1}\bar{1}2]$). Hikami-Larkin-Nagaoka fits (solid red lines) are performed following Eq.4.3. $B_\perp$, the out-of-plane magnetic field. **(c)** Left axis: Experimentally estimated momentum, inelastic and spin-orbit relaxation times, τ_{el} (named τ throughout the manuscript), τ_i and τ_{so}, respectively. Right axis: Strength of the Rashba spin-orbit coupling α_R versus sheet conductance σ_{xx}.

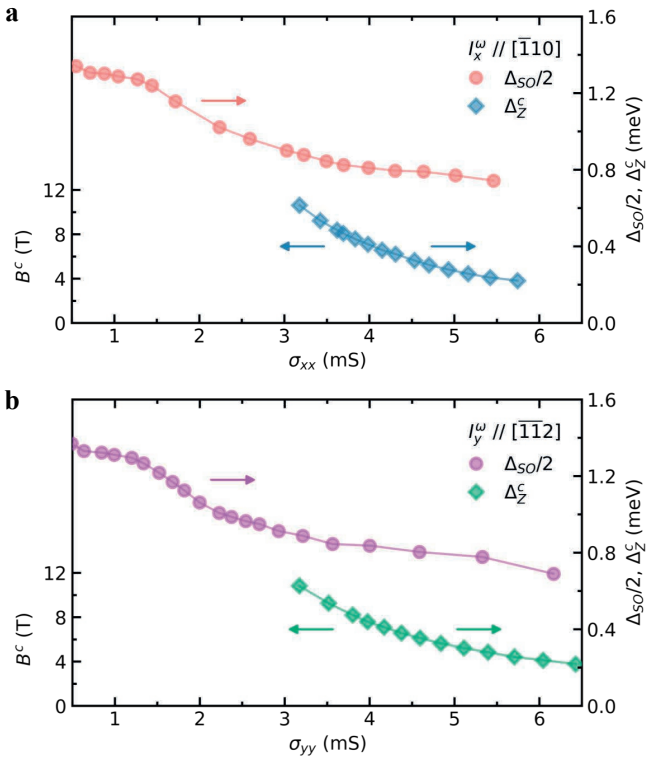

Figure 4.10: **Effective Zeeman energy and Rashba spin-orbit energy of the 2DES. a-b**, Right axis: Sheet conductance dependence of the Rashba spin-orbit energy $\Delta_{so}/2 = \alpha_R k_F$ and effective Zeeman energy $\Delta_Z^c = g\mu_B B^c/2$ at the critical in-plane field B^c (left axis), for I_x^ω along [$\bar{1}$10] (panel **a**) and for I_y^ω along [$\bar{1}\bar{1}$2] (panel **b**). See Supplementary Note III for details regarding the determination of B^c.

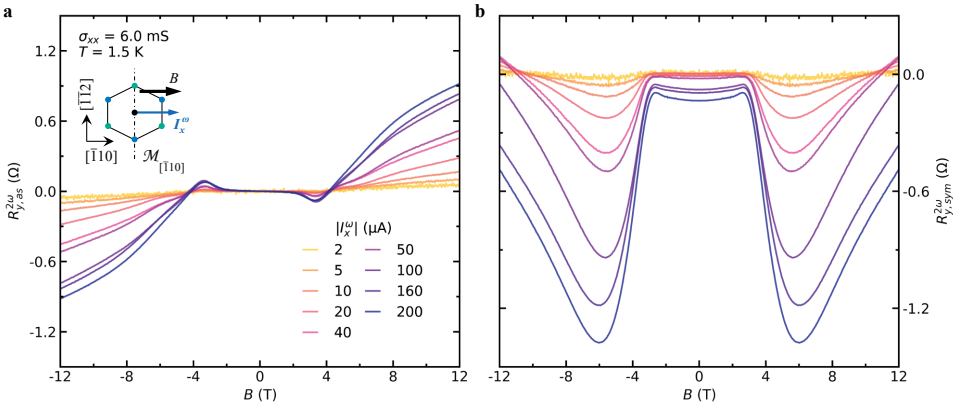

Figure 4.11: **Current bias dependent nonlinear transverse signal in a planar magnetic field. a**,**b**, Field-antisymmetric, $R_{y,as}^{2\omega}$, and field-symmetric $R_{y,sym}^{2\omega}$ second harmonic transverse resistance responses, for various magnitudes of the excitation a.c. current along [$\bar{1}$10](∥ B, see inset schematic).

AUTHOR CONTRIBUTION STATEMENT

A.D.C. proposed and supervised the experiments. C.O. proposed the theory models and supervised their analysis. E.L. grew the crystalline LaAlO3 thin films by pulsed laser deposition and performed the structural characterizations. E.L. and Y.G.S. lithographically patterned the samples, performed the magnetotransport experiments and analysed the experimental data with help from T.C.v.T. and U.F. R.B. and M.T.M. performed the BC and semiclassical transport calculations with help from M.C., C.N. and C.O. C.O., E.L., R.B. and A.D.C. wrote the manuscript, with input from all the authors.

METHODS

ELECTRICAL TRANSPORT MEASUREMENTS.

The Hall bars are connected to a chip carrier by ultrasonic wedge-bonding technique whereby the Aluminum wires form ohmic contacts to the 2DES through the $LaAlO_3$ overlayer. The sample is anchored to the chip carrier by homogeneously coating the backside of the $SrTiO_3$ substrate with silver paint. A d.c. voltage V_g is sourced between the silver back-electrode and the desired Hall bar device to enable electrostatic field-effect gating of the 2DES, leveraging the large dielectric permittivity of strontium titanate at low-T ($\approx 2\,\mathrm{x}\,10^4$ below 10 K) [138, 139]. Non-hysteretic dependence of σ_{xx} (σ_{yy}) on V_g is achieved following an initial gate-forming procedure [140].

Standard four-terminal electrical (magneto-)transport measurements were performed at 1.5 K in a liquid Helium-4 flow cryostat, equipped with a superconducting magnet (maximum magnetic field $B = \pm 12$ T). An a.c. excitation current $I^\omega \propto |I^\omega| \cdot \sin(\omega t)$, of frequency $\omega/(2\pi) = 17.77$ Hz, is sourced along the desired crystallographic direction. The sheet resistance, $R_s = \sigma_{xx}^{-1}$, of a Hall bar device is related to the first harmonic longitudinal voltage drop V_{xx} according to: $R_s = (V_{xx}/I_x)(W/L)$. When the a.c. current is sourced along $\hat{\boldsymbol{x}} \parallel [\bar{1}10]$ ($\hat{\boldsymbol{y}} \parallel [\bar{1}\bar{1}2]$, respectively), we make use of a standard lock-in detection technique to concomitantly measure the first harmonic longitudinal response V_{xx} (V_{yy}), and either the in-phase first-harmonic V_{xy}^ω (V_{yx}^ω) or out-of-phase second harmonic $V_{yxx}^{2\omega}$ ($V_{xyy}^{2\omega}$) transverse voltages (see Fig. 4.2a). We define the first and second harmonic transverse resistances as $R_{xy}^\omega = V_{xy}^\omega/|I_x^\omega|$ and $R_y^{2\omega} = V_{yxx}^{2\omega}/|I_x^\omega|^2$, respectively. First and second harmonic measurements are performed at 10 μA and 50 μA respectively.

We systematically decompose both the first and second harmonic magneto-responses into their field-symmetric, $R_{sym}^{(2)\omega}$, and field-antisymmetric, $R_{as}^{(2)\omega}$, contributions according to:

$$R_{sym}^{(2)\omega} = \left[R^{(2)\omega}(B) + R^{(2)\omega}(-B)\right]/2\,, \tag{4.2a}$$

$$R_{as}^{(2)\omega} = \left[R^{(2)\omega}(B) - R^{(2)\omega}(-B)\right]/2\,. \tag{4.2b}$$

In particular, the first harmonic transverse resistance is purely field-antisymmetric, hence we chose the simplified notation $R_{xy} \equiv R_{xy,as}^{\omega}$.

ESTIMATION OF THE RASHBA SPIN-ORBIT ENERGY FROM MAGNETOCONDUCTANCE MEASUREMENTS IN THE WEAK ANTILOCALIZATION REGIME.

In a 2DES, in the presence of a spin relaxation mechanism induced by an additional spin-orbit interaction, the conductance is subject at low temperature to weak localization corrections. Extended Data Fig. 4.9**a** shows the gate-modulated magnetoconductance curves of the 2DES, which exhibit a characteristic low field weak antilocalization (WAL) behaviour. The magnetoconductance curves, normalized to the quantum of conductance $G_Q = e^2/(\pi\hbar)$, are fitted using a Hikami-Larkin-Nagaoka (HLN) model that expresses the change of conductivity $\Delta\sigma(B_\perp) = \sigma(B_\perp) - \sigma(0)$ of the 2DES under an external out-of-plane magnetic field $B_\perp$, in the diffusive regime (with negligible Zeeman splitting), as [141, 142]:

$$\begin{aligned}\frac{\Delta\sigma(B_\perp)}{G_Q} = &-\frac{1}{2}\Psi\left(\frac{1}{2}+\frac{B_i}{B_\perp}\right)+\frac{1}{2}\ln\left(\frac{B_i}{B}\right)\\ &+\Psi\left(\frac{1}{2}+\frac{B_i+B_{so}}{B_\perp}\right)-\ln\left(\frac{B_i+B_{so}}{B_\perp}\right)\\ &+\frac{1}{2}\Psi\left(\frac{1}{2}+\frac{B_i+2B_{so}}{B_\perp}\right)-\frac{1}{2}\ln\left(\frac{B_i+2B_{so}}{B_\perp}\right)\\ &-A_k\frac{\sigma(0)}{G_Q}B_\perp^2\,.\end{aligned} \tag{4.3}$$

where Ψ is the digamma function, $B_{i,so}=\hbar/\left(4eD\tau_{i,so}\right)$ are the effective fields related to the inelastic and spin-orbit relaxation times (τ_i and τ_{so} respectively), with $D=\pi\hbar^2\sigma(0)/(e^2m^*)$ the diffusion constant. The last term in Eq. (3), proportional to $B_\perp^2$, contains A_k, the so-called Kohler coefficient, which accounts for orbital magnetoconductance.

Hence, from the fit to the WAL magnetoconductance curves, the effective Rashba spin-orbit coupling α_R can be calculated as:

$$\alpha_R=\hbar^2/\left[2m^*\sqrt{(D\tau_{so})}\right], \tag{4.4}$$

based on a D'yakonov-Perel' spin relaxation mechanism [142]. A summary of the dependence of the extracted parameters on the 2DES' sheet conductance is plotted in Extended Data Fig. 4.10b. The spin-orbit energy Δ_{so} can then be estimated according to:

$$\Delta_{so}=2\alpha_R k_F\,, \tag{4.5}$$

where, in 2 dimensions, the Fermi wavevector is given by $k_F=\sqrt{2\pi n_{2D}}$, assuming a circular Fermi surface. The sheet carrier density n_{2D} is experimentally obtained for each doping value from the (ordinary) Hall effect (Supplementary Note III), measured concomitantly with the magnetoconductance traces.

SPIN-SOURCED AND ORBITAL-SOURCED BERRY CURVATURE DIPOLE CALCULATIONS.

We first estimate the Berry curvature dipole due to spin-sources in time-reversal symmetric condition as a function of carrier density considering the low-energy Hamiltonian for a single Kramers' related pair of bands (Supplementary Note I):

$$\mathscr{H}=\frac{\boldsymbol{k}^2}{2m(\boldsymbol{k})}-\alpha_R\boldsymbol{\sigma}\cdot\boldsymbol{k}\times\hat{\mathbf{z}}+\frac{\lambda}{2}(k_+^3+k_-^3)\sigma_z\,. \tag{4.6}$$

where the momentum dependent mass can be negative close to Γ point (Supplementary Note I). Although this model Hamiltonian is equipped with a finite Berry curvature, its dipole is forced to vanish by the threefold rotation symmetry (Supplementary Note I). We capture the rotation symmetry breaking of the low-temperature structure at the leading order by assuming inequivalent coefficients for the spin-orbit coupling terms linear in momentum. In other words we make the substitution $\alpha_R\left(\sigma_x k_y-\sigma_y k_x\right)\rightarrow$

$v_y k_y \sigma_x - v_x k_x \sigma_y$. Since the dipole is a pseudo-vector, the residual mirror symmetry $\mathscr{M}_x$ forces it to be directed along the $\hat{\boldsymbol{x}}$ direction. In the relaxation time approximation it is given by

$$D_x = \int_{\boldsymbol{k}} \partial_{k_x} \Omega_z(\boldsymbol{k}) \tag{4.7}$$

with Ω_z the Berry curvature of our two-band model which we write in dimensionless form by measuring energies in units of $k_F^2/2m(k_F)$, lengths in units of $1/k_F$ and densities in units of $n_0 = k_F^2/2\pi$. Here, k_F is a reference Fermi wavevector. For simplicity, we have considered a positive momentum-independent effective mass. For the Berry curvature dipole shown in Fig. 4.5a the remaining parameters have been chosen as $v_x = 0.4$, $v_y = (1.2, 1.4, 1.6) \times v_x$ and $\lambda = 0.1$. Moreover, we account for the orbital degeneracy by tripling the dipole of a single Kramers' pair. This gives an upper bound for the spin-sourced BCD.

We have also evaluated the BCD due to orbital sources considering the low-energy Hamiltonian for spin-orbit free t_{2g} electrons derived from symmetry principles (Supplementary Note I) and reading

$$\begin{aligned} \mathscr{H}(\mathbf{k}) \quad = \quad & \frac{\hbar^2 \mathbf{k}^2}{2m} \Lambda_0 + \Delta \left(\Lambda_3 + \frac{1}{\sqrt{3}} \Lambda_8 \right) + \Delta_m \left(\frac{1}{2} \Lambda_3 - \frac{\sqrt{3}}{2} \Lambda_8 \right) \\ & - \alpha_{OR} \left[k_x \Lambda_5 + k_y \Lambda_2 \right] - \alpha_m k_x \Lambda_7, \end{aligned} \tag{4.8}$$

where we introduced the Gell-Mann matrices

$$\Lambda_2 = \begin{pmatrix} 0 & -i & 0 \\ i & 0 & 0 \\ 0 & 0 & 0 \end{pmatrix} \quad , \quad \Lambda_3 = \begin{pmatrix} 1 & 0 & 0 \\ 0 & -1 & 0 \\ 0 & 0 & 0 \end{pmatrix}$$

$$\Lambda_5 = \begin{pmatrix} 0 & 0 & -i \\ 0 & 0 & 0 \\ i & 0 & 0 \end{pmatrix} \quad , \quad \Lambda_7 = \begin{pmatrix} 0 & 0 & 0 \\ 0 & 0 & -i \\ 0 & i & 0 \end{pmatrix}$$

$$\Lambda_8 = \begin{pmatrix} \frac{1}{\sqrt{3}} & 0 & 0 \\ 0 & \frac{1}{\sqrt{3}} & 0 \\ 0 & 0 & \frac{-2}{\sqrt{3}} \end{pmatrix}.$$

and Λ_0 the identity matrix. In the Hamiltonian above, Δ is the splitting between the a_{1g} singlet and the e'_g doublet resulting from the t_{2g} orbitals in a trigonal crystal field. Δ_m is the additional splitting between the doublet caused by the rotational symmetry breaking. Finally, α_{OR} and α_m are the strength of the orbital Rashba coupling. Note that in the presence of a threefold rotation symmetry $\alpha_m \equiv 0$, in which case the Berry curvature is forced to vanish. For simplicity, we have evaluated the Berry curvature for the $\mathscr{C}_s$ point group-symmetric case assuming $\alpha_m \equiv \alpha_{OR}$. In our continuum $SU(3)$ model, the BC can be computed using the method outlined in Ref. [143]. We have subsequently computed the corresponding dipole measuring, as before, energies in units of $k_F^2/2m$, lengths in units of $1/k_F$ and densities in units of $n_0 = k_F^2/2\pi$. The dimensionless orbital Rashba coupling has been varied between $\alpha_{OR} = 1$ and $\alpha_{OR} = 2$ whereas we have fixed $\Delta = -0.1$ and $\Delta_m = 0.005$. The value of the crystal field splitting Δ is consistent with the amplitude determined by x-ray absorption spectrosopy [144] of the order 8 meV, and therefore

almost one order of magnitude smaller than our energy unit $\simeq$ 40meV for a reference $k_F^{-1} \simeq 0.5$ nm and an effective mass $m \simeq 3m_e$ (see Supplementary Note III). The calculated dipole displayed in Fig. 4.5a has been finally multiplied by two to account for spin degeneracy. We remark that, as shown in the Supplementary Information (Supplementary Note I), both the model Hamiltonian for the spin sources of Berry curvature Eq. (6) and the model Hamiltonian for the orbital sources Eq. (8) derive from a single six-band model where orbital and spin degree of freedom are treated on an equal footing.

ESTIMATION OF THE BERRY CURVATURE DIPOLE MAGNITUDE FROM NONLINEAR HALL MEASUREMENTS.

The nonlinear current density is mathematically given by $j_\alpha^{2\omega} = \chi_{\alpha\beta\gamma} E_\beta E_\gamma$, where $\chi_{\alpha\beta\gamma}$ is the nonlinear transverse conductivity tensor. When an a.c. current density $I_x^\omega / W = \sigma_{xx} E_x^\omega$ is sourced along $\hat{\boldsymbol{x}}$, the transverse second harmonic current density developing along $\hat{\boldsymbol{y}}$ is related to the BC dipole $\boldsymbol{D}$ according to [101]:

$$\boldsymbol{j}_y^{2\omega} = \frac{e^3\tau}{2\hbar^2(1+i\omega\tau)} \left(\hat{\boldsymbol{z}} \times \boldsymbol{E}_x^\omega\right)\left(\boldsymbol{D}\cdot \boldsymbol{E}_x^\omega\right), \tag{4.9}$$

where τ is the momentum relaxation time, and e the elementary charge. Due to the mirror symmetry $\mathcal{M}_x \equiv \mathcal{M}_{[\bar{1}10]}$, the dipole is found to point along $\hat{\boldsymbol{x}}$, and in the quasi-d.c. limit, *i.e.* $(\omega\tau) \ll 1$, the BC dipole expression reduces to:

$$D_x = \frac{2\hbar^2}{e^3\tau}\frac{j_y^{2\omega}}{\left(E_x^\omega\right)^2} = \frac{2\hbar^2}{e^3\tau}\frac{V_{yxx}^{2\omega}\sigma_{xx}^3 W}{|I_x^\omega|^2}, \tag{4.10}$$

which is the explicit expression for Eq.4.1, in terms of experimentally measurable quantities only, and where:

$$\chi_{yxx} = \frac{j_y^{2\omega}}{\left(E_x^\omega\right)^2}, \tag{4.11a}$$

$$\chi_{xyy} = \frac{j_x^{2\omega}}{\left(E_y^\omega\right)^2} \tag{4.11b}$$

are the measured nonlinear transverse conductivity tensor elements shown in Fig. 4.5c,e.

4.5. SUPPLEMENTARY NOTE

4.5.1. SUPPLEMENTARY NOTE I: BERRY CURVATURE AT TRIGONAL OXIDE INTERFACES

To derive the electronic properties of the two-dimensional system realized at the [111] $LaAlO_3$ / $SrTiO_3$ interface in the high-temperature trigonal phase, we first discuss the orbital and symmetry character of the electronic levels at the center of the Brillouin zone. Let us first neglect spin-orbit coupling. Due to the trigonal coordination, the three t_{2g} Ti orbitals are split into an a_{1g} orbital representing a real one-dimensional irreducible representation of the $\mathscr{C}_{3v}$ point group, and an e'_g doublet forming a real two-dimensional irreducible representation of the group. The e_g Ti orbitals are not affected by the trigonal crystal field as they also form a doublet. Let us now include the effect of spin-orbit coupling breaking the $SU(2)$ spin rotation symmetry. The two spin-orbit coupled states originating from the a_{1g} orbital have a symmetry-protected degeneracy since they form the Γ_4 two-dimensional irreducible representation of the $\mathscr{C}_{3v}$ double-point group. Spin-orbit coupling instead splits the quartet of states originating from the e'_g doublets. Specifically, two spin-orbit coupled orbitals are singly degenerate and form the Γ_5 and the Γ_6 one-dimensional irreducible representations of the double point group. The remaining two states are instead degenerate and form a Γ_4 representation. Since the Γ_5 and Γ_6 representations are complex, time-reversal symmetry implies that these states must stick together thus forming a Kramers' doublet. The irreducible two-dimensional Γ_4 representation is instead quaternionic and therefore is already equipped with time-reversal invariance. As a result, we have that all levels at the BZ center correspond to an effective spin-$\frac{1}{2}$ Kramers' doublet.

The minimal model Hamiltonian close to each of these Kramers' doublets can be derived in a $\mathbf{k}\cdot\mathbf{p}$ expansion accounting for all symmetry-allowed terms. To do so, we note that in the surface Kramers' doublet basis the time-reversal symmetry can be represented as $\mathscr{T} = i\sigma_y\mathscr{K}$ with $\mathscr{K}$ the complex conjugation. The mirror symmetry is instead represented by $\mathscr{M} = i\sigma_x$. Note that from here onwards $\hat{x}$ will indicate the $[\bar{1}10]$ direction. In the basis $\psi^{\uparrow\downarrow}$ the threefold rotation operator takes the form $\mathscr{C}_3 = e^{-i\sigma_z\pi/3}$. Under the operation of $\mathscr{C}_3$ and $\mathscr{M}$, momentum and spin transform as follows,

$$\begin{array}{llll} \mathscr{C}_3: & k_\pm \to e^{\pm i2\pi/3}k_\pm, & \sigma_\pm \to e^{\pm i2\pi/3}\sigma_\pm, & \sigma_z \to \sigma_z \\ \mathscr{M}: & k_+ \to -k_- & \sigma_x \to \sigma_x, & \sigma_{y,z} \to -\sigma_{y,z} \end{array}$$

where $k_\pm = k_x \pm ik_y$ and $\sigma_\pm = \sigma_x \pm i\sigma_y$. The Hamiltonian must also be invariant under time reversal which adds the constraint $\mathscr{H}(\mathbf{k}) = \mathscr{T}\mathscr{H}(-\mathbf{k})\mathscr{T}^{-1} = \sigma_y\mathscr{H}^*(-\mathbf{k})\sigma_y$.

At linear order in the momentum $\mathbf{k}$, and including an effective regularizing quadratic term, the minimal two-band Hamiltonian for a Kramers' related pair of bands reads:

$$\mathscr{H}_{\mathrm{R}}(\mathbf{k}) = \frac{\mathbf{k}^2}{2m}\sigma_0 - \alpha_{\mathrm{R}}\boldsymbol{\sigma}\cdot\mathbf{k}\times\hat{\mathbf{z}}, \tag{4.12}$$

where $\boldsymbol{\sigma}$ is a vector of Pauli matrices, σ_0 is the identity matrix, α_{R} is the "Rashba" spin-orbit coupling strength, while m is the effective electron mass. Note that nothing prevents the effective electron mass to be negative. In this case, electron-like transport can

be ensured by adding a term quartic in momentum $\mathbf{k}^4/(2m_1)\,\sigma_0$ with $m_1 > 0$. Overall, this amounts to consider a momentum dependent effective electron mass. The Hamiltonian in Eq. (4.12) does not capture crystalline anisotropy effects. In addition, the Berry curvature associated to this minimal model is zero, since there is no term proportional to σ_z. However, higher order momentum terms change this situation. The first symmetry allowed term accounting for crystalline anisotropy is third order in momentum and takes the form,

$$\mathscr{H}_w(\mathbf{k}) = \frac{\lambda}{2}(k_+^3 + k_-^3)\sigma_z\,. \tag{4.13}$$

This warping Hamiltonian is proportional to the Pauli matrix σ_z, which is crucial to obtain a non-zero Berry curvature and leads to out-of-plane spin textures. Note that since the full Hamiltonian is invariant under the mirror symmetry $\mathscr{M}$, $\mathscr{H}_w(\mathbf{k})$ is forced to vanish along the mirror line.

To show the presence of a finite Berry curvature induced by warping, we recall that in a two band model the Berry curvature can be calculated by rewriting the full Hamiltonian as $\mathscr{H}(\mathbf{k}) = \mathbf{d}(\mathbf{k})\cdot\boldsymbol{\sigma} + \mathbf{k}^2\sigma_0/[2m(\mathbf{k})]$, where $\mathbf{d}$ is a momentum dependent vector, which for our specific model has components $\mathbf{d} = \{-k_y, k_x, \lambda\left(k_+^3 + k_-^3\right)/2\}$. The $\mathbf{d}$ vector is independent of terms $\propto \sigma_0$, and thus of the momentum dependent effective electron mass. The expression for the Berry curvature is then given by $\Omega_z^{\pm}(\mathbf{k}) = \pm\hat{\mathbf{d}}\cdot(\partial_{k_x}\hat{\mathbf{d}}\times\partial_{k_y}\hat{\mathbf{d}})/2$ with $\hat{\mathbf{d}} = \mathbf{d}/|\mathbf{d}|$. For our minimal model Hamiltonian in the presence of trigonal symmetry, we have

$$\Omega_{\pm}^z(k,\theta) = \pm\frac{2\sqrt{2}\lambda\alpha_{\mathrm{R}}^2 k^3\cos(3\theta)}{\left[2\alpha_{\mathrm{R}}^2 k^2 + \lambda^2 k^6\cos(6\theta) + \lambda^2 k^6\right]^{3/2}}\,, \tag{4.14}$$

where θ is the polar angle in momentum space.

The Berry curvature is well defined in each point except the origin where the bands are degenerate. Note that the constraints set by time reversal symmetry and the threefold rotational symmetry are satisfied as can be verified upon a closer inspection of Eq. (4.14). Moreover $\Omega_{\pm}^z(k,\theta)$ vanishes along the mirror lines, in accordance with Eq. (4.13).

The orbital sources of Berry curvature can be instead derived by explicitly considering interorbital mixing terms. To this end, it is convenient to neglect spin-orbit coupling. The effective Hamiltonian for the a_{1g} and e_g' doublet in the trigonal crystal field can be derived using symmetry principles. Specifically, any generic 3×3 Hamiltonian can be expanded in terms of the nine Gell-Mann matrices Λ_i as

$$\mathscr{H}(\mathbf{k}) = \sum_{i=0}^{8} b_i(\mathbf{k})\Lambda_i\,. \tag{4.15}$$

The invariance of the Hamiltonian requires that the components of the Hamiltonian vector $\mathbf{b}(\mathbf{k})$ should have the same behavior as the corresponding Gell-Mann matrices Λ_i. This means that they should belong to the same representation of the crystal point group. The representation of the Gell-Mann matrices Λ_i and those of the polynomials of $\mathbf{k}$ can be found using that the generators of the point group for spinless electrons can be

written as

$$\mathscr{M}_x = \begin{pmatrix} 1 & 0 & 0 \\ 0 & 1 & 0 \\ 0 & 0 & -1 \end{pmatrix}; \quad \mathscr{C}_3 = \begin{pmatrix} 1 & 0 & 0 \\ 0 & \cos\frac{2\pi}{3} & \sin\frac{2\pi}{3} \\ 0 & -\sin\frac{2\pi}{3} & \cos\frac{2\pi}{3} \end{pmatrix}.$$

With this, the effective Hamiltonian up to linear order in momentum reads

$$\mathscr{H}(\mathbf{k}) = \frac{\mathbf{k}^2}{2m}\Lambda_0 + \Delta\left(\Lambda_3 + \frac{1}{\sqrt{3}}\Lambda_8\right) - \alpha_{\mathrm{OR}}\left[k_x\Lambda_5 + k_y\Lambda_2\right], \tag{4.16}$$

where Λ_0 is the identity matrix and the other Gell-Mann matrices are reported in the main text. The last term in the equation above corresponds to the orbital Rashba coupling with strength α_{OR}. The second term gives the crystal field splitting of size Δ between the a_{1g} singlet and the e'_g doublet. As discussed in the main text, a direct computation of the Berry curvature using the method outlined in Ref. [143] yields a vanishing Berry curvature at all momenta. This changes by considering a crystalline symmetry lowering to $\mathscr{C}_s$. From the representation of Gell-Mann matrices and polynomials of momentum, the effective Hamiltonian now takes the form

$$\mathscr{H}_{\mathrm{OR}}(\mathbf{k}) = \frac{\mathbf{k}^2}{2m}\Lambda_0 + \Delta\left(\Lambda_3 + \frac{1}{\sqrt{3}}\Lambda_8\right) + \Delta_m\left(\frac{1}{2}\Lambda_3 - \frac{\sqrt{3}}{2}\Lambda_8\right) - \alpha_{\mathrm{OR}}\left[k_x\Lambda_5 + k_y\Lambda_2\right] - \alpha_m k_x\Lambda_7\,.$$

In the equation above, the crystal field splitting Δ_m yields an energy separation between the e'_g states at the center of the BZ. This Hamiltonian is characterized by Berry curvature distributions with dipolar hot spots and singular pinch points. Furthermore, it is naturally equipped with a large non-vanishing Berry curvature dipole. The dispersion of the bands is strongly dependent on the ratio between the characteristic orbital Rashba energy $E_{\mathrm{OR}} = 2m\alpha_{\mathrm{OR}}^2$ and the crystal field splittings. In particular, the effective mass of the lowest band is negative close to the Γ point of the BZ whenever the orbital Rashba energy is comparable to the crystal-field splitting Δ. In this regime, an intraband Lifshitz transition occurs when increasing the chemical potential. On the contrary, in the opposite regime of large crystal field splittings, all bands possess an effective electron mass that is positive at all momenta, and consequently intraband Lifshitz transitions do not take place. This is explicitly shown in Fig. 4.12 where we report the evolution of the bands by continuously increasing the Δ/E_{OR} ratio. Note that similar features are also found within the remaining doublet of bands. In this case the momentum dependence of the effective mass is controlled by the ratio between the crystal field splitting Δ_m and the effective orbital Rashba energy $E_{\mathrm{OR}} = 2m\alpha_m^2$, and can acquire a non-trivial dependence along the $k_y = 0$ line.

In Fig. 4.12, we also indicate the relevant range of energies in the band structure, which we evaluate using the following argument. To obtain a Berry curvature dipole of order k_F, the orbital Rashba parameter has to be comparable to $k_F/(2m)$. This is explicitly shown in Fig. 4.4a of our main manuscript – the Berry curvature dipole has a sweet spot and can exceed $1/k_F$ when $2m\alpha_{OR} \simeq k_F$. Hence, the orbital Rashba momentum $k_{OR} \simeq k_F$. Considering the finite range of the Berry curvature dipole sweet spot and the additional tuning of the carrier density by gating (see Supplementary Note III), we estimate that the Fermi wavevector $k_{OR} < k_F < 1.5k_{OR}$. This consequently gives an upper

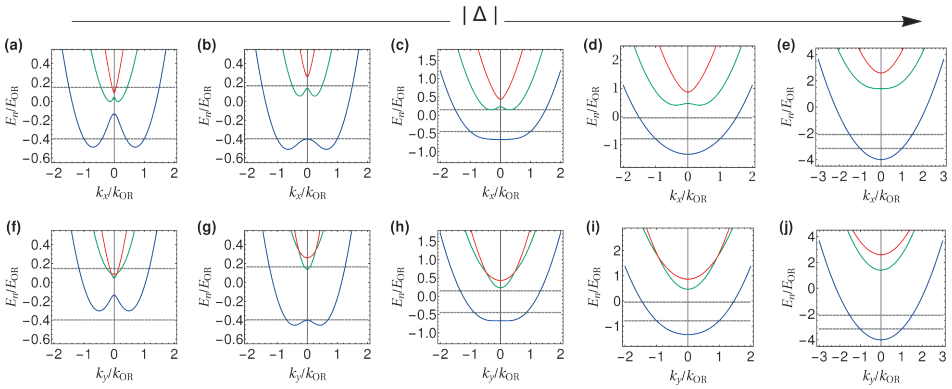

Figure 4.12: **Dependence of the orbital-sourced model on crystal field splittings.** Evolution of the energy bands on the $k_y = 0$ line (top panels) and the $k_x = 0$ line (bottom panels) for the spin-orbit-free orbital-sourced model by increasing the ratio between the crystal field splitting Δ and the characteristic orbital Rashba energy $E_{OR} = 2m\alpha_{OR}^2$. The panels correspond to a) $\Delta/E_{OR} = -0.1$, (b) $\Delta/E_{OR} = -0.3$, (c) $\Delta/E_{OR} = -0.5$, (d) $\Delta/E_{OR} = -1.0$, and (e) $\Delta/E_{OR} = -3.0$. Same values are used for the sequence (f)-(j). The crystal field splitting $\Delta_m = 0.2|\Delta|$ and we have chosen the orbital Rashba parameter $\alpha_m = \alpha_{OR}$. All energies are measured in units of E_{OR} whereas momenta are measured in units of the orbital Rashba momentum $k_{OR} = 2m\alpha_{OR}$. The gray lines are upper and lower bounds for the Fermi energy.

and lower bounds for the Fermi energy shown as gray lines in Fig. 4.12. We note that the possibility of occupying more than one band is in line with the observations presented in Ref. [122]. Finally we wish to point out that since the orbital Rashba energy corresponds to the characteristic kinetic energy $k_F^2/(2m)$, which lies in the tens of meV range, all values of the crystal field splitting Δ considered in Fig. 4.12 could be realized in practice – x-ray absorption spectroscopy [144] indicates a crystal field splitting of the order 8 meV. In other words, the material could be on the verge of a change in the sign of the effective mass close to zero momentum.

We next show that both the Hamiltonian characterizing the orbital degrees of freedom and the Hamiltonian in Eq. (4.12) for the spin degree of freedom can be derived from a single model that treats orbital and spin degrees of freedom on an equal footing. In order to make a link between the spin and orbital degrees of freedom one needs to include the atomic spin-orbit coupling.

Then, the starting point for the coupled spin and orbital degrees of freedom is provided by the following model Hamiltonian:

$$\mathscr{H}_{tot}(\mathbf{k}) \quad = \quad \mathscr{H}_{OR}(\mathbf{k}) \otimes \sigma_0 + \lambda_{so}(L_x \otimes \sigma_x + L_y \otimes \sigma_y + L_z \otimes \sigma_z), \tag{4.17}$$

where we have included the atomic spin-orbit coupling with the strength λ_{so} and σ_i indicate the spin Pauli matrices with $i = x, y, z$. We recall that the orbital angular momentum projected on the effective subspace with the three selected orbital configurations has the following representation in terms of the Gell-Mann matrices: $L_x = \Lambda_2$, $L_y = \Lambda_5$, and $L_z = \Lambda_7$.

For simplicity, we next consider a $\mathscr{C}_{3v}$ symmetric (i.e. $\Delta_m = \alpha_m = 0$) crystalline environment. At the Γ point of the BZ, and explicitly including atomic spin-orbit coupling,

the Hamiltonian reduces to:

$$\mathscr{H}^{\Gamma}_{tot} = \mathscr{H}^{\Gamma}_{\mathrm{OR}} \otimes \sigma_0 + \lambda_{\mathrm{so}}(L_x \otimes \sigma_x + L_y \otimes \sigma_y + L_z \otimes \sigma_z), \tag{4.18}$$

with

$$\mathscr{H}^{\Gamma}_{\mathrm{OR}} = \Delta\left(\Lambda_3 + \frac{1}{\sqrt{3}}\Lambda_8\right). \tag{4.19}$$

$\mathscr{H}^{\Gamma}_{tot}$ can be diagonalized and yields the following double degenerate (Kramer pairs) eigenvalues $E_A = \tilde{E_A} + \frac{4}{3}\Delta, E_B = \tilde{E_B} + \frac{4}{3}\Delta$, $E_C = \tilde{E_C} + \frac{4}{3}\Delta$ with:

$$\tilde{E}_C = \frac{1}{2}\left(-2\Delta - \lambda_{\mathrm{so}} + \sqrt{4\Delta^2 + 4\Delta\lambda_{\mathrm{so}} + 9\lambda^2_{\mathrm{so}}}\right) \tag{4.20}$$

$$\tilde{E}_B = -2\Delta + \lambda_{\mathrm{so}} \tag{4.21}$$

$$\tilde{E}_A = \frac{1}{2}\left(-2\Delta - \lambda_{\mathrm{so}} - \sqrt{4\Delta^2 + 4\Delta\lambda_{\mathrm{so}} + 9\lambda^2_{\mathrm{so}}}\right). \tag{4.22}$$

According to the character of the trigonal splitting and the Hund's rule (spin-orbit coupling favors the highest total angular momentum at low filling) λ_{so} and Δ have negative values. Thus, the following energy relation holds $E_A < E_B < E_C$. E_A is the lowest energy in the multiplet.

The eigenvectors can be also written in a compact vectorial form as:

$$|v_{C,1}\rangle = \frac{1}{\sqrt{2+c^2}}[-c,0,0,-i,0,1] \tag{4.23}$$

$$|v_{C,2}\rangle = \frac{1}{\sqrt{2+c^2}}[0,c,i,0,1,0] \tag{4.24}$$

$$|v_{B,1}\rangle = \frac{1}{\sqrt{2}}[0,0,0,i,0,1] \tag{4.25}$$

$$|v_{B,2}\rangle = \frac{1}{\sqrt{2}}[0,0,-i,0,1,0] \tag{4.26}$$

$$|v_{A,1}\rangle = \frac{1}{\sqrt{2+a^2}}[-a,0,0,-i,0,1] \tag{4.27}$$

$$|v_{A,2}\rangle = \frac{1}{\sqrt{2+a^2}}[0,a,i,0,1,0], \tag{4.28}$$

with

$$a = -\frac{\tilde{E}_C}{\lambda_{\mathrm{so}}} \tag{4.29}$$

$$c = -\frac{\tilde{E}_A}{\lambda_{\mathrm{so}}}. \tag{4.30}$$

In the new spin-orbit coupled basis the Hamiltonian $\mathscr{H}_{tot}$ has the following matrix form:

$$\mathscr{H}_{tot} = \begin{pmatrix} H_{CC} & H_{CB} & H_{CA} \\ H_{CB}^{\dagger} & H_{BB} & H_{BA} \\ H_{CA}^{\dagger} & H_{BA}^{\dagger} & H_{AA} \end{pmatrix} \tag{4.31}$$

with H_{MN} being 2x2 matrices.

Let us now focus on the matrix elements of the block Hamiltonian H_{AA} associated with the lowest energy doublet assuming that the energy splitting among the levels is larger than the strength occurring in the inter-doublet terms (i.e. H_{CB},H_{BA}, H_{CA}). We emphasize that since the energy splitting between the spin-orbit Kramers' doublets is controlled (at fixed values of the crystal fields) by the spin-orbit coupling strength, the intradoublet hybridization channels H_{BA}, H_{CA}, H_{CB} can be safely neglected in the large spin-orbit coupling regime $\lambda_{\rm so} \gg E_{\rm OR}$. In this case, one can directly determine the effective spin Hamiltonian by evaluating the following expectation values:

$$H_{AA}(i,j) = \langle v_{A,i}|\mathscr{H}_{tot}|v_{A,j}\rangle. \tag{4.32}$$

Taking into account the expressions of the eigenvectors $v_{A,i}$ and of the k-dependent terms of the total Hamiltonian, the matrix of the block H_{AA} can be written as:

$$H_{AA} = E_A + \frac{\mathbf{k}^2}{2m} + \begin{pmatrix} \frac{\lambda}{2}(k_+^3 + k_-^3) & -\alpha_{\rm R}\left(ik_x - ky\right) \\ -\alpha_{\rm R}\left(-ik_x - ky\right) & -\frac{\lambda}{2}(k_+^3 + k_-^3) \end{pmatrix} \tag{4.33}$$

with the effective intra-doublet Rashba interaction given by

$$\alpha_{\rm R} = \frac{2\alpha_{\rm OR}\lambda_{\rm so}}{\sqrt{4\Delta^2 + 4\Delta\lambda_{\rm so} + 9\lambda_{\rm so}^2}}. \tag{4.34}$$

Note that in the Hamiltonian above the trigonal warping in the spin sector is found by equipping the orbital model Hamiltonian with a symmetry-allowed cubic term $\propto \gamma(k_+^3 + k_-^3)\Lambda_7$. Then the warping coupling λ has the following expression

$$\lambda = \gamma \frac{16\lambda_{\rm so}^2}{8\lambda_{\rm so}^2 + \tilde{E}_A^2}. \tag{4.35}$$

Therefore, the effective low-energy spin model can be directly linked to the orbital model with its sources of Berry curvature dipole. Two remarks are in order here. First, using a Löwdin procedure one can verify that there exist higher-order corrections, *e.g.* momentum dependent renormalization of the Rashba coupling $\alpha_{\rm R} \to \alpha_{\rm R}(1 + \delta\mathbf{k}^2)$. Second, the bare effective electron mass appearing in Eq. (4.33) is corrected by intraorbital mixing terms due to the finiteness of the spin-orbit coupling strength. This generally results in a momentum dependent mass that can be negative close to zero momentum in agreement with the features of the spin-orbit free orbital bands discussed above. This is explicitly proven in Fig.4.13 where we show the evolution of the spin-orbit coupled bands

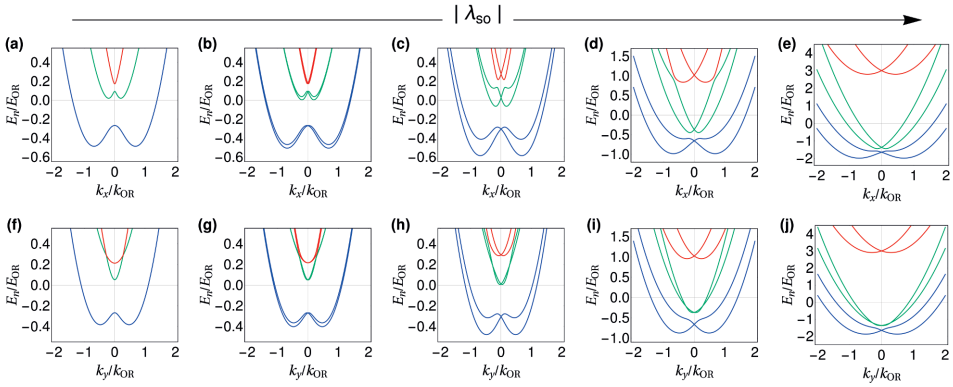

Figure 4.13: **Dependence of the energy bands on spin-orbit coupling.** Evolution of the energy bands on the $k_y = 0$ line (top panels) and the $k_x = 0$ line (bottom panels) for the full model Eq. (4.17) by increasing the ratio between the spin-orbit coupling strength λ_{so} and the characteristic orbital Rashba energy $E_{OR} = 2m\alpha_{OR}^2$. The panels correspond to (a) $\lambda_{so} = 0$, (b) $\lambda_{so}/E_{OR} = -0.02$, (c) $\lambda_{so}/E_{OR} = -0.1$, (d) $\lambda_{so}/E_{OR} = -0.5$, and (e) $\lambda_{so}/E_{OR} = -1.5$. Same values are used for the sequence (f)-(j). The crystal field splittings have been chosen as $\Delta = -0.2E_{OR}$ and $\Delta_m = 0.2|\Delta|$. Finally the orbital Rashba parameter $\alpha_m = \alpha_{OR}$. All energies are measured in units of E_{OR} whereas momenta are measured in units of the orbital Rashba momentum $k_{OR} = 2m\alpha_{OR}$.

by increasing λ_{so}. Spin-orbit coupling generally weakens the momentum dependence of the effective mass eventually leading to a positive effective mass at all momenta. Importantly, and as mentioned above, the symmetry-based spin model can be applied without restrictions even in the presence of a strongly momentum dependent mass. Therefore, the spin sources of Berry curvature are correctly captured even for intermediate spin-orbit coupling strenghts.

In this case, the spin-sourced model can be applied up to momenta for which the corresponding energy of the spin bands is comparable to the splitting ΔE_Γ between two different Kramers doublets at the center of the BZ. This gives an upper bound for the Fermi wavevector $k_F = \sqrt{k_R^2/4 + m\Delta E_\Gamma} - k_R/2$ with $k_R = 2m\alpha_R$.

Our experimental observations indicate the occurrence of a strong anomalous planar Hall effect at the same carrier densities at which a sizable non-linear Hall effect at zero magnetic field is measured. The characteristic features of the anomalous planar Hall effect can be explained using the spin-sourced model – the orbital-sourced Berry curvature is stiff in response to externally applied in-plane magnetic fields. Instead, the non-linear Hall effect at zero magnetic field cannot be quantitatively captured within this picture, and the orbital sources of Berry curvature are needed. Putting these observations together, we can therefore conclude that both orbital Rashba and spin-orbit coupling are relevant ingredients to describe the physical properties of the material structure. Our experimental tools independently probe the Berry curvature associated with orbital and spin degrees of freedom.

4.5.2. SUPPLEMENTARY NOTE II: MAGNETOTRANSPORT THEORY

ANOMALOUS PLANAR HALL EFFECT

In this section we discuss the Hall effect induced by the spin-sourced Berry curvature in the presence of a planar magnetic field using a semiclassical Boltzmann framework.

We first note that the presence of a planar magnetic field generates a Zeeman coupling term in the low-energy Hamiltonian $\mathscr{H}_B = B(\sigma_x \cos\phi + \sigma_y \sin\phi)$, that breaks $\mathscr{C}_3$ when present, $\mathscr{T}$ and the remaining mirror $\mathscr{M}_x$ except when the direction of the magnetic field with respect to the $\hat{x}$ axis $\phi = 2\pi m/6$ with $m \in \mathbb{N}$. In this case one mirror symmetry is preserved. The energy dispersion of the total Hamiltonian is then given by:

$$\begin{aligned}\varepsilon_{\pm}(\mathbf{k}) &= \frac{\mathbf{k}^2}{2m} + \Big[(B\sin(\phi) + k_x\alpha_R)^2 + (k_y\alpha_R - B\cos(\phi))^2 \\ &\quad + \lambda^2\left(k_x^3 - 3k_xk_y^2\right)^2\Big]^{1/2}. \end{aligned} \tag{4.36}$$

The planar magnetic field breaks the Kramer's degeneracy at the center of the BZ and completely splits the two bands. However, when a mirror is preserved there is a mirror-symmetry protected Dirac point along the mirror line at $(k,\theta) = (|B|/\alpha_R, \phi + sgn(B)\pi/2)$. The condition $k_F = |B|/\alpha_R$ defines the critical magnetic field strength introduced in the main text. Moreover, a Lifshitz transition (a change in topology in the Fermi surface, in this case going from one closed Fermi line to two) appears since the Zeeman coupling shifts the minima of the two bands. The energy for which the upper band is completely depleted is given by $\varepsilon_L = B^2/(2m\alpha_R^2)$ if $B < m\alpha_R^2$ otherwise $\varepsilon_L = B - m\alpha_R^2/2$ if $B > m\alpha_R^2$.

To derive the transport characteristic associated to this low-energy model we assume to apply an electric field $\mathbf{E} = E\hat{\mathbf{x}}$ along the $\hat{x}$ axis and rotate the magnetic field in the $x-y$ plane. Thus we write the magnetic field as $\mathbf{B} = B(\cos\phi\hat{\mathbf{x}} + \sin\phi\hat{\mathbf{y}})$. Generally speaking, the semiclassical equations of motions in the presence of a non-zero Berry curvature read

$$\dot{\mathbf{r}} = D(\mathbf{B},\Omega_k)[\mathbf{v_k} + e(\mathbf{E}\times\Omega_k) + e(\mathbf{v_k}\cdot\Omega_k)\mathbf{B}] \tag{4.37}$$

$$\dot{\mathbf{k}} = D(\mathbf{B},\Omega_k)[e\mathbf{E} + e(\mathbf{v_k}\times\mathbf{B}) + e^2(\mathbf{E}\cdot\mathbf{B})\Omega_k], \tag{4.38}$$

where $D(\mathbf{B},\Omega_k) = [1 + (e)(\mathbf{B}\cdot\Omega_k)]^{-1}$, Ω_k is the Berry curvature and $\mathbf{v_k}$ is the group velocity. Solving the Boltzmann equation for the electron distribution function $f(k)$ within the relaxation time approximation allows to compute the charge current $\mathbf{J} = e\int(d^dk/(2\pi)^d)\dot{\mathbf{r}}f(k)D^{-1}$ that accounts for the modified phase space factor D. In linear response theory the charge current obeys the relation $J_a = \sigma_{ab}E_b$, where σ_{ab} are the components of the conductivity tensor and E_b the external electric field. Following Ref. [99], the planar Hall conductivity, after discarding higher order contributions, is given by

$$\begin{aligned}\sigma_{yx} &= e^2\int\frac{d^dk}{(2\pi)^d}D\tau(-\frac{\partial f_{eq}}{\partial\epsilon})\{[v_y + eB\sin\theta(\mathbf{v_k}\cdot\Omega_k)] \\ &\quad [v_x + eB\cos\theta(\mathbf{v_k}\cdot\Omega_k]\} + \frac{e^2}{h}\int\frac{d^2k}{(2\pi^2)}\Omega_k^z f_{eq}, \end{aligned} \tag{4.39}$$

where f_{eq} is the equilibrium Fermi-Dirac distribution. Eq. (4.39) contains all transverse linear responses in the presence of coplanar electric and magnetic fields in both two-

and three-dimensional systems. In three-dimensional topological Dirac and type-I Weyl semimetals, the Berry-curvature induced planar Hall effect stems from the term proportional to $\propto B^2 \sin\theta\cos\theta(\mathbf{v_k}\cdot\Omega_k)^2$. The last term instead represents the usual anomalous Hall contribution for magnetic materials. In two-dimensional systems, $\mathbf{v_k} \perp \Omega_k$. However, in trigonal crystals a non-vanishing contribution to the last term of Eq. (4.39) appears once the Zeeman interaction is explicitly taken into account, and exists provided all mirror symmetries are broken, even though the material is non-magnetic. This also implies that, contrary to three-dimensional topological semimetals, the Berry-curvature related planar Hall effect of two-dimensional systems does not explicitly depend on the relative angle between the electric and magnetic field but only on the angle between the planar magnetic field and the principal crystallographic directions. This, in turns, allows to directly observe a purely antisymmetric planar Hall effect when the electric and magnetic fields are perfectly aligned since in this configuration the classical contribution of Eq. (4.39), containing the $v_x v_y$ term vanishes.

We have computed the behavior of the anomalous planar Hall conductivity assuming a magnetic field direction $\phi = \pi/2$. In this configuration all mirror symmetries are broken. Moreover the integral of the Berry curvature is maximum. The contribution to the linear transverse response σ_{xy} is given by the integral of the Berry curvature over the Fermi surfaces of the two energy bands. Since the two bands contribute with opposite curvatures it is sufficient to integrate over the exclusion region of the two bands. Hence the anomalous contribution to the transverse conductivity, at zero temperature is given by

$$\sigma_{xy} \propto \int_{\mathscr{S}_+} \Omega_z^+(\mathbf{k}) + \int_{\mathscr{S}_-} \Omega_z^-(\mathbf{k}) = \int_{\mathscr{S}_+ \cap \mathscr{S}_-} \Omega_z^-(\mathbf{k}) \,, \tag{4.40}$$

where $\mathscr{S}_\pm$ are the Fermi surfaces of the two bands and the last integral contains Ω^- since it is the curvature of the outermost band. The magnetic field dependence at constant density can be calculated numerically by varying the Fermi energy as the magnetic field is changed. Indeed, by keeping the area of the surface $\mathscr{S}_+ \cap \mathscr{S}_-$ fixed the number of electronic carriers stays constant. To obtain the resistivity ρ_{xy} it is necessary to compute the two longitudinal conductivities σ_{xx} and σ_{yy}. In the relaxation time approximation these are given by,

$$\sigma_{\alpha\alpha} = e^2\tau \sum_{\gamma=\pm} \int_{\mathbf{k}} (\partial_\alpha \varepsilon_\gamma)^2 (-\frac{\partial f_0}{\partial \varepsilon_\gamma}) \,, \tag{4.41}$$

where $\alpha = (x, y)$, ε_γ is the energy dispersion of the band γ and f_0 is the equilibrium Fermi-Dirac distribution. The resistivity ρ_{xy} is then obtained by inverting the conductivity tensor,

$$\rho_{xy} = \frac{\sigma_{xy}}{\sigma_{xx}\sigma_{yy} + \sigma_{xy}^2} \,. \tag{4.42}$$

Here we have used that the transverse conductivity is purely antisymmetric, *i.e.* $\sigma_{xy}(B) = -\sigma_{yx}(B)$, since the semiclassical contributions are vanishing.

Fig. 4.14 shows the corresponding behavior of the anomalous planar Hall resistivity as a function of the magnetic field strength for different values of the carrier density.

The plot has been obtained by writing the low-energy Hamiltonian in dimensionless form measuring energies units of $k_F^2/2m$, lengths in units of $1/k_F$ and density in units of $n_0 = k_F^2/2\pi$. The remaining dimensionless parameters have been fixed to $\alpha_R = 0.4$, and $\lambda = 0.1$ Furthermore, we have used the approximate expression for the transverse resistivity $\rho_{xy} \simeq \sigma_{xy}/(\sigma_{xx}\sigma_{yy})$, which is accurate since the transverse conductivity is much smaller than the linear in τ longitudinal resistivity. We obtain that the anomalous planar Hall resistivity increases non-monotonically and gets enhanced by decreasing the carrier density. Note that when considering the observed decrease of the carrier density as the sheet conductivity increases (see Supplementary Note VI), this trend is in agreement with the behavior of the antisymmetric Hall resistance reported in the main text.

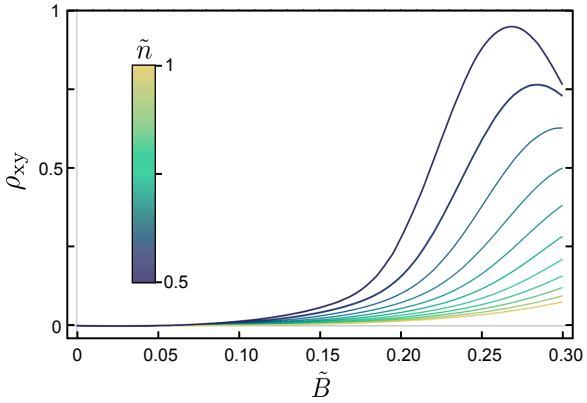

Figure 4.14: **Calculated planar Hall resistivity versus band filling.** Calculated magnetic field dependence of the anomalous planar Hall resistivity (measured in arbitrary units) ρ_{xy}, for different carrier densities. The magnetic field $\tilde{B}$ is normalized in units of $k_F^2/2m$ and the densities $\tilde{n}$ are in units of $k_F^2/2\pi$. The anomalous planar Hall contribution is maximum for values of the magnetic field that shift the anti-crossing point close to the Fermi energy, and goes back to zero for stronger magnetic fields.

NONLINEAR TRANSVERSE RESPONSE WITH PLANAR MAGNETIC FIELDS

Nonlinear transverse currents have two intrinsic contributions: the first is a semiclassical term that depends on the integral of the electronic velocities, whereas the other has a purely quantum nature stemming from the Berry curvature dipole:

$$\sigma^{sc}_{\alpha\alpha\beta} \propto \int_k \partial^2_\alpha f_0 \partial_\beta \varepsilon_k \tag{4.43}$$

$$\sigma^{dip}_{\alpha\alpha\beta} \propto \epsilon_{\alpha\beta} \int_k (\partial_\beta \Omega) f_0 \,, \tag{4.44}$$

where $\epsilon_{\alpha\beta}$ is the Levi-Civita antisymmetric tensor, $\partial_\alpha = \partial_{k_\alpha}$, f_0 is the equilibrium Fermi Dirac distribution and ε_k is the energy dispersion. The two conductivities are the proportionality factors between the applied AC electric field $(E^\omega_\alpha)^2$ and the second harmonic response $j^{2\omega}_\beta$. Typically the full response is measured, and it is necessary to decouple the two contributions in order to extract the magnitude of the Berry curvature dipole. This

can be done by considering how the two conductivities behave when switching the sign of the magnetic field. The $\sigma^{\mathrm{sc}}_{\alpha\alpha\beta}$ is odd in B: this can be seen by sending $B \to -B$ and applying the coordinate change $\mathbf{k} \to -\mathbf{k}$. While the integration measure $\partial k_x \partial k_y$ and the f_0 remain unchanged $[\varepsilon(\mathbf{k}, B) = \varepsilon(-\mathbf{k}, -B)]$ the three derivatives bring an overall minus sign. On the other hand the contribution $\sigma^{\mathrm{dip}}_{\alpha\alpha\beta}$ is even with respect to the sign of the magnetic field. Sending $B \to -B$ and $\mathbf{k} \to -\mathbf{k}$ produces a sign change in the Berry curvature $[\Omega(\mathbf{k}, B) = -\Omega(-\mathbf{k}, -B)]$ which is compensated by the minus sign originating from the coordinate change in the partial derivative.

SYMMETRY CONSTRAINTS ON THE LINEAR AND NONLINEAR RESISTIVITY TENSOR

We recall that the linear conductivity tensor is defined by the relation

$$j_\alpha = \sigma_{\alpha\beta} E_\beta \,. \tag{4.45}$$

We can derive the transformation rule of the conductivity tensor under a generic point group symmetry represented by an orthogonal matrix $\mathcal{O}$ by simply noticing that both the current j and the driving electric field E transform as vectors under a generic coordinate change. Therefore, the conductivity tensor transforms as $\mathcal{O}^T \sigma \mathcal{O}$. For the point group $\mathscr{C}_s$ the single mirror symmetry $\mathscr{M}_x$ implies that the transverse conductivity $\sigma_{xy} \equiv \sigma_{yx} \equiv 0$. In crystals with $\mathscr{C}_{3v}$ point group symmetry instead, the additional threefold rotation symmetry implies that the two longitudinal conductivities along the principal crystallographic directions $\sigma_{xx} \equiv \sigma_{yy}$. Crystalline symmetries also pose constraints on the nonlinear conductivity tensor defined by

$$j_\alpha = \chi_{\alpha\beta\gamma} \, E_\beta \, E_\gamma \,. \tag{4.46}$$

The transformation rule of the nonlinear conductivity tensor imply that in the presence of a $\mathscr{M}_x$ mirror symmetry, we have $\chi_{xxx} = \chi_{xyy} = \chi_{yxy} = \chi_{yyx} = 0$. The additional threefold rotation symmetry in the $\mathscr{C}_{3v}$ point group symmetry implies that the non-zero component of the nonlinear conductivity tensor satisfy the relation $\chi_{xxy} = \chi_{xyx} = \chi_{yxx} = -\chi_{yyy}$. A violation of this relation implies that the trigonal symmetry is broken and only a mirror symmetry is present in the system.

PLANAR MAGNETORESISTANCE COMPUTATION

We have computed the planar magnetoresistance MR $= \left[\rho_{xx,yy}(B)/\rho_{xx,yy}(0) - 1\right]$ considering a planar magnetic field directed along the $[\bar{1}10]$ direction, thus preserving the mirror symmetry. In this case, the transverse Berry-mediated conductance σ_{xy} vanishes. The magnetoresistance is strongly anisotropic and indeed a qualitative difference exists depending on whether the driving current is collinear or orthogonal to the magnetic field. Specifically in the former case (see Fig.4.15 a small positive magnetoresistance starts to develop when the Fermi energy crosses the mirror symmetry-protected Dirac point (orange line). This positive magnetoresistance persists up to the Lifshitz point (red line). After the Lifshitz transition, the magnetoresistance starts decreasing and reaches a negative saturation value as also seen in experiments (see Fig. 4.16). The negative magnetoresistance can be intuitively understood by considering that after the Lifshitz transition scattering between the two energy bands is suppressed, hence enhancing the

magnetoconductance. In the configuration in which the driving electric field and the magnetic field are orthogonal, the magnetoresistance is always negative and the weak-field positive magnetoresistance does not occur [see Fig. 4.13 (a)]. This is in agreement with the features observed at the $LaVO_3$-$KTaO_3$ interface [145]. Note that for configurations in which the magnetic field is not mirror-preserving, a similar type of behaviour is still expected since the quantum contribution is a lower order correction to the semi-classical one.

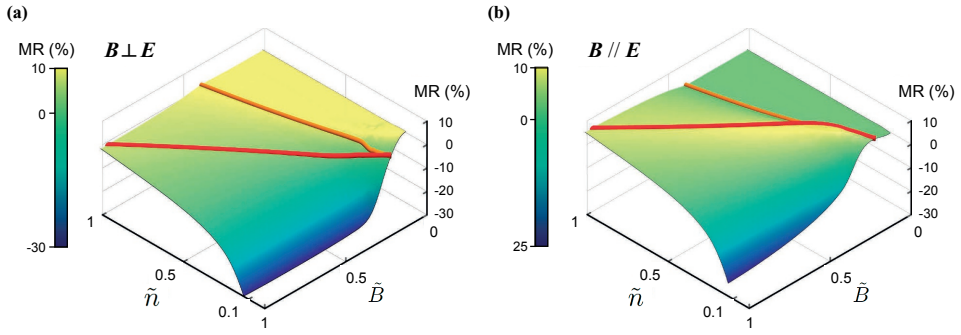

Figure 4.15: **Calculated planar magnetoresistance.** Planar magnetoresistance as obtained by considering a planar magnetic field in the $[\bar{1}10]$ direction and an orthogonal **(a)**, or collinear **(b)** driving electric field. Since the magnetic field is mirror-symmetry preserving $\rho_{xx,yy} = 1/\sigma_{xx,yy}$. The magnetoresistance has been obtained using the same parameter set as in Fig. S1, and is shown also as a function of the carrier density. The magnetic field $\tilde{B}$ is normalized in units of $k_F^2/2m$ and the densities $\tilde{n}$ are in units of $k_F^2/2\pi$.

4.5.3. SUPPLEMENTARY NOTE III: ADDITIONAL MAGNETOTRANSPORT MEASUREMENTS

ORDINARY HALL EFFECT & ESTIMATION OF THE MOMENTUM RELAXATION TIME – GATE DEPENDENCE

Figure 4.17 (a,b) display the gate-modulated ordinary Hall effect, and longitudinal MR (respectively) acquired in the same device, oriented along $[\bar{1}10]$, presented throughout the manuscript; with $B_\perp$ the out-of-plane magnetic field. At low doping levels, the two-dimensional electron system (2DES) exhibits a linear Hall effect, while the low-field MR is indicative of a weak-antilocalization regime, as reported previously [120, 122]. At sheet conductance values σ_{xx} exceeding $\approx$ 2 mS, $\rho_{xy}(B_\perp)$ is found to depart from a purely linear Hall effect. Non-linearities in the ordinary Hall effect response have been discussed extensively in the framework of a multi-carrier conduction, or multi-orbital conduction when considering $SrTiO_3$-based 2DES [146, 147, 122]. Here, in the case of the $[111]-LaAlO_3/SrTiO_3$ 2DES, the nonlinear Hall component has been attributed to the populating of replica sub-bands of the t_{2g}-manifold (derived from the Ti-3d bands) in the quantum well [122, 148].

A number of authors have further discussed the relevance of the two-band model for the determination of meaningful transport parameters values, *i.e.*, carrier densities and mobilities [147, 146, 122]. We simply point out, that in the limit of large magnetic fields,

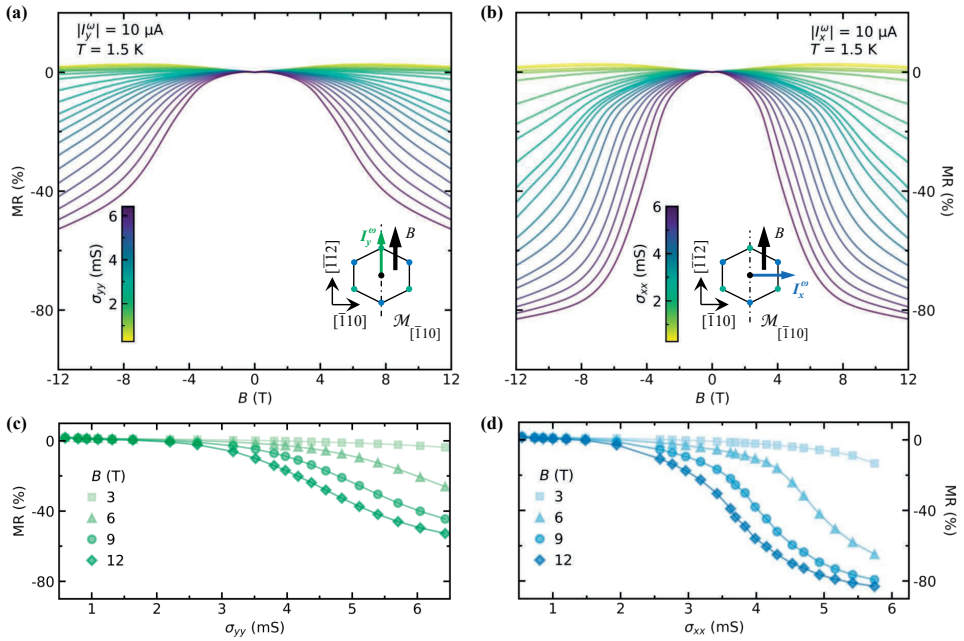

Figure 4.16: **Measured gate-dependent planar magnetoresistance.** Gate modulated magnetoresistance in an in-plane magnetic field for I_y^ω along [$\bar{1}\bar{1}$2] parallel to B **(a)**, and for I_x^ω along [$\bar{1}$10] transverse to B **(b)**. In both cases, the MR is seen to grow negatively above a critical planar magnetic field value. Panels **(c)** and **(d)** display the corresponding sheet conductance dependences of the MR at constant magnetic field values. For both Hall bar devices, the MR shows an onset above a given value of sheet conductance followed by a monotonic increase, and even an apparent saturation for the curve corresponding to $B = 12$ T.

the total carrier density in the system, which we denote n_{2D}, can be related to the slope of ρ_{xy} vs. $B_\perp$ via:

$$n_{2D} = \frac{-1}{e\,R_H}. \tag{4.47}$$

where $R_H = \partial\rho_{xy}(B_\perp)/\partial B_\perp$ is the (here, high-field) Hall coefficient, whose negative sign is consistent with electron-like transport. Making use of the Drude's formula, it follows for μ_H, the electronic mobility:

$$\mu_H = \frac{\sigma_s}{e\,n_{2D}}, \tag{4.48}$$

where $\sigma_s = \sigma_{xx}$ is the sheet conductance of the considered Hall bar device (along [$\bar{1}$10]). Figure 4.17(c) displays both the estimated areal carrier density and electron mobility of the [111]−$LaAlO_3/SrTiO_3$ 2DES across the whole accessible doping range $0.5 \leq \sigma_{xx} \leq 6$ mS. While the mobility is found to increase monotonically, the apparent decrease of n_{2D} versus σ_{xx} is consistent with previous reports making use of a two-band fitting procedure up to 15 T, and which has been physically mapped by self-consistent tight-binding calculations to the redistribution of sub-bands population under the effect of electronic correlations (see Ref. [122] for details).

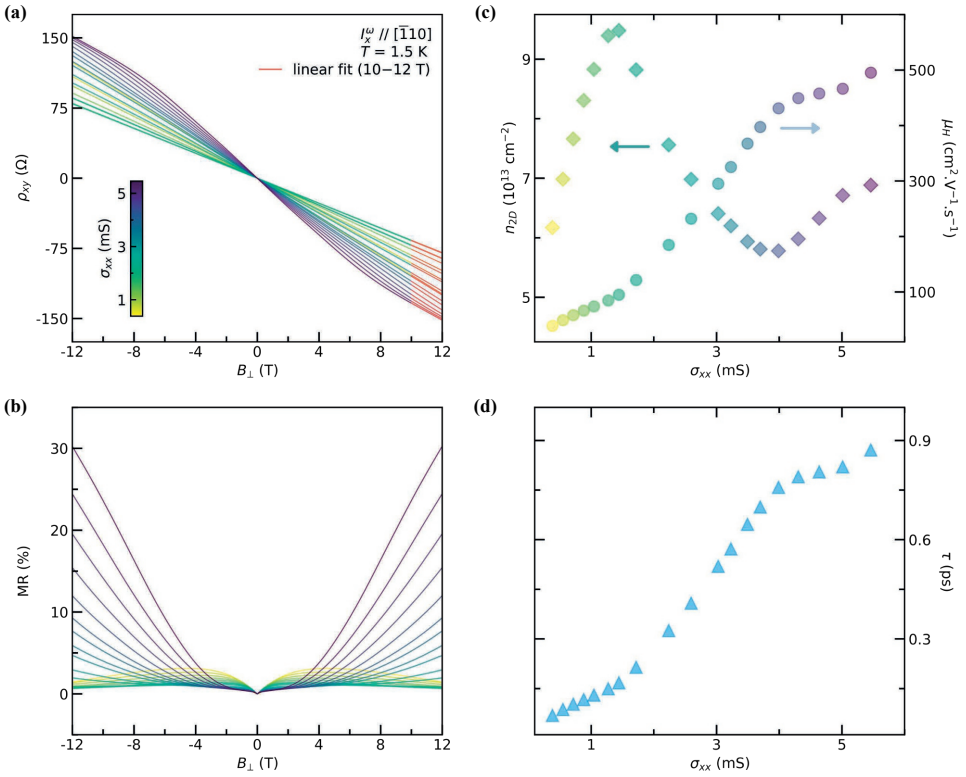

Figure 4.17: **Ordinary Hall effect and magnetoresistance of the 2DES. (a)** Gate-modulated ordinary Hall effect response of the 2DES for the current along [$\bar{1}$10]. Solid red lines are linear fits to $\rho_{xy}(B_\perp)$ performed between 10 and 12 T. **(b)** Corresponding longitudinal magnetoresistance. $B_\perp$, the out-of-plane magnetic field. **(c)** Experimentally estimated sheet carrier density n_{2D} (left axis) and electronic mobility μ_H (right axis) as a function of doping levels. **(d)** Momentum relaxation time τ versus sheet conductance σ_{xx}, obtained in a Drude model, following Eq. (4.49)

We estimate the momentum relaxation time $\tau_{(el)}$ [see Fig. 4.17(d)], within Drude's model, which in the quasi-d.c. limit ($\omega\tau \ll 1$) is given by:

$$\tau = \frac{\mu_H\, m^*}{e}, \tag{4.49}$$

where $m^* = \sqrt{m^*_{[\bar{1}\bar{1}2]} \cdot m^*_{[\bar{1}10]}}$ is the effective mass of the multi-orbital 2DES in the $SrTiO_3$[111] quantum well, with $m^*_{[\bar{1}\bar{1}2]} = 8.7m_e$ and $m^*_{[\bar{1}10]} = 1.1m_e$ [149], m_e the electron mass. The resulting calculated m^* is assumed to be gate- and temperature-independent.

A linear interpolation of the measured value of the momentum relaxation time τ vs. σ_{xx} allows to calculate the sheet conductance dependence of the BCD's magnitude D_x (shown in Fig. 4.5 **d**) following equation 4.1 of the main text.

4

ORDINARY HALL EFFECT & ESTIMATION OF THE MOMENTUM RELAXATION TIME – TEMPERATURE DEPENDENCE

Additionally, we also report the temperature dependence of the ordinary Hall effect and longitudinal MR of the 2DES, as shown in Fig. 4.18 (a),(b), respectively, for the Hall bar device oriented along [$\bar{1}$10]. Following the steps described above for the gate-dependent data set, we similarly extract the temperature dependence of the carrier density and electronic mobility [see Fig. 4.18 (c)], as well as that of the momentum scattering time [see Fig. 4.18 (d)]. Even though not shown here, we perform the same analysis for the orthogonal Hall bar device (*i.e.*, oriented along [$\bar{1}\bar{1}$2]) for experimentally measured data between 1.5 K and 30 K. These combined results, together with nonlinear Hall measurements with time-reversal symmetry, allow us to calculate the temperature dependence of the nonlinear conductivity tensor elements χ_{yxx} and χ_{xyy} [see Fig.4.5 **e** of the main manuscript], as well as the T-dependence of the Berry curvature dipole D_x [see Fig.4.5 **f** of the main manuscript].

ADDITIONAL DOPING-DEPENDENT HALL EFFECT MEASUREMENTS AND MAGNETOCONDUCTANCE IN THE WEAK ANTILOCALIZATION REGIME

We present in Fig. 4.19 (a,b) the gate-dependent ordinary Hall and longitudinal magnetoconductance data set collected for the Hall bar device oriented along the [$\bar{1}\bar{1}$2] direction. This allows the experimental estimation of total the carrier density (n_{2D}), Hall mobility (μ_H), momentum scattering time (τ_{el}), as well as inelastic and spin-orbit and scattering times (τ_i and τ_{so}, respectively) as a function of the 2DES' sheet conductance σ_{yy} ($I^\omega_y \parallel [\bar{1}\bar{1}2]$).

We refer the reader to the Methods sections of the main manuscript for details regarding the Hikami-Larkin-Nagaoka (HLN) model used to fit [see Eq. (3)] the magnetoconductance curves in the weak-antilocalization regime [141, 142].

ESTIMATION OF THE CRITICAL MAGNETIC FIELD AND CORRESPONDING ZEEMAN ENERGY. COMPARISON WITH THE RASHBA SPIN-ORBIT ENERGY

On one hand, we establish a criterion for the determination of the 'critical' magnetic field, B^c, at which the transverse magnetoresponse in a planar magnetic field exceeds a given threshold value R^c_{xy} [shown in the legends of panels in Fig. 4.20 (a,c), respectively].

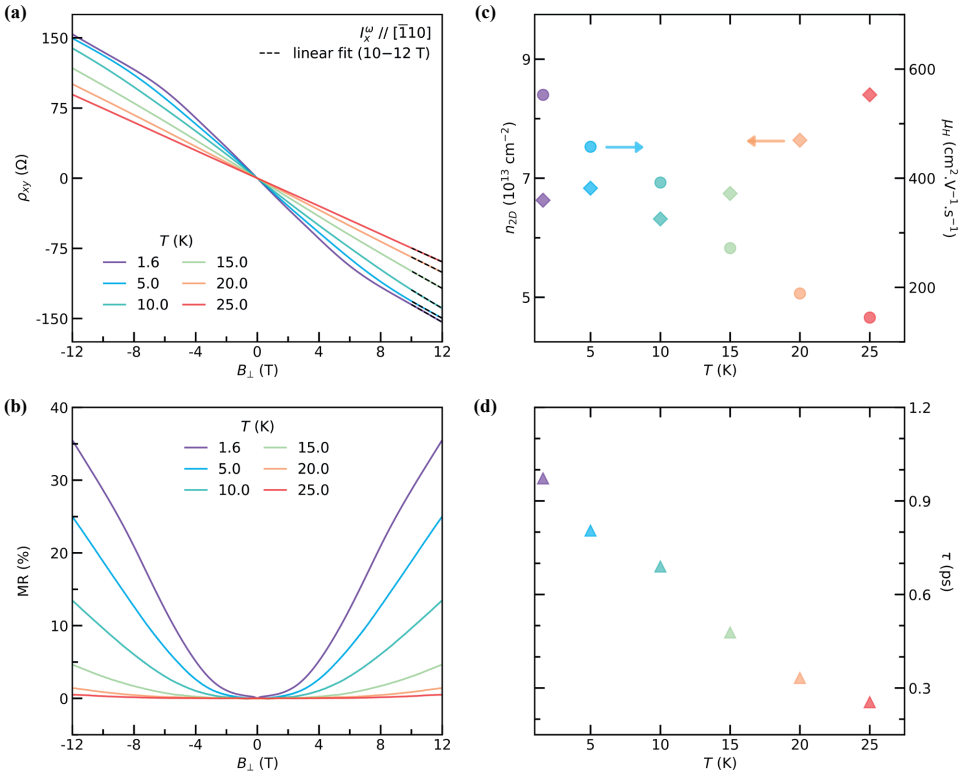

Figure 4.18: **Temperature dependent ordinary Hall effect and magnetoresistance of the 2DES. (a)** Temperature dependent Hall effect response of the 2DES for the current sourced along [$\bar{1}$10]. Dashed black lines are linear fits to $\rho_{xy}(B_\perp)$ performed between 10 and 12 T. **(b)** Corresponding longitudinal magnetoresistance. $B_\perp$, the out-of-plane magnetic field. **(c)** Experimentally estimated sheet carrier density n_{2D} (left axis) and electronic mobility μ_H (right axis) as a function of temperature. **(d)** Momentum relaxation time τ versus temperature T, obtained in a Drude model, following Eq. (4.49)

The corresponding effective Zeeman energy, at the in-plane field magnitude $B = B^c$, is given by:

$$\Delta_Z^c = \Delta_Z\left(B^c\right) = \frac{1}{2} g \mu_B B^c \,, \tag{4.50}$$

where $g = 2$ is the electron g-factor. In the main manuscript, we keep the criterion $R_{xy}^c \equiv \left|R_{xy}\right| \geq 6\ \Omega$ for the determination of B^c and Δ_Z^c, as shown in Extended Data Fig. 5.

On the other hand, assuming a D'yakonov-Perel' spin relaxation mechanism [150, 151], the Rashba spin-orbit energy is given by [142]:

$$\Delta_{so} = 2\alpha_R k_F \,, \tag{4.51}$$

with α_R the Rashba spin-orbit coupling (SOC) determined from WAL measurements (see Methods section), and k_F the electron wavevector at the Fermi energy.

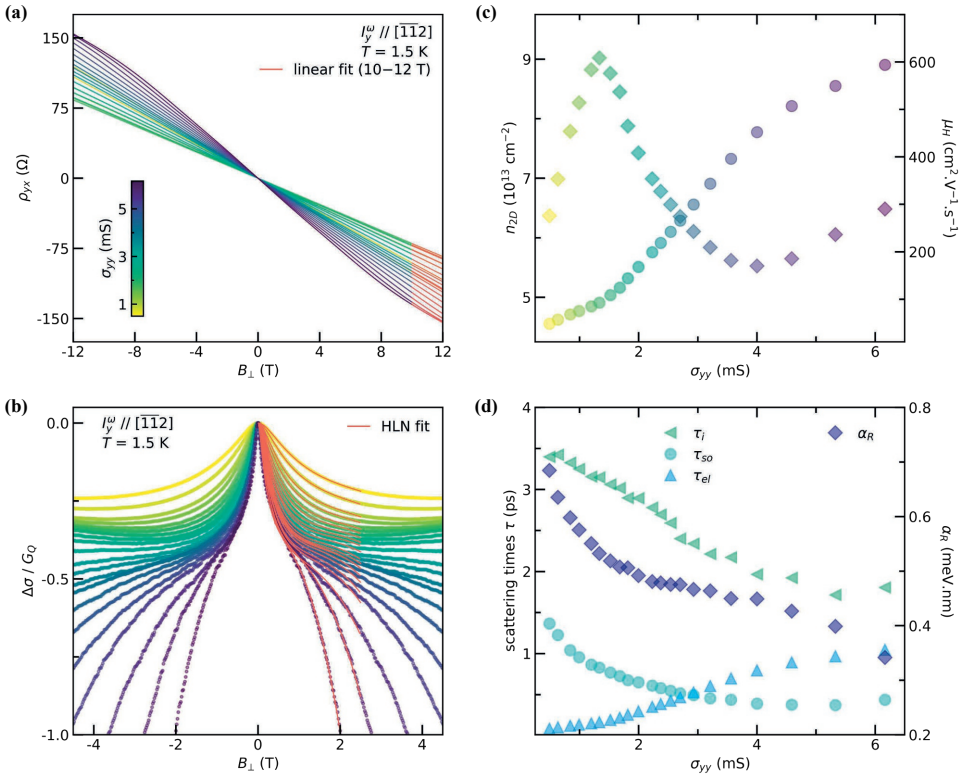

Figure 4.19: **Ordinary Hall effect and magnetoconductance in the WAL regime. (a)** Gate-modulated ordinary Hall effect response of the 2DES for the current sourced along [$\bar{1}\bar{1}$2]. Solid red lines are linear fits to $\rho_{yx}(B_\perp)$ performed between 10 and 12 T. **(b)** Corresponding magnetoconductance curves (normalized to the quantum of conductance G_Q) and fitted (solid red lines)using a Hikami-Larkin-Nagaoka model, following Eq. (3) from the main manuscript. $B_\perp$, the out-of-plane magnetic field. **(c)** Experimentally estimated sheet carrier density n_{2D} (left axis) and electronic mobility μ_H (right axis) versus sheet conductance σ_{yy}. **(d)** Left axis: Momentum, inelastic and spin-orbit relaxation times τ_{el}, τ_i and τ_{so}, as a function of σ_{yy}. Right axis: Strength of the Rashba spin-orbit coupling α_R *vs.* σ_{yy}.

OUT-OF-PLANE MISALIGNMENT OF THE PLANAR MAGNETIC FIELD

In order to experimentally estimate the value of the out-of-plane misalignment angle, γ, for the measurements displayed in Fig.4.4 (c,d) of the main manuscript, we conduct a low-field analysis of both the ordinary Hall and first-harmonic planar Hall effects as a function of doping levels for the same [$\bar{1}$10]−oriented Hall bar device.

Figs. 4.21 (a),(b) are magnified low-field views of the data set displayed in Fig. 4.17 (a) and Fig.4.3 (c) (see main text). We perform linear fits between ±2 T of the field-antisymmetrized out-of-plane $\rho_{xy}(B_\perp)$, and field-antisymmetrized in-plane $R_{xy}^{\omega}(B_\parallel)$ Hall magnetoresponses. The corresponding slopes are shown in Fig. 4.21 (c) and (d), respectively. The common dependence of both quantities as a function of σ_{xx} highlights their common origin. We hence attribute the linear contribution to $R_{xy}(B)$ in Fig. 4.4 (c) [here denoted: $R_{xy}^{\omega}(B_\parallel)$] at low-field to a spurious contribution of the ordinary Hall compo-

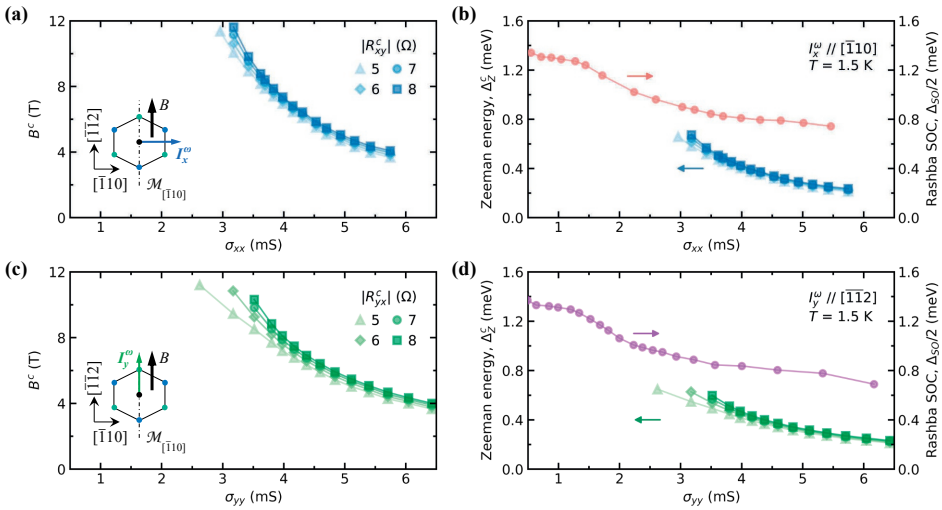

Figure 4.20: **Estimation of the critical magnetic field, corresponding Zeeman energy and comparison with the Rashba spin-orbit energy. (a)** Estimation of the critical field B^c corresponding to the onset of the planar Hall effect, for I^ω_x along [$\bar{1}$10]. **(b)**, Corresponding effective Zeeman energy Δ^c_Z at $B = B^c$ (left axis), and Rashba spin-orbit energy $\Delta_{so}/2$ (right axis) versus sheet conductance. (**c-d**) *Idem* for I^ω_y along [$\bar{1}\bar{1}$2].

nent due to a small out-of-plane magnetic field component: $\Delta B_\perp = B_\parallel \sin(\gamma)$, resulting from an imperfect coplanar alignment of the field with the plane of the 2DES. We denote this out-of-plane misalignment angle γ. The contribution ΔR^ω_{xy} to the planar Hall effect, from the conventional Hall effect due to this misalignment, is then expected to take the form: $\Delta R^\omega_{xy} = \frac{\delta\rho_{xy}}{\delta B_\perp} \cdot B_\parallel \sin(\gamma)$.

To further support this interpretation, we display in Fig. 4.22 the calculated quantity γ given by:

$$\gamma = \sin^{-1}\left(\frac{\delta R^\omega_{xy}/\delta B_\parallel}{\delta\rho_{xy}/\delta B_\perp}\right) \tag{4.52}$$

where the argument is the ratio of the low-field slopes from the in-plane and out-of-plane Hall effects. We indeed find that γ is independent of σ_{xx}, and consistently smaller than 1.5°. This misalignment amounts to an out-of-plane field component $\Delta B_\perp \leq 25$ mT at $B_\parallel = 1$ T.

Fig. 4.23 displays the change of longitudinal and transverse planar magnetoresponses, when deliberately imposing a small out-of-plane misalignment of the magnetic field (with tilt angle $\Delta\gamma$). We define $\gamma = 0°$ the angle at which the measurements displayed in Fig.4.3 of the main text were performed. Prior to any measurement campaign, we tentatively minimize γ by finding the tilt-angle which minimizes the low-field slope of $R^\omega_{xy}(B_\parallel)$, which is typically performed at low doping levels where the BCD-induced planar Hall contribution is absent.

As seen in Fig. 4.23 (a,c), we find that the planar longitudinal MR is extremely sensitive to a very small out-of-plane misalignment, changing by a factor of two within only one degree. This explains the relative magnitude discrepancies in the planar MR be-

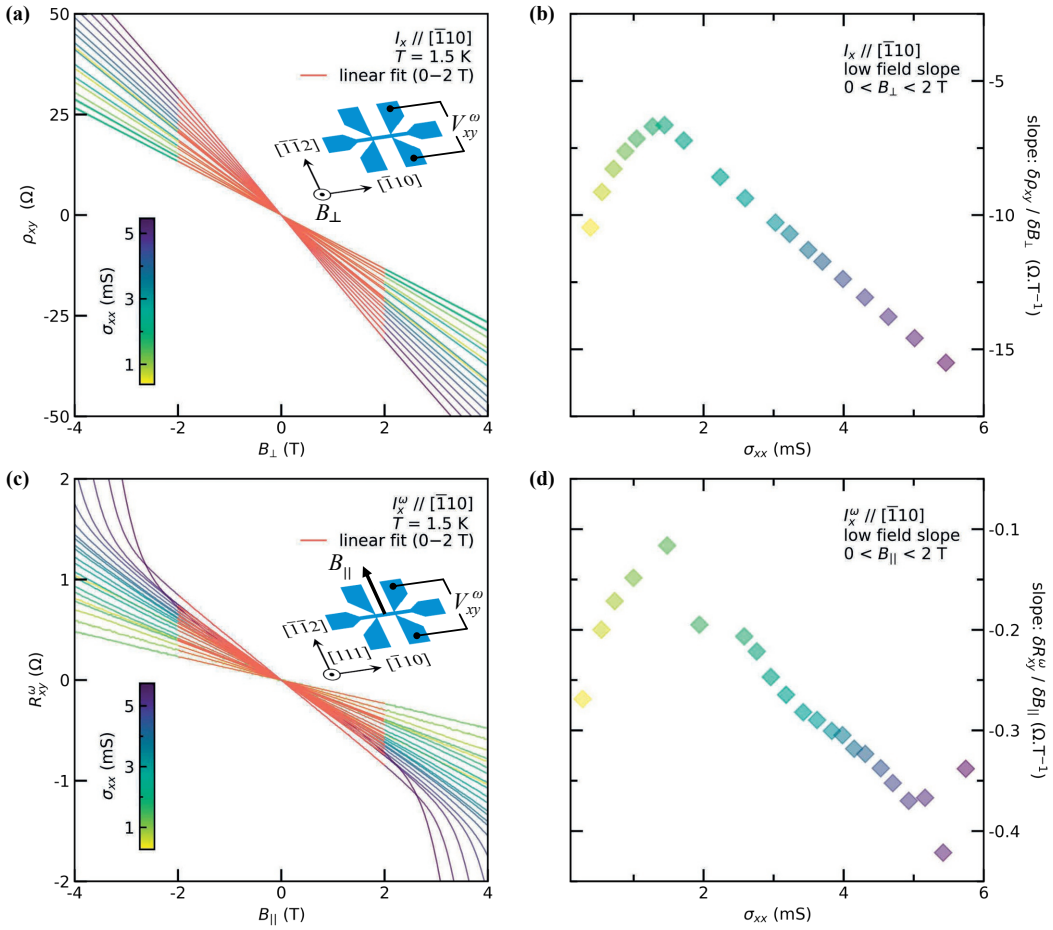

Figure 4.21: **Low-magnetic field linear fitting of ordinary Hall effect and first Harmonic planar Hall effect.** **(a)** Gate-modulated ordinary Hall effect response vs. $B_\perp$ of the 2DES for I_x along [$\bar{1}$10]. **(b)** Planar Hall response versus $B_\parallel$, the out-of-plane magnetic field. Solid red lines are linear fits performed between 0 and 2 T. **(c),(d)** Corresponding low-field slopes of $\rho_{xy}(B_\perp)$, and $R^{\omega}_{xy}(B_\parallel)$, respectively.

tween different cooldowns and measurements campaign. On the other hand, the planar Hall contribution is found to be relatively robust against small out-of-plane tilts of the magnetic field [see Fig.4.23 (b,d). The low-field slope R_{yx} is found to be proportional to $\Delta\gamma$, corroborating that it originates from a spurious conventional Hall component.

ANGULAR DEPENDENCE OF PLANAR MAGNETORESPONSES

We acquire the full in-plane angular dependence of the longitudinal magnetoresistance (MR) at $|B| = 12$ T, by sweeping the angle θ between the field and the current direction, in steps of 5°. Due to our mechanical rotator being limited to a 180° rotation range, we perform the rotation procedure twice, once for $B = +12$ T and a second time for $B = -12$ T, while keeping the sourced current and voltage probe contacts polarities unchanged.

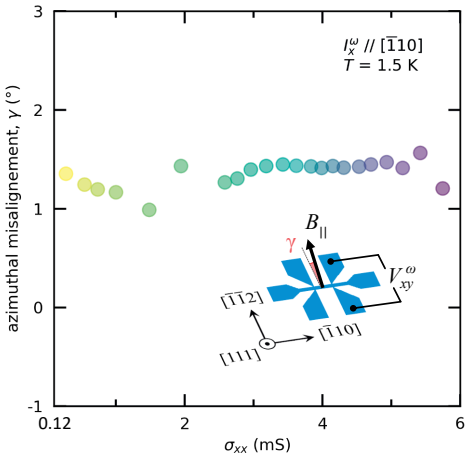

Figure 4.22: **Out-of-plane misalignment angle.** Experimentally estimated out-of-plane tilt value γ of the planar magnetic field, following Eq. (4.52), for the measurement of R_{yx} displayed in Fig. 2**c** (see main manuscript).

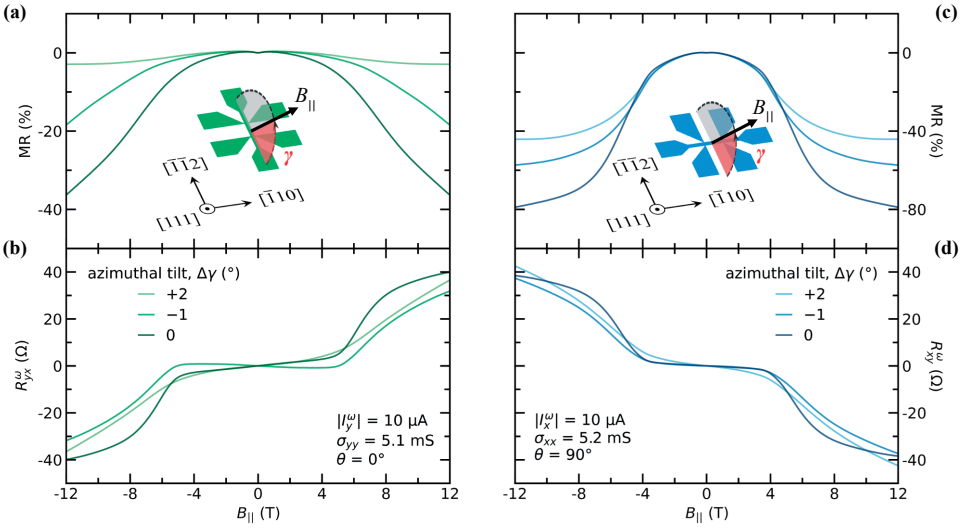

Figure 4.23: **Dependence of planar MR and planar Hall signals in a noncoplanar magnetic field.** Dependence of **(a)** the longitudinal MR, and **(b)** linear Hall response of the [$\bar{1}\bar{1}$2] device (≈ // B), for small out-of-plane deviations ($\Delta\gamma$) of the magnetic field. **(c)**,**(d)**, Idem with B perpendicular to I^ω sourced along [$\bar{1}$10] device. For both devices: while the linear planar Hall response is found to be quite insensitive to small $\Delta\gamma$ offsets, the quasi-planar MR shows a drastic change of magnitude upon small tilts of the magnetic field out-of-plane.

We can obtain the full field-symmetrized magnetoresistance at $|B| = 12$ T, as displayed in Fig. 4.24, by virtue of Onsager's relation: $\rho_{xx,yy}(B) = \rho_{xx,yy}(-B)$. The field-symmetric longitudinal magnetoresistance is then given by:

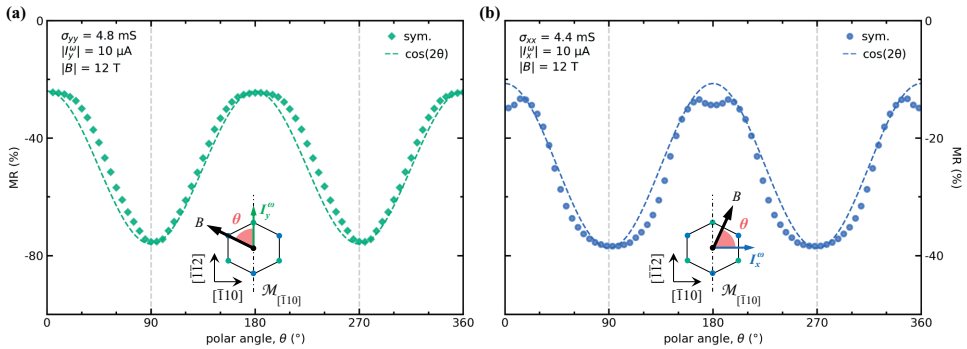

Figure 4.24: **Angular dependence of planar magnetoresistance.** Dependence of the field-symmetric planar magnetoresistance upon rotating a 12 T magnetic field within the sample's plane for **(a)** I_y^ω along $[\bar{1}\bar{1}2]$, and **(b)** I_x^ω along $[\bar{1}10]$; at a fixed sheet conductance value. θ is defined as the angle between the current bias direction and the external magnetic field. Dotted lines display the cos(2θ) dependence of the MR.

$$\mathrm{MR} = \frac{\rho_{\alpha\alpha}(B) + \rho_{\alpha\alpha}(-B)}{2\rho_{\alpha\alpha}(0)} - 1. \tag{4.53}$$

Whether the bias current is sourced along $\hat{\boldsymbol{y}} \parallel [\bar{1}\bar{1}2]$ or along $\hat{\boldsymbol{x}} \parallel [\bar{1}10]$, the planar MR follows the semiclassical cos(2θ) dependence, where θ is the relative angle between the current direction (along a principal crystal axis) and the planar magnetic field orientation.

Concomitantly, when measuring the planar transverse magnetoresponse, we observe that the field-symmetric contributions $R^{\mathrm{sym}}_{xy(yx)}$, of semiclassical origin (usually referred to as the 'planar Hall effect'), follows a sin(2θ) dependence, and goes to zero at $\theta = 0[\frac{\pi}{2}]$, as expected for a nonmagnetic system.

However, we find that the total transverse resistance $R^{\mathrm{tot}}_{\alpha\beta}$ (displayed in Fig. 2**f** of the manuscript) is dominated by the field-antisymmetric contribution (see Fig.4.25, $R^{\mathrm{as}}_{\alpha\beta}$, dubbed anomalous planar Hall effect" [99, 100], which remains finite whenever the external planar magnetic field is not orthogonal to the mirror line $\mathscr{M}_{[\bar{1}10]}$. Independent of whether the current is sourced along the $[\bar{1}10]$ or $[\bar{1}\bar{1}2]$ crystal axis directions, the transverse planar contribution vanishes in the linear response regime when the ($\mathscr{M}_{[\bar{1}10]}$-symmetry preserving) planar magnetic field is aligned with the $[\bar{1}10]$ direction (*i.e.* $\varphi = 0[\pi]$).

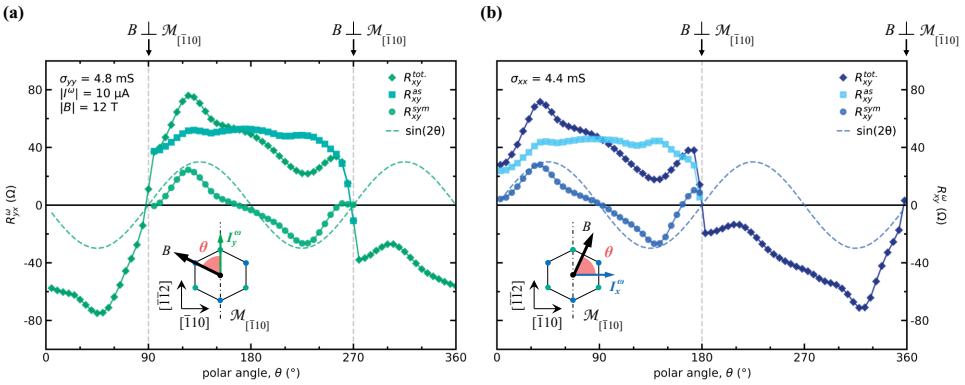

Figure 4.25: **Angular dependence of transverse magnetoresistance contributions.** Measured raw total signal $R^{\text{tot.}}_{\alpha\beta}$ at $|B| = 12$ T and the corresponding field-antisymmetric $R^{\text{as}}_{\alpha\beta}$ and field-symmetric $R^{\text{sym}}_{\alpha\beta}$ contributions for **(a)** I^{ω}_y along $[\bar{1}\bar{1}2]$, and **(b)** I^{ω}_x along $[\bar{1}10]$ at fixed electronic density. Remarkably, for both devices orientations, the semiclassical contribution to the planar Hall effect, *i.e.*, $R^{sym}_{\text{yx(xy)}}$, follows the expected $\sin(2\theta)$ dependence (highlighted by the dotted lines).

5

A RADIO-FREQUENCY STUDY OF SUPERCONDUCTIVITY AT THE (111)–ORIENTED LAO/STO INTERFACE

Here, we will present an comprehensive study on the superconducting properties of (111)-$LaAlO_3/SrTiO_3$ interface by using radio-frequency measurements. The interface shows interesting properties such coexistence of superconductivity and spin–orbit coupling in a honeycomb lattice structure. We show experimental results of two dimensional gas behaviour under external effect such as electric field and temperature by using microwave measurements. Then, we determine the behaviour of the superfluid density parameter and transition temperature directly calculated from the kinetic inductance of the resonator. From these measurements, we observe a violation of single band s-wave BCS superconductivity at (111)-LAO/STO interface.

5.1. INTRODUCTION

Almost a decade ago, a conductive interface was found in each crystallographic direction at LAO/STO interfaces [58]. The role of the orientation of the crystal in the properties of the two-dimensional electron gas were presented by Herranz *et al.* [13]. On the other hand, (111)-$LaAlO_3/SrTiO_3$ interfaces have attracted a lot of attention for showing a conductive interface at polar/polar layer combination with a hexagonal lattice symmetry. Previous studies showed that the interface hosts a superconducting two-dimensional electron gas and spin–orbit interaction [66, 67]. These studies have been conducted by traditional transport measurements, which are known to be limited in the exploration of a superconducting state under external effects. In this study, we will present the implementation of coplanar waveguide resonators at the interface itself of a (111)-LAO/STO material. We use superconducting coplanar resonators to conduct direct measurements of the superfluid density parameter. We measured the superconducting order parameters in a way that is beyond the traditional transport measurement scheme.

In this study, we drafted a design with multiple devices on a single sample in order to study the interface and obtain a unified picture. We placed traditional hall-bars next to the resonators which allow us to make measurements without changing the structure of the domain of the interface. The new design approach, involving conducting the transport and radio-frequency measurements on the same chip, performed concomitantly, can provide a unified picture of the characteristics of the superconducting ground state. For this study, a 9 unit cell (u.c.) LAO layer is grown on a TiO_2 terminated 5x5 mm $SrTiO_3$ crystal by using the PLD technique. The design details of the devices at the sample can be found in the following sections. Moreover, the fabrication techniques are explained in Chapter 2.

5.2. ELECTRICAL TRANSPORT MEASUREMENTS

In this section, we discuss the electronic transport measurements on the cleverleaf shaped device which is shown in Fig. 5.1 (a). The current-voltage measurements are conducted by using the four-probe technique. The current and the voltage leads are placed at the $[\bar{1}\bar{1}2]$ crystal direction. In order to check for any possible anisotropic behavior for (111)-LAO/STO complex oxides, we repeated the same measurements on the $[\bar{1}10]$ crystallographic directed device. We found that the transport measurement results are almost identical to the results presented in Fig. 5.1. We did not observe any anisotropic behavior between the two devices results.

In Fig. 5.1 (b), we present the $I-V$ curves of the presented device, from -45 to +30 voltage (V) range. No electrical hysteresis was observed at the ground state. The characteristics of a superconductor are clearly recognized by the zero resistance behaviour. These measurements were repeated from the superconducting to the insulating state in which the input is used to calculate the sheet resistance of the interface. Figure 5.1 (c) shows the normalized sheet resistance as a function of the temperature for the applied voltage range. The normalized resistance value is calculated by

$$R_N = \frac{R_s(T)}{R_s(T = 350mK)} \tag{5.1}$$

where $R_s(T = 350\ \text{mK})$ is the resistance of the interface at the insulating state. The critical temperature is defined based on the mid-value of the normalized resistance. The calculated T_c is found to be ≈ 125 mK and which is in agreement with a previous report on the (111)-LAO/STO interface [66]. In Figure 5.1 (d), we show T_c vs. V_{gate} for different bias currents to observe its impact on the critical temperature. It is observed that the application of a bias current has an effect only on the value of T_c. One of the key observations from the transport measurements is that T_c does not vanish in the depleted region, which is in contrast to the behaviour of the (001) interface. A similar behaviour was observed in the other device which was oriented along the [$\bar{1}$10] crystal direction. The critical temperature of the superconducting interface from transport and radio-frequency measurements is presented in a single figure for interested readers in Section 5.6.1.

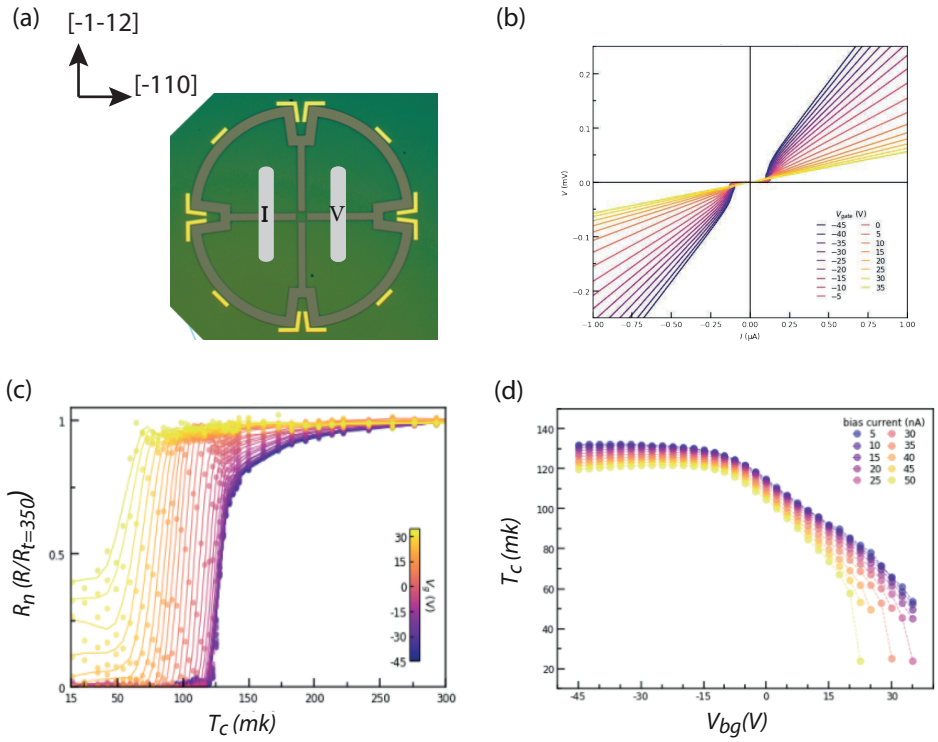

Figure 5.1: The DC-transport measurements. The I-V curves are measured at base temperature for [-45, +30] voltage range. (a) Optical image of cleverleaf van der pauw devices, the current-voltage leads are located at [-1-12] crystallographic direction. (b) I-V measurement for various gate voltages at base temperature. (c) Normalized Sheet resistance for the bias current 20 nA; the resistance value for each temperature is divided by resistance of the insulating state, *T=350 mK* as a function of temperature for various gate voltages. Inset: applied gate voltage range (d) The critical temperature is plotted as a function of gate voltage for various bias current.

5.3. EXPERIMENTAL DETAILS FOR RADIO-FREQUENCY MEASUREMENTS

The growth and fabrication methods for realizing devices at the (111)-LAO/STO complex oxide have been explained in Chapter 2. Here, we discuss the specifications of the implemented radio-frequency resonators at the 9 u.c. sample interface. We have designed two resonators which have same geometrical parameters yet distinctive electrical boundary conditions. One of them is defined as a closed end $\lambda/2$ coplanar waveguide resonator that has a current-node and voltage anti-node (open to ground). The other one is a $\lambda/4$ resonator with current anti-node conditions – open end. These resonators are located in the sample in such a way that each input line is along a different crystal symmetry. We expect to obtain similar results since the interface does not show any anistropy for different symmetry which was udnerstood during transport measurements. The length of the resonators (L) is 1 mm, the width of the central conductor (W) is 40 um, and the spacing between the ground plane and the center conductor (S) is 40 um. The optical image of the closed-end resonator is presented in Fig. 5.2 (c). In the present work, we will focus on the results of the closed-end resonator, though the results from the open-end resonator are displayed in the supplementary information 5.6.4. It is important to mention that each device has its own ground plane in order to avoid cross-talk during the measurements. The frequency of the coplanar waveguide resonator is directly related to the capacitance and inductance as given by the fundamental equation

$$f = \frac{1}{2\pi\sqrt{(L * C)}}. \tag{5.2}$$

In the given configuration of the closed-end resonator, the capacitance is 77 pF and geometric inductance is 0.06 nH. The first experiments with the resonator showed that the fundamental frequency is around 70 MhZ with optimized power settings. The value of the total inductance for the first mode is approximately 60 nH, which is two orders of magnitude higher than the geometric inductance. In other words, the measured frequency is greatly affected by the kinetic inductance, which is a directly related to the kinetic energy of Cooper pairs. The measurement set-up and device packaging for this study is presented in detail in Chapter 2. For the characterization of the resonators and van der Pauw devices, we tailored a set-up which allows running the measurements in sequence. The RF measurements were executed using a vector network analyzer and an IVVI-rack (to provide an electric field). The incoming signal is sent to the dilution fridge with a series of attenuators, which is in total −48 dB, until it reaches the device under test. The reflected signal is sent back to the VNA by using a low frequency amplifier and a small amount of attenuation within the fridge set-up.

5.4. RESULTS

5.4.1. GATE DEPENDENCY OF THE RESONANCE FREQUENCY

The experimental configuration facilitates sending an electric field to the radio-frequency resonators at the interface. In this section, we will present the response of the resonator to electric field at the base temperature. As was explained in the previous section, Section 5.2, the two-dimensional electron system can be tuned without any impact of hys-

teresis on the sheet conductance value for the [-45, +30] voltage range. Therefore, during the course of the radio-frequency measurements, we applied the same range of voltage to the resonators. In Fig. 5.2 (d), we show the reflection response of the resonator at the base temperature for different gate voltages. The most clear response is seen by a fundamental mode which appears to be at 90 Mhz in the depleted region and shows a slight decrease trend as the bias voltage increases. In Fig. 5.2 (e), the evolution of the reflection spectrum of the first three modes across the entire range of voltages is presented for T = 14 mK. For all these modes, the frequency does not show any decreasing trend at high voltages, which is utterly different than the (001)-LAO/STO interface results in Chapter 3. The frequency parameter alters by 30% under the gating effect, which aligns with earlier transport results. Moreover, the frequency of the resonator shifts to lower values as carriers are added to the system.

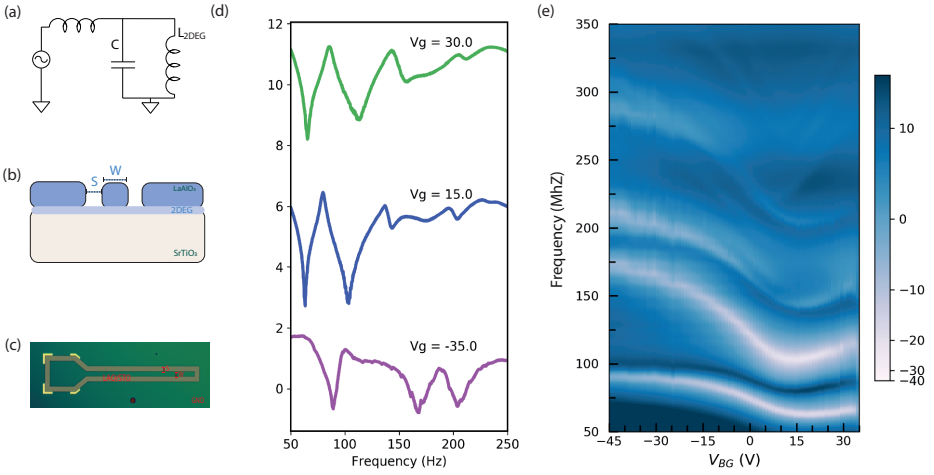

Figure 5.2: (a) Schematic circuit diagram of a radio-frequency resonator that is coupled to an input/output line. The first inductance comes from Al-wire bonding of the device to the printed circuit board. The resonator device can be represented as an LC circuit where L is the total inductance, dominated by the kinetic inductance of the Cooper pairs - L_{2DEG}, C is the total geometric capacitance, C = 77 pF, which is defined by by the geometric parameters of the device. (b) Illustration of embedded resonators at (111)-LAO/STO interface. (c) Optical image of the device, gold-coated bonding pads, closed-end resonator and ground plane of the sample. The image was taken before the argon-etching step for enhanced visibility. (d) The frequency response of the fundamental resonator for three different values of the gate voltage, namely, $V_g = -35$ V, $V_g = 15$ V, and $V_g = 30$ V at T = 25 mK. In order to observe changes in resonance frequency value deterioration as an impact of gate voltage, the values of the resonators are shifted by 10 dB at 15 V and 30 V. (e) The radio-frequency reflection spectrum as a function of applied gate voltage at T = 25 mK.

5.4.2. BEHAVIOUR OF SUPERFLUID DENSITY WITH TEMPERATURE AND GATE VOLTAGE

In the previous section, we showed the gate tunable characteristics of the embedded resonators at the interface. In order to understand the behaviour of the superfluid density under the passage from the from superconducting to the insulating state, we conducted radio-frequency measurements as a function of both temperature and gate voltage. Here, we will present the results of these measurements and revisit the method of calculating n_s from the resonance frequency parameter. From an experimental point of view, we repeat the same measurement from 14 mK up to 120 mK with the same voltage range. The temperature of the sample puck was determined by previous calibration measurements. A description of the procedure for performing the analysis is given in the supplementary information 5.6.2. As we mentioned in chapter 1, the eigenvalues of the resonators f_{res} are the main input for the calculation of the superfluid density n_s, where the relation is

$$f_{res} = \frac{1}{2\ell} n_s \sqrt{\frac{wq^2}{2\epsilon_0(\epsilon_{eff}-1)m^*}} \tag{5.3}$$

where w stands for the width of the resonator, q for the charge of the electron, ϵ_0 is the relative permittivity of (111)-STO and ϵ_{eff} the effective permittivity, while m is the average electron mass. The electron mass is calculated based on the equation

$$m = 2m_e\sqrt{(m_{[\bar{1}10]} * m_{[\bar{1}\bar{1}2]})} \tag{5.4}$$

where $m_{[\bar{1}10]}$ is taken as 1.1 and $m_{[\bar{1}\bar{1}2]}$ is 8.7 for (111)-$SrTiO_3$ substrate or surface, based on Reference [63]. Another important parameter for the calculation of n_s from the RF measurements is the permittivity of the $SrTiO_3$ substrate. It is known that the dielectrict permittivity of STO changes as a function of the gate voltage. To take this into account, we performed calculations to understand the impact of a gate-dependent value of the permittivity on the superfluid density for (111)-oriented STO based on previous studies [87]. It is found that a field dependent ϵ_{sto} does not create a significant difference in the final results for the superfluid density, compared to the case where the value of ϵ_{sto} does not vary. For that reason, we continue to carry out the analysis with a constant value of the dielectric response, which is equal to ϵ = 19500 for the superconducting state [87]. However, the contribution of the variation of the dielectric constant to the superfluid density and other parameters are presented in supplementary information 5.6.3. In Fig. 5.3, we represent the frequency response (f_s) of the radio-frequency resonators for this range of voltages. We observe a flat response of the resonator in the depleted region for the entire superconducting state. Namely, removing electrons from the system does not have a big impact on the total Cooper pair density, which is different than the (001)-LAO/STO interface. On the contrary, as carriers are added to the system, the frequency decreases, as clearly seen in Fig. 5.3(a). Moreover, the frequency can decrease to one-half of its value as a result of additional carriers to 2DEG for the same temperature. These results show that a (111)-LAO/STO interface allows a distinctive electrostatic control of the superconductivity. As can be seen from Fig. 5.3, the extracted superfluid density is on the order of 10^{11} cm^{-2}, which is only a small portion of normal state carriers, 10^{13} cm^{-2} for this sample. The superfluid density numbers indicate that (111)-LAO/STO is

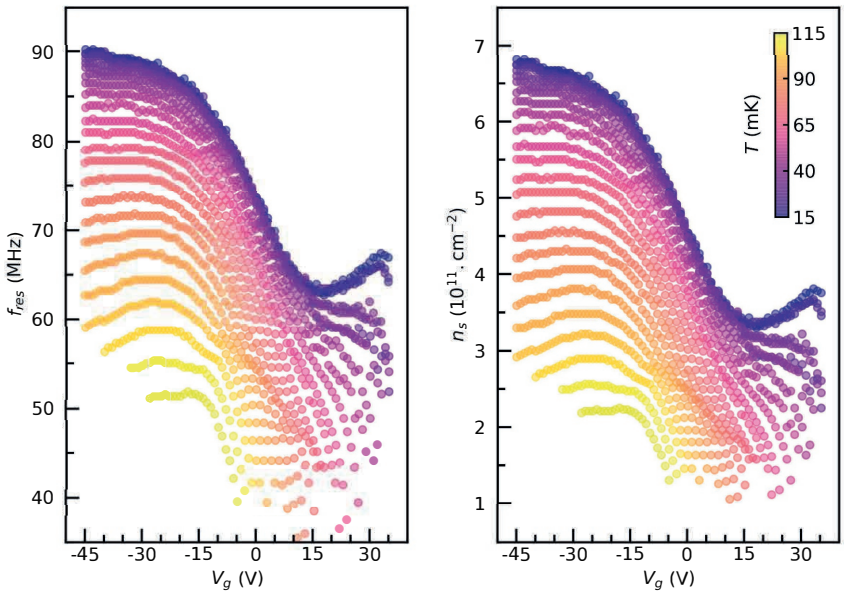

Figure 5.3: (a) The resonance frequency as a function of gate voltage for superconducting state. (b) The superfluid density (n_s) determined from the presented frequency responses which are presented on the left.Inset: The temperature range.

a very dilute superconductor due to fact only a very small portion of carriers enters the superconducting state. Fig. 5.3 (b) shows the (111)-LAO/STO interface can be diluted from 7x10^{11} to ≈ 1x10^{11} cm^{-2} by applying a gate voltage or increasing the temperature of the system. The n_s shows a non-monotonic behavior with the gate voltage, which was seen in previous studies of (001)-LAO/STO interface. Above 120 mK, no resonance dip has been detected, which indicates the critical temperature is approximately around 120 mK. On a different note, we would like mention that the upturn of the frequency at low temperatures might be related to the dielectric permittivity of the STO. Earlier experimental studies showed that the resonance frequency of the resonator increases at high doping in the insulating state, which is dominated by the STO substrate. In conclusion, we can confirm that radio-frequency resonators are reliable tools to investigate the superconducting state of complex heterointerfaces. The characteristic paramaters of a superconductor, such as the critical temperature and its relation with the carrier density, will be presented in the next section.

5.4.3. INDICATIONS OF A FAILURE OF THE SINGLE BAND BCS MODEL

In this section, we will take the data presented in the previous section as an input and implement them into a model whose results could allow us to classify the two-dimensional gas. The temperature dependence of the superfluid density, n_s (T) is a probe of the superconducting order parameter. Here, we will demonstrate the temperature dependence of n_s with the hope of shining light on the pairing mechanism at the (111)-LAO/STO interface. The model's predictions will show whether the superconductivity is based on the single electron band or multi electron band. For the calculations, the superfluid density can be used as a direct input for the clean s-wave BCS superconductors model as shown in this equation:

$$n_s(T) = n_0 \left[1 - \left(\frac{T}{T_c}\right)^{\gamma}\right], \tag{5.5}$$

where n_0 stands for the zero temperature superfluid density, T_c for the critical temperature, and γ for the global parameter in the equation for the Bardeen–Cooper–Schrieffer theory. During the analysis, we used the non-linear least squares method in order to fit the estimated superfluid density to the presented model. From the fitting procedure, we can have three different order parameters: T_c, n_o and γ, which reveal important information on the superconducting nature of a material. As a result of the calculations, we present n_s vs T for various gate voltages to understand the impact of the carrier density on the superconductivity. Fig. 5.4 (a) exhibits both the experimental (circles) and modelling (lines) results as a function of temperature for gate voltages. We found that the s-wave BCS model does fit well for the underdoped region, unlike the overdoped region, as can be seen from Fig. 5.4 (a). Even so, there is an agreement between the data and model for underdoped region, the outcome γ parameter value is not equal to two. the critical temperature is another findings of the model which is shown in Fig. 5.4 (b) right axis as a function of carrier doping. We observed the behaviour of T_c changes over the doping of the carriers. For instance, it slightly increases in the very low doping region (from -40V to -10 V) and does not show any quantum critical point (QCP). In particular, T_c does not fall to zero for high negative voltage, which indicates no observation of QCP. After -10 V, T_c changes its nature and decreases as carriers are added to system. The change in the behaviour of the transition temperature after a certain level of doping could be an indication of a second band population in the system. Although this may be true, we believe further studies would be necessary to understand the contributions of the bands to the superconductivity as a function of the gate voltage. There might be some reason other than the orbital ordering, such as inter–intra band scattering between bands, but our experimental findings are not sufficient to make a comment on this topic. We believe further theoretical and experimental studies could bring more understanding to the interpretation of the current results. Another fundamental characteristic for a superconductor is the zero temperature superfluid density n_0. Therefore, we represent the calculated n_0 as a function of the gate voltage in Fig. 5.4 (b) left axis. It decreases as a function of the carrier doping in the system. For the underdoped region, the zero temperature superfluid density is continually decreasing as carriers are added to the system, which is a behaviour different from that of the critical temperature. For the overdoped regime, the agreement between the data and the BCS model leads to huge error bars, as can be seen from Fig. 5.4 (c). The exponent γ in Eq. 5.5 can help to classify materials

into conventional or unconventional BCS superconductors. Fig. 5.4 (c) presents the calculated parameter as it varies as a function of the voltage bias. The model fit parameter γ should be equal to 2 for single-band s-wave superconductor. These results indicate that the superconducting gas at the interface has an unconventional behaviour. In the underdoped region, the value is equal to 3 and has fairly small error bars up to V_g=0. For the overdoped region, the value can go up to ≈ 4–5, which also presents very large error bars. This observation has been reproduced on an open-end resonator device, proving that the superconductivity at the interface is not contributed to only by the single band. The detailed findings are presented in the supplementary information 5.6.4 for interested readers. The normalized superfluid density as a function of temperature should fall on a single line to be considered as a single gap superconductor [30]. Previous studies on (001)-LAO/STO interfaces found the characteristics of the BCS model by finding a single line around the value of two for the pristine state. In contrast to an (001)-oriented interface, our results do not fall on a single line close to the value of two, as can be seen from Fig. 5.4 (d). We can confirm that no one of the devices (based on our experimental work) has shown a behaviour which falls on a single line.To elaborate, the value of gamma is shown for three distinctive values, 2, 3.5 and 5, to help us to classify the superconductivitiy. Most of the values lie between 3.5 and 5. From these results, we can only say that the two-dimensional gas at the (111)-LAO/STO interface is not a single band s-wave superconductor. These results imply that (111)-LAO/STO interfaces need further studies related to the mechanisms where they contribute to the superconductivity. We believe that further experimental and theoretical studies could supply the reasoning for the observed behaviour in these experiments.

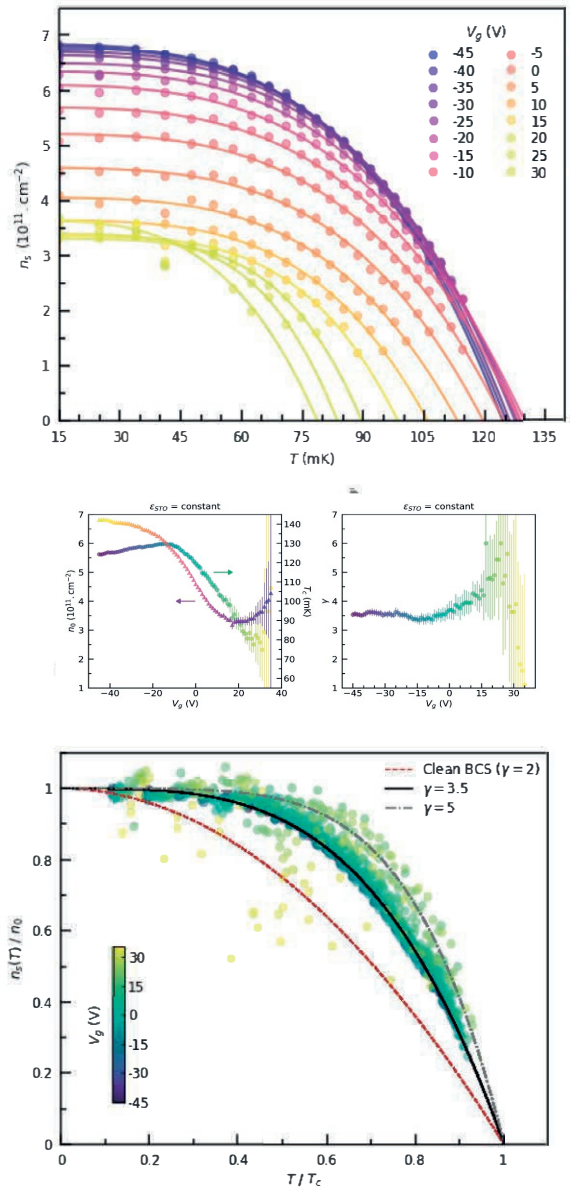

Figure 5.4: The predictions of the BCS model as a function of temperature and gate voltage. Top: Superfluid density vs temperature for every gate voltage from -45 V to +30 V with 5-volt intervals. Small circles represent the measurement data, solid lines the predictions of the single-band BCS model. Middle left: Superconducting critical temperature, T_c, (right axis) and zero temperature superfluid density (left axis), n_0, obtained from least squares fitting of the BCS model, Eq. 5.5. The large error bars for high positive voltages are an indication of a non-BCS scenario. Middle right: The gamma parameter vs gate voltage, γ starts from 3 in the underdoped region. The overdoped region shows huge error bars, indicating the disparity between the data and the predictions of the BCS model. Down: Normalized superfluid density vs. reduced temperature, calculated as a follow-up from above figure. A simulation (dotted lines) predicts the behavior of 'universal' lines for different values of gamma. Red line: case of γ=2, indicates clean s-wave superconductor. Black line (solid): the case of γ=3.5 where most of negative gate voltages fall on. Grey line: the case of γ=5, where positive voltages result in huge error bars. Note that these simulated lines are presented as a guide to the reader. All experimental data points stay above the red line.

5.5. DISCUSSION

Over the last decade, unconventional superconductivity for complex oxides has been studied from different perspectives. The multi-band superconductivity scenarios have been extensively studied and explained for LAO/STO hetero-structures where intra- and inter-band couplings play an important role in the supression [30, 78, 152, 27]. In addition, superconducting puddles have been discussed, where their distribution plays a role in the superconducting order parameters [153]. Studies regarding further explanations of the contributions of the different bands to the superconductivity at the newly discovered (111)-LAO/STO interface could be very interesting topic for future work, but is is not included in this thesis.

The possibility of tuning the two-dimensional electron gas with radio-frequency measurements opens up new possibilities to study fundamental issues for this quantum material. Oxide based coplanar waveguide resonators, with some degree of tunability, could find applications in the future (e.g., single photon detectors, actuators). In addition, the new design approach of conducting DC and RF-measurements on the same chip, performed concomitantly, can provide a unified picture of the nature of 2D superconductivity at thin films.

To our best knowledge, this is the first experimental study on superconductivity at the (111)-LAO/STO interface by using a radio-frequency resonator technique. We hope that this study will motivate other researchers to implement radio-frequency measurements for complex oxide materials.

5.6. SUPPLEMENTARY INFORMATION

5.6.1. THE CRITICAL TEMPERATURE FROM DC&RF MEASUREMENTS

Here, we will present the critical temperature as a function of the carrier doping, using both DC-transport and radio-frequency measurements. In order to provide a universal picture of the carrier doping, we calculate the sheet conductance from the transport measurement, as presented in Fig. 5.5. Subsequently, we combine the results for critical temperature from the electronic transport and radio-frequency measurements as a function of the sheet conductance. Due to having been able to measure both devices within same cooldown and after, we believe we didn't change the domain of the sample. This allows us to apply the correct gate voltage by ensuring no hysteresis in the system. As a matter of fact, the sample doping state stays the same, which provides more reliable results. In summary, we see that both measurement methods produce similar results, indicating that complex oxide interfaces can be studied by radio-frequency resonators. As can be seen from Fig. 5.5, both results provide very similar numbers as a function of the carrier density. As carriers are added to the system, T_c decreases until the saturation point. For the overdoped region,we observe the model is not correlating with data which results in huge error bars.

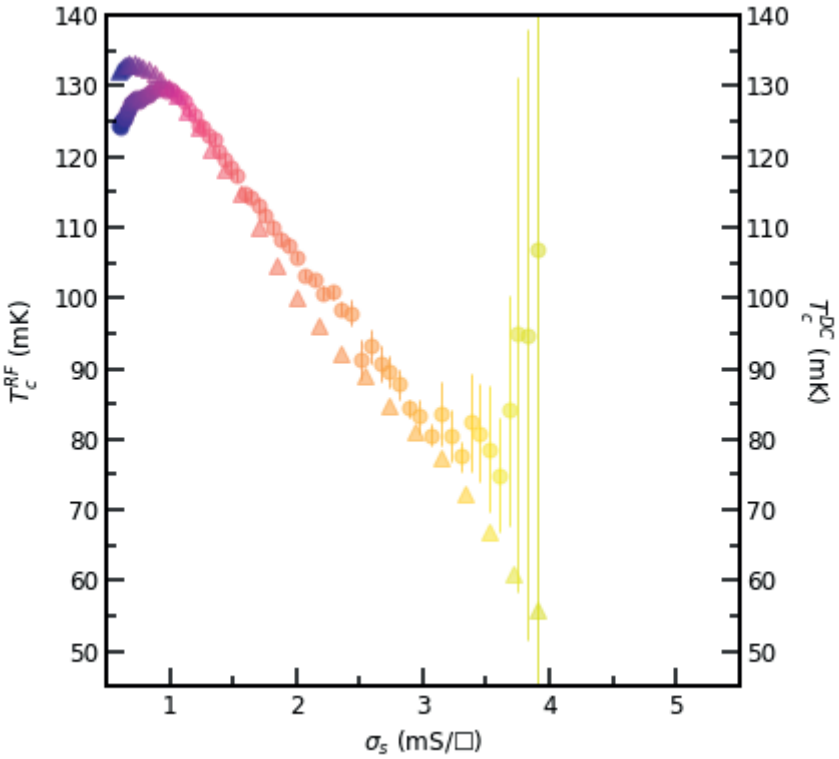

Figure 5.5: The critical temperature as a function of sheet conductance for DC-transport and radio-frequency measurements. The left axis stands for values from DC-transport - triangle shapes - , the the right axis - circle shape - for radio-frequency measurements. Both devices are located along the [$\bar{1}\bar{1}$2] direction on the sample. Inset: The calculation of sheet conductance is obtained from transport measurements.

5.6.2. CALCULATION OF RESONANCE FREQUENCY FROM REFLECTION SPECTRUM

In this study, the resonance frequency was directly measured from the experimental set-up via vector network analyzer. The reflected signal from the device carries additional signals until it reaches the output port. In order to get a responsive signal only from the two-dimensional electron gas, other contributing signals need to be excluded from the measured signal at the VNA. Here, we will explain the method which is used to find the correct values of the resonance frequency for each measurement point. Firstly, we will explain the method for subtracting the background to clean external contributors from the reflected signal. We assesed the magnitude of the contribution of the background by measuring the resonator response in the insulating state with the same input power as a function of the gate voltage. Later, we subtract this from each measured reflected signal S_{11} response of the superconducting state. We observed that this subtraction provides a clearer picture of the behaviour of resonators under the effect of a field.

The next step in the analysis is finding the correct value of the resonance from these cleaned data points. By using a peak finding function, we could access the resonance frequency of the fundamental mode for each gate voltage for all values of the temperature. This process is done automatically by defining the tolerance for the value of the bandwith, so no miscalculation is expected. The accuracy of the method can be easily seen in Fig. 5.6. The fundamental resonator frequesies are presented with blue dots in

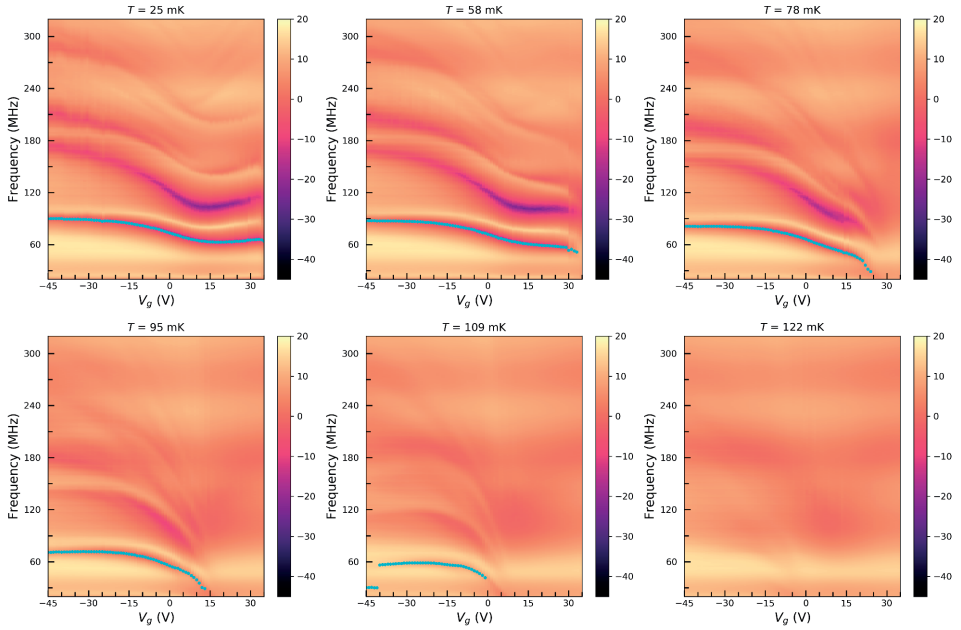

Figure 5.6: Reflected response of coplanar resonator under the effect of a field effect; a–f, 2D map of reflection spectrum for various temperatures from superconducting to insulating state. For $T = 122$ mK, the sample does not show any superconducting resonator response. Blue dots represent extracted resonance frequency values from resonance finding method (see main text).

two-dimensional maps of the parameter S_{11}(dB). There is good agreement between the experimental data and the extracted values, confirming that the peak finding method is a robust technique for analysing radio-frequency measurements.

5.6.3. THE IMPACT OF GATE-DEPENDENT PERMITTIVITY ON SUPERCONDUCTING ORDER PARAMETERS

As explained in the main text 5.4.2, the relative permittivity of the STO substrate plays an important role in the calculation of the superfluid density. Previous studies proved that ϵ_{STO} varies with varying the gate voltage bias or temperature. Therefore, it is important to consider the impact of the gate dependency of the dielectric constant in our analysis. Here, we will present an investigation where the dielectric permittivity is calculated as a function of the voltage bias.

Previous studies presented the permittivity of $SrTiO_3$ as a function of temperature and applied bias voltage for all crystallographic directions [39, 41] The value of the room temperature for the (111)-STO is reported to be 448 by Neville et al. [87]. In the same study, the relative permittivity as a function of the field effect was presented for all (111)–oriented STO crystal. In order to calculate the dielectric constant for a specific gate voltage value, the following equation can be used:

$$\frac{1}{\epsilon} l = A(T) + B(T)\,|E| \tag{5.6}$$

where A stands for 7.072 x 10^{-5} and B for 2.005 x 10^{-10} for temperatures below 4 K. Now, we will present the results where both cases are presented for the superfluid density, kinetic inductance and effective capacitance parameters. When the permittivty of STO is taken as a constant for the calculations, the magnitude of the superfluid density is slightly higher than the gate-dependent case, as can be seen in Fig. 5.7 (a). However, the trend of n_s does not show a deterioration. The same observation holds for the kinetic inductance results. On the contrary, for the effective capacitance, we observed the impact more clearly even though its magnitude is still negligible. These figures prove that a gate dependency has an impact on the values of the parameters for very low and high carrier densities. It is understood that the amount of variation amount is within acceptable limits (20%).

As a follow-up step, we calculated the superconducting parameters to observe any possible change due to the field dependency of the STO. In Fig. 5.8 (a), we present the results for T_c and n_0 when the dielectric constant is calculated as a function of the gate voltage. We observed the behavior of T_c and n_0 is almost identical compared to the case where ϵ is constant, which was presented in main text. Similarly, the fitting result for the parameter γ is around 3 for the underdoped region and increases with the gate voltage. From all parameters, the impact of a field dependency is mostly seen for n_0, which is $\approx$ 20% less than the case where ϵ is taken as constant. All things considered, these results show that the field dependency can have an impact on certain parameters but does not affect the main findings of the results of the radio-frequency measurements.

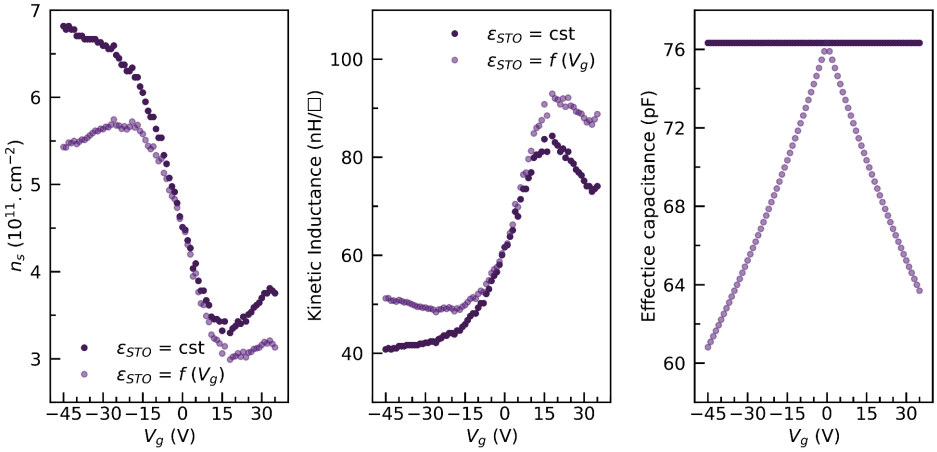

Figure 5.7: Calculations of parameters for constant and gate-dependent dielectric constant. (a) The zero-temperature superfluid density, dark circles stands for ϵ_{STO} is constant (=19500 V/C*m), light purple circle for gate-dependent $\epsilon_{(STO)}$ $T = 14$ mK. (b), (c) The kinetic inductance and the effective capacitance as functions of gate voltage range.

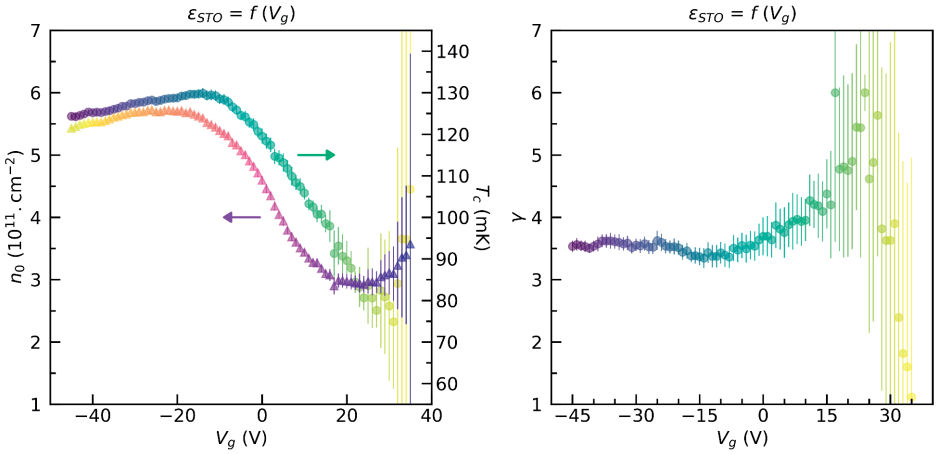

Figure 5.8: The superconducting state parameters as functions of gate voltage and temperature from the BCS-model fitting. For each measured gate voltage, the corresponding dielectric constant is input to the calculation of the superfluid density. (a) T_c, (b) n_o and (c) γ as functions of gate voltage.

5.6.4. SUPERCONDUCTING ORDER PARAMETERS FOR OPEN-END RESONATOR

Another radio-frequency resonator for the sample was placed along the [$\bar{1}$10] crystallographic direction, as shown in Fig. 5.9 (a). For the purpose of proving that there is no observed anisotropy at the (111)-LAO/STO interface, this device was placed along a different location than the closed-end resonator. Here, we will only show the results for the temperature and gate dependency of the superfluid density and other superconducting state parameters. In the main text, we explained the protocol to calculate T_c, n_o, and γ from the resonator response. For this study, we repeat the same measurements and protocol to avoid any contribution from experimental errors. In addition, the dielectric constant of the STO substrate was taken as a constant to be able to make a fair comparison with the results of the main text. It is found that all characteristic parameters react to the gate voltage in a similar way as for the closed-end resonator. To put it differently, gate tunable resonators at the complex oxide resonators provide very similar numbers for T_c, n_o and γ. At the same time, these analyses indicate there is an isotropy among distinct crystallographic directions, as observed in the DC-transport measurements.

As shown, we have experimentally demonstrated the results of a radio-frequency resonator from a different device at the 111-LAO/STO interface. The robustness of the radio-frequency resonator technique at the (111)-LAO/STO interface is shown by the fact that we obtain nearly equal results from two distinct devices.

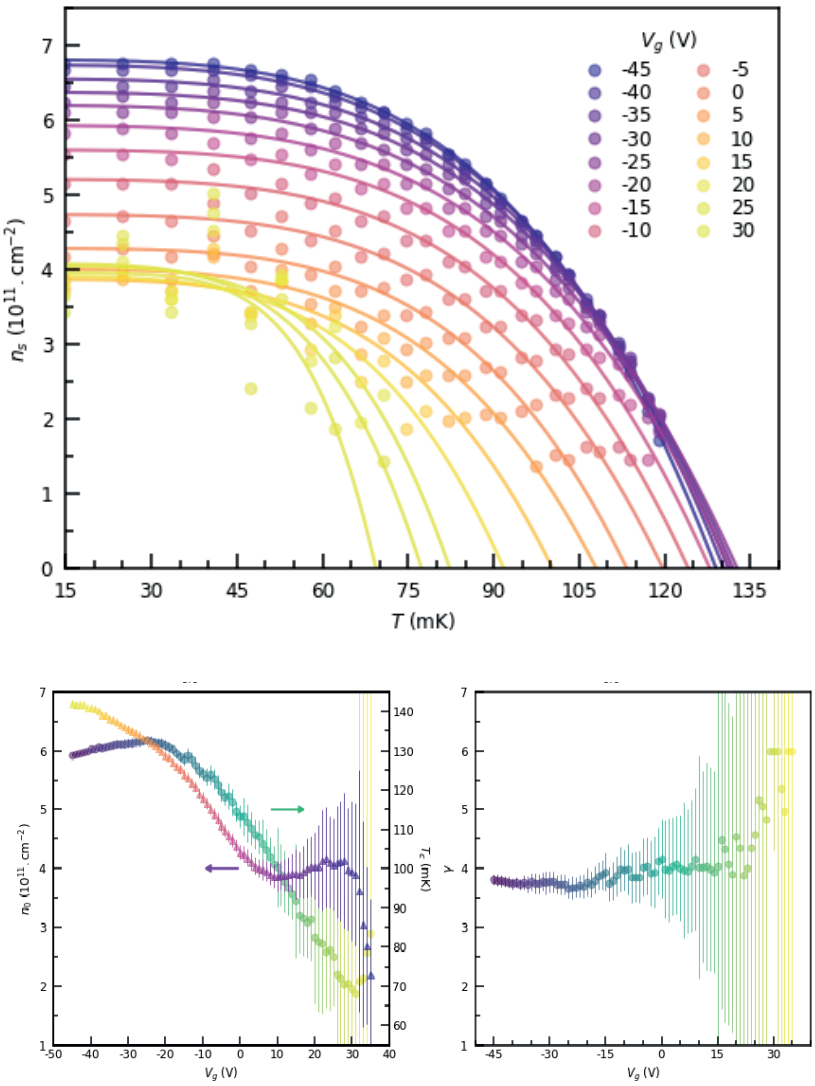

Figure 5.9: Superconducting state parameters resulting from BCS-model fitting. Top: Superfluid density as a function of temperature for various gate voltages. Down left: T_c and n_0 as functions of gate voltage. Down-right: The universal value of γ as a result of fitting a BCS single band model. The big error bars indicate the inadequacy of this modeling, which is seen more prominently as carriers are added to the system.

6

CONCLUSION

In this thesis, we presented studies on complex oxide interface by using different measurement techniques to explore their electrical and magnetic properties. We studied both the (001)-oriented and (111)-oriented LAO/STO complex oxides over the years. Here, I will summarize the main findings of each research study.

In Chapter 3, it was shown that the integration of superconducting coplanar waveguides at the (001)−LAO/STO interface. We observed with no application of an electric field, the temperature dependence of superfluid density is a good agreement with a clean s-wave BCS superconductor. When the system is under field effect both the critical temperature and the superfluid density show a dome-shaped phase diagram, leading to a multi-valued relationship between them. The comparison between transport data and cavity resonances suggests that the ground state of this 2DES is a Josephson junction array undergoing a transition between long- and short-range order under electrostatic doping. This study exhibits a new way of accessing for mapping the superconducting phase diagram of complex oxides.

In Chapter 4, it was reported the observation of sizable Berry curvature dipoles at complex oxide interfaces by a geometric design. the study uncovers a complex interplay between quantum confinement, spin-orbit coupling and crystal field along the (111) orientation of oxide heterostructures, bringing forth the appearance of a non-linear quantum Hall effect in time-reversal symmetric conditions with a large nonlinear transport response. This allows direct probing a geometric property of the occupied electronic states in complex systems with other competing ground states. In summary, it is reported fundamental finding of the coexistence of spin and orbital sources of Berry curvature in (111)-oriented LAO/STO system.

In Chapter 5, we designed embedded resonators at the interface of (111)-oriented LAO/STO interface which allowed us to map the superconducting phase diagram in a detection scheme that goes beyond traditional resistive measurements. In this study, we designed a new layout for conducting the DC-transport and radio frequency measurements on the same chip. This new design provides a unified picture of the nature of 2D superconductivity at the interface. In this study, we were able to investigate the superconducting order parameters behavior under the electric field for various temperatures.

We observe the two-dimensional electron gas at the interface can not be defined by single BCS-gap superconductors. The nature of the multiband nature of superconductivity can be explored by further possible research studies. We showed that the high-sensitivity probe technique can be implemented to oxide-based materials as a new pathway to study their fundamental properties. We hoped that oxide-based resonators could find applications in the future such as single photon detectors, and actuators. As we seen in Chapter 3 and Chapter 5, the coplanar waveguide resonators can be implemented to complex oxides in order to probe their fundamental properties.

BIBLIOGRAPHY

[1] Mariona Coll et al. “Towards oxide electronics: a roadmap”. In: *Applied surface science* 482 (2019), pp. 1–93.

[2] Bernhard Keimer et al. “From quantum matter to high-temperature superconductivity in copper oxides”. In: *Nature* 518.7538 (2015), pp. 179–186.

[3] M. Dawber, K. M. Rabe, and J. F. Scott. “Physics of thin-film ferroelectric oxides”. In: *Rev. Mod. Phys.* 77 (4 Oct. 2005), pp. 1083–1130.

[4] Elbio Dagotto. *Nanoscale phase separation and colossal magnetoresistance: the physics of manganites and related compounds*. Springer Science & Business Media, 2003.

[5] Ramaroorthy Ramesh and Nicola A Spaldin. “Multiferroics: progress and prospects in thin films”. In: *Nature materials* 6.1 (2007), pp. 21–29.

[6] Manuel Bibes, Javier E Villegas, and Agnès Barthélémy. “Ultrathin oxide films and interfaces for electronics and spintronics”. In: *Advances in Physics* 60.1 (2011), pp. 5–84.

[7] Tae Joon Park et al. “Complex oxides for brain-inspired computing: A review”. In: *Advanced Materials* (2022), p. 2203352.

[8] Amit Dey and Sudhakar Yarlagadda. “Oxides: An answer to the qubit problem?” In: *International Journal of Modern Physics B* 33.14 (2019), p. 1930003.

[9] A Ohtomo and HY Hwang. “A high-mobility electron gas at the LaAlO 3/SrTiO 3 heterointerface”. In: *Nature* 427.6973 (2004), pp. 423–426.

[10] Stefano Gariglio et al. “Superconductivity at the LaAlO3/SrTiO3 interface”. In: *Journal of Physics: Condensed Matter* 21.16 (2009), p. 164213.

[11] AD Caviglia et al. “Electric field control of the LaAlO 3/SrTiO 3 interface ground state”. In: *Nature* 456.7222 (2008), pp. 624–627.

[12] AD Caviglia et al. “Tunable Rashba spin-orbit interaction at oxide interfaces”. In: *Physical review letters* 104.12 (2010), p. 126803.

[13] Gervasi Herranz et al. “Engineering two-dimensional superconductivity and Rashba spin–orbit coupling in LaAlO 3/SrTiO 3 quantum wells by selective orbital occupancy”. In: *Nature communications* 6.1 (2015), pp. 1–8.

[14] DA Dikin et al. “Coexistence of superconductivity and ferromagnetism in two dimensions”. In: *Physical Review Letters* 107.5 (2011), p. 056802.

[15] Karen Michaeli, Andrew C Potter, and Patrick A Lee. “Superconducting and ferromagnetic phases in SrTiO 3/LaAlO 3 oxide interface structures: possibility of finite momentum pairing”. In: *Physical review letters* 108.11 (2012), p. 117003.

[16] Stefano Gariglio et al. “Interface superconductivity”. In: *Physica C: Superconductivity and its Applications* 514 (2015), pp. 189–198.

[17] Julie A Bert et al. “Direct imaging of the coexistence of ferromagnetism and superconductivity at the LaAlO3/SrTiO3 interface”. In: *Nature physics* 7.10 (2011), pp. 767–771.

[18] Holger Thierschmann et al. “Transport regimes of a split gate superconducting quantum point contact in the two-dimensional LaAlO3/SrTiO3 superfluid”. In: *Nature communications* 9.1 (2018), p. 2276.

[19] VV Bal et al. “Gate-tunable superconducting weak link behavior in top-gated LaAlO3-SrTiO3”. In: *Applied Physics Letters* 106.21 (2015), p. 212601.

[20] Jochen Mannhart and Darrell G Schlom. “Oxide interfaces—an opportunity for electronics”. In: *Science* 327.5973 (2010), pp. 1607–1611.

[21] J. Biscaras et al. “Two-Dimensional Superconducting Phase in $LaTiO_3/SrTiO_3$ Heterostructures Induced by High-Mobility Carrier Doping”. In: *Phys. Rev. Lett.* 108 (24 June 2012), p. 247004.

[22] Daniela Stornaiuolo et al. “Tunable spin polarization and superconductivity in engineered oxide interfaces”. In: *Nature materials* 15.3 (2016), pp. 278–283.

[23] S Hurand et al. “Josephson-like dynamics of the superconducting LaAlO 3/SrTiO 3 interface”. In: *Physical Review B* 99.10 (2019), p. 104515.

[24] D Valentinis et al. “Modulation of the superconducting critical temperature due to quantum confinement at the LaAlO 3/SrTiO 3 interface”. In: *Physical Review B* 96.9 (2017), p. 094518.

[25] RM Fernandes et al. “Two-band superconductivity in doped SrTiO 3 films and interfaces”. In: *Physical Review B* 87.1 (2013), p. 014510.

[26] G Venditti et al. “Nonlinear I- V characteristics of two-dimensional superconductors: Berezinskii-Kosterlitz-Thouless physics versus inhomogeneity”. In: *Physical Review B* 100.6 (2019), p. 064506.

[27] Thaıs V Trevisan, Michael Schütt, and Rafael M Fernandes. “Unconventional Multiband Superconductivity in Bulk SrTiO 3 and LaAlO 3/SrTiO 3 Interfaces”. In: *Physical review letters* 121.12 (2018), p. 127002.

[28] Christof W Schneider et al. “Microlithography of electron gases formed at interfaces in oxide heterostructures”. In: *Applied physics letters* 89.12 (2006), p. 122101.

[29] B Förg, Christoph Richter, and Jochen Mannhart. “Field-effect devices utilizing LaAlO3-SrTiO3 interfaces”. In: *Applied Physics Letters* 100.5 (2012), p. 053506.

[30] Julie A Bert et al. “Gate-tuned superfluid density at the superconducting LaAlO 3/SrTiO 3 interface”. In: *Physical Review B* 86.6 (2012), p. 060503.

[31] Beena Kalisky et al. “Critical thickness for ferromagnetism in LaAlO3/SrTiO3 heterostructures”. In: *Nature communications* 3.1 (2012), p. 922.

[32] Sumilan Banerjee, Onur Erten, and Mohit Randeria. “Ferromagnetic exchange, spin–orbit coupling and spiral magnetism at the LaAlO3/SrTiO3 interface”. In: *Nature physics* 9.10 (2013), pp. 626–630.

[33] AMRVL Monteiro et al. “Side gate tunable Josephson junctions at the LaAlO3/SrTiO3 interface”. In: *Nano letters* 17.2 (2017), pp. 715–720.

[34] D Stornaiuolo et al. “Signatures of unconventional superconductivity in the LaAlO 3/SrTiO 3 two-dimensional system”. In: *Physical Review B* 95.14 (2017), p. 140502.

[35] P. A. Fleury, J. F. Scott, and J. M. Worlock. “Soft Phonon Modes and the 110°K Phase Transition in $SrTiO_3$”. In: *Phys. Rev. Lett.* 21 (1 July 1968), pp. 16–19.

[36] K. A. Müller, W. Berlinger, and F. Waldner. “Characteristic Structural Phase Transition in Perovskite-Type Compounds”. In: *Phys. Rev. Lett.* 21 (12 Sept. 1968), pp. 814–817.

[37] Yun-Yi Pai et al. “Physics of SrTiO3-based heterostructures and nanostructures: a review”. In: *Reports on Progress in Physics* 81.3 (2018), p. 036503.

[38] CS Koonce et al. “Superconducting transition temperatures of semiconducting SrTi O 3”. In: *Physical Review* 163.2 (1967), p. 380.

[39] H-M Christen et al. “Dielectric properties of sputtered SrTiO 3 films”. In: *Physical Review B* 49.17 (1994), p. 12095.

[40] JF Schooley, WR Hosler, and Marvin L Cohen. “Superconductivity in Semiconducting SrTi O 3”. In: *Physical Review Letters* 12.17 (1964), p. 474.

[41] K Alex Müller and H Burkard. “SrTi O 3: An intrinsic quantum paraelectric below 4 K”. In: *Physical Review B* 19.7 (1979), p. 3593.

[42] Naoyuki Nakagawa, Harold Y Hwang, and David A Muller. “Why some interfaces cannot be sharp”. In: *Nature materials* 5.3 (2006), pp. 204–209.

[43] Stefan Thiel et al. “Tunable quasi-two-dimensional electron gases in oxide heterostructures”. In: *Science* 313.5795 (2006), pp. 1942–1945.

[44] Alexey Kalabukhov et al. “Effect of oxygen vacancies in the SrTiO 3 substrate on the electrical properties of the LaAlO 3/ SrTiO 3 interface”. In: *Physical Review B* 75.12 (2007), p. 121404.

[45] A. Fête et al. “Growth-induced electron mobility enhancement at the LaAlO3/SrTiO3 interface”. In: *Applied Physics Letters* 106.5 (2015).

[46] Claudia Cancellieri et al. “Influence of the growth conditions on the LaAIO3/SrTiO3 interface electronic properties”. In: *Europhysics letters* 91.1 (2010), p. 17004.

[47] Wolter Siemons et al. “Origin of charge density at LaAlO 3 on SrTiO 3 heterointerfaces: Possibility of intrinsic doping”. In: *Physical review letters* 98.19 (2007), p. 196802.

[48] Stefano Gariglio, M Gabay, and J-M Triscone. “Research Update: Conductivity and beyond at the LaAlO3/SrTiO3 interface”. In: *APL materials* 4.6 (2016), p. 060701.

[49] Nicolas Reyren et al. “Superconducting interfaces between insulating oxides”. In: *Science* 317.5842 (2007), pp. 1196–1199.

[50] AEM Smink et al. “Gate-Tunable Band Structure of the LaAlO 3- SrTi O 3 Interface”. In: *Physical review letters* 118.10 (2017), p. 106401.

[51] J Biscaras et al. “Two-dimensional superconducting phase in LaTiO 3/SrTiO 3 heterostructures induced by high-mobility carrier doping”. In: *Physical review letters* 108.24 (2012), p. 247004.

[52] E Maniv et al. “Strong correlations elucidate the electronic structure and phase diagram of LaAlO3/SrTiO3 interface”. In: *Nature communications* 6.1 (2015), p. 8239.

[53] Arjun Joshua et al. “A universal critical density underlying the physics of electrons at the LaAlO 3/SrTiO 3 interface”. In: *Nature communications* 3.1 (2012), pp. 1–7.

[54] M Ben Shalom et al. “Tuning spin-orbit coupling and superconductivity at the SrTiO 3/LaAlO 3 interface: a magnetotransport study”. In: *Physical review letters* 104.12 (2010), p. 126802.

[55] Zhicheng Zhong, Anna Tóth, and Karsten Held. “Theory of spin-orbit coupling at LaAlO 3/SrTiO 3 interfaces and SrTiO 3 surfaces”. In: *Physical Review B* 87.16 (2013), p. 161102.

[56] A Biswas et al. “Universal Ti-rich termination of atomically flat SrTiO 3 (001),(110), and (111) surfaces”. In: *Applied Physics Letters* 98.5 (2011), p. 051904.

[57] N Ramadass. “ABO3-type oxides—Their structure and properties—A bird’s eye view”. In: *Materials Science and Engineering* 36.2 (1978), pp. 231–239.

[58] Gervasi Herranz et al. “High mobility conduction at (110) and (111) LaAlO 3/SrTiO 3 interfaces”. In: *Scientific reports* 2 (2012), p. 758.

[59] David G Gonzalez et al. “First-principles modeling of conductivity at the (001),(110), and (111) SrTiO 3/LaAlO 3 heterointerfaces”. In: *Physical Review B* 104.15 (2021), p. 155306.

[60] Yin-Long Han et al. “Two-dimensional superconductivity at (110) LaAlO3/SrTiO3 interfaces”. In: *Applied Physics Letters* 105.19 (2014), p. 192603.

[61] Kalon Gopinadhan et al. “Gate Tunable In-and Out-of-Plane Spin–Orbit Coupling and Spin-Splitting Anisotropy at LaAlO3/SrTiO3 (110) Interface”. In: *Advanced Electronic Materials* 1.8 (2015), p. 1500114.

[62] Yin-Long Han et al. “Reconstruction of electrostatic field at the interface leads to formation of two-dimensional electron gas at multivalent (110) $LaAlO_3/SrTiO_3$ interfaces”. In: *Phys. Rev. B* 92 (11 Sept. 2015), p. 115304.

[63] TC Rödel et al. “Orientational tuning of the fermi sea of confined electrons at the SrTiO 3 (110) and (111) surfaces”. In: *Physical Review Applied* 1.5 (2014), p. 051002.

[64] Kyung Song et al. “Direct imaging of the electron liquid at oxide interfaces”. In: *Nature nanotechnology* 13.3 (2018), pp. 198–203.

[65] GM De Luca et al. “Symmetry breaking at the (111) interfaces of SrTiO 3 hosting a two-dimensional electron system”. In: *Physical Review B* 98.11 (2018), p. 115143.

[66] AMRVL Monteiro et al. “Two-dimensional superconductivity at the (111) LaAlO 3/SrTiO 3 interface”. In: *Physical Review B* 96.2 (2017), p. 020504.

[67] PK Rout, E Maniv, and Y Dagan. “Link between the Superconducting Dome and Spin-Orbit Interaction in the (111) LaAlO 3/SrTi O 3 Interface”. In: *Physical Review Letters* 119.23 (2017), p. 237002.

[68] AMRVL Monteiro et al. “Band inversion driven by electronic correlations at the (111) LaAlO 3/SrTiO 3 interface”. In: *Physical Review B* 99.20 (2019), p. 201102.

[69] Jiansong Gao. *The physics of superconducting microwave resonators*. California Institute of Technology, 2008.

[70] Koki Watanabe, Keiji Yoshida, and Takeshi Aoki Kohjiro. “Kinetic inductance of superconducting coplanar waveguides”. In: *Japanese journal of applied physics* 33.10R (1994), p. 5708.

[71] Hilary Noad et al. “Modulation of superconducting transition temperature in LaAlO 3/SrTiO 3 by SrTiO 3 structural domains”. In: *Journal of Superconductivity and Novel Magnetism* 32 (2019), pp. 821–825.

[72] Michelle Tomczyk et al. “Micrometer-Scale Ballistic Transport of Electron Pairs in $LaAlO_3/SrTiO_3$ Nanowires”. In: *Phys. Rev. Lett.* 117 (9 Aug. 2016), p. 096801. DOI: 10.1103/PhysRevLett.117.096801. URL: https://link.aps.org/doi/10.1103/PhysRevLett.117.096801.

[73] Nicola Manca et al. “Bimodal Phase Diagram of the Superfluid Density in LaAlO 3/SrTi O 3 Revealed by an Interfacial Waveguide Resonator”. In: *Physical review letters* 122.3 (2019), p. 036801.

[74] Cheng Cen et al. “Oxide nanoelectronics on demand”. In: *Science* 323.5917 (2009), pp. 1026–1030.

[75] M Diez et al. “Giant negative magnetoresistance driven by spin-orbit coupling at the LaAlO 3/SrTiO 3 interface”. In: *Physical review letters* 115.1 (2015), p. 016803.

[76] C Bell et al. “Dominant mobility modulation by the electric field effect at the LaAlO 3/SrTiO 3 interface”. In: *Physical review letters* 103.22 (2009), p. 226802.

[77] Srijit Goswami et al. “Quantum interference in an interfacial superconductor”. In: *Nature nanotechnology* 11.10 (2016), pp. 861–865.

[78] Gyanendra Singh et al. “Competition between electron pairing and phase coherence in superconducting interfaces”. In: *Nature communications* 9.1 (2018), pp. 1–8.

[79] MJ Lancaster, J Powell, and A Porch. “Thin-film ferroelectric microwave devices”. In: *Superconductor Science and Technology* 11.11 (1998), p. 1323.

[80] MPJ Tiggelman et al. “On the trade-off between quality factor and tuning ratio in tunable high-frequency capacitors”. In: *IEEE transactions on Electron Devices* 56.9 (2009), pp. 2128–2136.

[81] R Barends et al. “Niobium and tantalum high Q resonators for photon detectors”. In: *IEEE transactions on applied superconductivity* 17.2 (2007), pp. 263–266.

[82] Dejan Davidovikj et al. “Quantum paraelectricity probed by superconducting resonators”. In: *Physical Review B* 95.21 (2017), p. 214513.

[83] Martin Göppl et al. “Coplanar waveguide resonators for circuit quantum electrodynamics”. In: *Journal of Applied Physics* 104.11 (2008), p. 113904.

[84] O Copie et al. “Towards two-dimensional metallic behavior at LaAlO 3/SrTiO 3 interfaces”. In: *Physical review letters* 102.21 (2009), p. 216804.

[85] Ruslan Prozorov and Russell W Giannetta. “Magnetic penetration depth in unconventional superconductors”. In: *Superconductor Science and Technology* 19.8 (2006), R41.

[86] JP Carbotte. “Properties of boson-exchange superconductors”. In: *Reviews of Modern Physics* 62.4 (1990), p. 1027.

[87] RC Neville, B Hoeneisen, and CA Mead. “Permittivity of strontium titanate”. In: *Journal of Applied Physics* 43.5 (1972), pp. 2124–2131.

[88] Joachim Hemberger et al. “Electric-field-dependent dielectric constant and nonlinear susceptibility in SrTiO 3”. In: *Physical Review B* 52.18 (1995), p. 13159.

[89] CJ Lobb, David W Abraham, and M Tinkham. “Theoretical interpretation of resistive transition data from arrays of superconducting weak links”. In: *Physical Review B* 27.1 (1983), p. 150.

[90] J Biscaras et al. “Multiple quantum criticality in a two-dimensional superconductor”. In: *Nature materials* 12.6 (2013), pp. 542–548.

[91] Zhuoyu Chen et al. “The density and disorder tuned superconductor-metal transition in two dimensions”. In: *arXiv preprint arXiv:1807.08347* (2018).

[92] Edouard Lesne et al. “Designing spin and orbital sources of Berry curvature at oxide interfaces”. In: *Nature Materials* 22.5 (2023), pp. 576–582.

[93] F. D. M. Haldane. “Berry Curvature on the Fermi Surface: Anomalous Hall Effect as a Topological Fermi-Liquid Property”. In: *Phys. Rev. Lett.* 93 (20 Nov. 2004), p. 206602. DOI: 10.1103/PhysRevLett.93.206602. URL: https://link.aps.org/doi/10.1103/PhysRevLett.93.206602.

[94] Naoto Nagaosa et al. “Anomalous Hall effect”. In: *Rev. Mod. Phys.* 82 (2 May 2010), pp. 1539–1592. DOI: 10.1103/RevModPhys.82.1539. URL: https://link.aps.org/doi/10.1103/RevModPhys.82.1539.

[95] Di Xiao, Ming-Che Chang, and Qian Niu. “Berry phase effects on electronic properties”. In: *Rev. Mod. Phys.* 82 (3 July 2010), pp. 1959–2007. DOI: 10.1103/RevModPhys.82.1959. URL: https://link.aps.org/doi/10.1103/RevModPhys.82.1959.

[96] Haijun Zhang et al. “Topological insulators in Bi2Se3, Bi2Te3 and Sb2Te3 with a single Dirac cone on the surface”. In: *Nature Physics* 5.6 (2009), pp. 438–442. DOI: 10.1038/nphys1270. URL: https://doi.org/10.1038/nphys1270.

[97] Pan He et al. “Quantum frequency doubling in the topological insulator Bi2Se3”. In: *Nature Communications* 12.1 (2021), p. 698. DOI: 10.1038/s41467-021-20983-1. URL: https://doi.org/10.1038/s41467-021-20983-1.

[98] N. P. Armitage, E. J. Mele, and Ashvin Vishwanath. “Weyl and Dirac semimetals in three-dimensional solids”. In: *Rev. Mod. Phys.* 90 (1 Jan. 2018), p. 015001. DOI: 10.1103/RevModPhys.90.015001. URL: https://link.aps.org/doi/10.1103/RevModPhys.90.015001.

[99] Raffaele Battilomo, Niccoló Scopigno, and Carmine Ortix. “Anomalous planar Hall effect in two-dimensional trigonal crystals”. In: *Phys. Rev. Research* 3 (1 Jan. 2021), p. L012006. DOI: 10.1103/PhysRevResearch.3.L012006. URL: https://link.aps.org/doi/10.1103/PhysRevResearch.3.L012006.

[100] James H. Cullen et al. “Generating a Topological Anomalous Hall Effect in a Nonmagnetic Conductor: An In-Plane Magnetic Field as a Direct Probe of the Berry Curvature”. In: *Phys. Rev. Lett.* 126 (25 June 2021), p. 256601. DOI: 10.1103/PhysRevLett.126.256601. URL: https://link.aps.org/doi/10.1103/PhysRevLett.126.256601.

[101] Inti Sodemann and Liang Fu. “Quantum Nonlinear Hall Effect Induced by Berry Curvature Dipole in Time-Reversal Invariant Materials”. In: *Phys. Rev. Lett.* 115 (21 Nov. 2015), p. 216806. DOI: 10.1103/PhysRevLett.115.216806. URL: https://link.aps.org/doi/10.1103/PhysRevLett.115.216806.

[102] Carmine Ortix. “Nonlinear Hall Effect with Time-Reversal Symmetry: Theory and Material Realizations”. In: *Advanced Quantum Technologies* 4.9 (2021), p. 2100056. URL: https://doi.org/10.1002/qute.202100056.

[103] Z. Z. Du et al. “Band Signatures for Strong Nonlinear Hall Effect in Bilayer WTe_2”. In: *Phys. Rev. Lett.* 121 (26 Dec. 2018), p. 266601. DOI: 10.1103/PhysRevLett.121.266601. URL: https://link.aps.org/doi/10.1103/PhysRevLett.121.266601.

[104] Kaifei Kang et al. “Nonlinear anomalous Hall effect in few-layer WTe2”. In: *Nature Materials* 18.4 (Apr. 2019), pp. 324–328. ISSN: 1476-4660. DOI: 10.1038/s41563-019-0294-7. URL: https://doi.org/10.1038/s41563-019-0294-7.

[105] Su-Yang Xu et al. “Electrically switchable Berry curvature dipole in the monolayer topological insulator WTe2”. In: *Nature Physics* 14.9 (Sept. 2018), pp. 900–906. ISSN: 1745-2481. DOI: 10.1038/s41567-018-0189-6. URL: https://doi.org/10.1038/s41567-018-0189-6.

[106] Qiong Ma et al. “Observation of the nonlinear Hall effect under time-reversal-symmetric conditions”. In: *Nature* 565.7739 (Jan. 2019), pp. 337–342. ISSN: 1476-4687. DOI: 10.1038/s41586-018-0807-6. URL: https://doi.org/10.1038/s41586-018-0807-6.

[107] Sheng-Chin Ho et al. “Hall effects in artificially corrugated bilayer graphene without breaking time-reversal symmetry”. In: *Nature Electronics* 4.2 (Feb. 2021), pp. 116–125. ISSN: 2520-1131. DOI: 10.1038/s41928-021-00537-5. URL: https://doi.org/10.1038/s41928-021-00537-5.

[108] Raffaele Battilomo, Niccoló Scopigno, and Carmine Ortix. “Berry Curvature Dipole in Strained Graphene: A Fermi Surface Warping Effect”. In: *Phys. Rev. Lett.* 123 (19 Nov. 2019), p. 196403. DOI: 10.1103/PhysRevLett.123.196403. URL: https://link.aps.org/doi/10.1103/PhysRevLett.123.196403.

[109] Jhih-Shih You et al. “Berry curvature dipole current in the transition metal dichalcogenides family”. In: *Phys. Rev. B* 98 (12 Sept. 2018), p. 121109. DOI: 10.1103/PhysRevB.98.121109. URL: https://link.aps.org/doi/10.1103/PhysRevB.98.121109.

[110] Joolee Son et al. “Strain Engineering of the Berry Curvature Dipole and Valley Magnetization in Monolayer MoS_2”. In: *Phys. Rev. Lett.* 123 (3 July 2019), p. 036806. DOI: 10.1103/PhysRevLett.123.036806. URL: https://link.aps.org/doi/10.1103/PhysRevLett.123.036806.

[111] Yang Zhang et al. “Electrically tuneable nonlinear anomalous Hall effect in two-dimensional transition-metal dichalcogenides WTe 2 and MoTe 2”. In: *2D Materials* 5.4 (July 2018), p. 044001. DOI: 10.1088/2053-1583/aad1ae. URL: https://doi.org/10.1088/2053-1583/aad1ae.

[112] Dushyant Kumar et al. “Room-temperature nonlinear Hall effect and wireless radiofrequency rectification in Weyl semimetal TaIrTe4”. In: *Nature Nanotechnology* 16.4 (Apr. 2021), pp. 421–425. ISSN: 1748-3395. DOI: 10.1038/s41565-020-00839-3. URL: https://doi.org/10.1038/s41565-020-00839-3.

[113] O. Matsyshyn and I. Sodemann. “Nonlinear Hall Acceleration and the Quantum Rectification Sum Rule”. In: *Phys. Rev. Lett.* 123 (24 Dec. 2019), p. 246602. DOI: 10.1103/PhysRevLett.123.246602. URL: https://link.aps.org/doi/10.1103/PhysRevLett.123.246602.

[114] Sobhit Singh et al. “Engineering Weyl Phases and Nonlinear Hall Effects in T_d-$MoTe_2$”. In: *Phys. Rev. Lett.* 125 (4 July 2020), p. 046402. DOI: 10.1103/PhysRevLett.125.046402. URL: https://link.aps.org/doi/10.1103/PhysRevLett.125.046402.

[115] Jorge I. Facio et al. “Strongly Enhanced Berry Dipole at Topological Phase Transitions in BiTeI”. In: *Phys. Rev. Lett.* 121 (24 Dec. 2018), p. 246403. DOI: 10.1103/PhysRevLett.121.246403. URL: https://link.aps.org/doi/10.1103/PhysRevLett.121.246403.

[116] Yang Zhang, Yan Sun, and Binghai Yan. “Berry curvature dipole in Weyl semimetal materials: An ab initio study”. In: *Phys. Rev. B* 97 (4 Jan. 2018), p. 041101. DOI: 10.1103/PhysRevB.97.041101. URL: https://link.aps.org/doi/10.1103/PhysRevB.97.041101.

[117] Dennis Wawrzik et al. “Infinite Berry Curvature of Weyl Fermi Arcs”. In: *Phys. Rev. Lett.* 127 (5 July 2021), p. 056601. DOI: 10.1103/PhysRevLett.127.056601. URL: https://link.aps.org/doi/10.1103/PhysRevLett.127.056601.

[118] A. Ohtomo and H. Y. Hwang. “A high-mobility electron gas at the LaAlO3/SrTiO3 heterointerface”. In: *Nature* 427.6973 (Jan. 2004), pp. 423–426. ISSN: 1476-4687. DOI: 10.1038/nature02308. URL: https://doi.org/10.1038/nature02308.

[119] N. Reyren et al. “Superconducting Interfaces Between Insulating Oxides”. In: *Science* 317.5842 (Aug. 2007), pp. 1196–1199. DOI: 10.1126/science.1146006. URL: https://doi.org/10.1126/science.1146006.

[120] P. K. Rout, E. Maniv, and Y. Dagan. “Link between the Superconducting Dome and Spin-Orbit Interaction in the (111) $LaAlO_3/SrTiO_3$ Interface”. In: *Phys. Rev. Lett.* 119 (23 Dec. 2017), p. 237002. DOI: 10.1103/PhysRevLett.119.237002. URL: https://link.aps.org/doi/10.1103/PhysRevLett.119.237002.

[121] A. M. R. V. L. Monteiro et al. “Two-dimensional superconductivity at the (111)$LaAlO_3/SrTiO_3$ interface”. In: *Phys. Rev. B* 96 (2 July 2017), p. 020504. DOI: 10.1103/PhysRevB.96.020504. URL: https://link.aps.org/doi/10.1103/PhysRevB.96.020504.

[122] A. M. R. V. L. Monteiro et al. “Band inversion driven by electronic correlations at the (111) $LaAlO_3/SrTiO_3$ interface”. In: *Phys. Rev. B* 99 (20 May 2019), p. 201102. DOI: 10.1103/PhysRevB.99.201102. URL: https://link.aps.org/doi/10.1103/PhysRevB.99.201102.

[123] G. Herranz et al. “High mobility conduction at (110) and (111) LaAlO3/SrTiO3 interfaces”. In: *Scientific Reports* 2.1 (Oct. 2012), p. 758. ISSN: 2045-2322. DOI: 10.1038/srep00758. URL: https://doi.org/10.1038/srep00758.

[124] T. C. Rödel et al. “Orientational Tuning of the Fermi Sea of Confined Electrons at the $SrTiO_3$ (110) and (111) Surfaces”. In: *Phys. Rev. Applied* 1 (5 June 2014), p. 051002. DOI: 10.1103/PhysRevApplied.1.051002. URL: https://link.aps.org/doi/10.1103/PhysRevApplied.1.051002.

[125] C. Bareille et al. “Two-dimensional electron gas with six-fold symmetry at the (111) surface of KTaO3”. In: *Scientific Reports* 4.1 (2014), p. 3586. DOI: 10.1038/srep03586.

[126] Liang Fu. “Hexagonal Warping Effects in the Surface States of the Topological Insulator Bi_2Te_3”. In: *Phys. Rev. Lett.* 103 (26 Dec. 2009), p. 266801. DOI: 10.1103/PhysRevLett.103.266801. URL: https://link.aps.org/doi/10.1103/PhysRevLett.103.266801.

[127] Pan He et al. “Observation of Out-of-Plane Spin Texture in a $SrTiO_3$(111) Two-Dimensional Electron Gas”. In: *Phys. Rev. Lett.* 120 (26 June 2018), p. 266802. DOI: 10.1103/PhysRevLett.120.266802. URL: https://link.aps.org/doi/10.1103/PhysRevLett.120.266802.

[128] M. Trama et al. “Gate tunable anomalous Hall effect: Berry curvature probe at oxides interfaces”. In: *Phys. Rev. B* 106 (7 Aug. 2022), p. 075430. DOI: 10.1103/PhysRevB.106.075430. URL: https://link.aps.org/doi/10.1103/PhysRevB.106.075430.

[129] B. B. Kim et al. “Microscopic mechanism for asymmetric charge distribution in Rashba-type surface states and the origin of the energy splitting scale”. In: *Phys. Rev. B* 88 (2013), p. 205408.

[130] Maria Teresa Mercaldo et al. “Orbital design of Berry curvature: pinch points and giant dipoles induced by crystal fields”. In: *arXiv:2301.04548* (2023). DOI: 10.48550/ARXIV.2301.04548. URL: https://arxiv.org/abs/2301.04548.

[131] L. Rimai and G. A. deMars. “Electron Paramagnetic Resonance of Trivalent Gadolinium Ions in Strontium and Barium Titanates”. In: *Phys. Rev.* 127 (3 Aug. 1962), pp. 702–710. DOI: 10.1103/PhysRev.127.702. URL: https://link.aps.org/doi/10.1103/PhysRev.127.702.

[132] P. A. Fleury, J. F. Scott, and J. M. Worlock. “Soft Phonon Modes and the 110°K Phase Transition in $SrTiO_3$”. In: *Phys. Rev. Lett.* 21 (1 July 1968), pp. 16–19. DOI: 10.1103/PhysRevLett.21.16. URL: https://link.aps.org/doi/10.1103/PhysRevLett.21.16.

[133] M. Rössle et al. “Electric-Field-Induced Polar Order and Localization of the Confined Electrons in $LaAlO_3/SrTiO_3$ Heterostructures”. In: *Phys. Rev. Lett.* 110 (13 Mar. 2013), p. 136805. DOI: 10.1103/PhysRevLett.110.136805. URL: https://link.aps.org/doi/10.1103/PhysRevLett.110.136805.

[134] Lars Onsager. “Reciprocal Relations in Irreversible Processes. I.” In: *Phys. Rev.* 37 (4 Feb. 1931), pp. 405–426. DOI: 10.1103/PhysRev.37.405. URL: https://link.aps.org/doi/10.1103/PhysRev.37.405.

[135] Z. Z. Du et al. “Disorder-induced nonlinear Hall effect with time-reversal symmetry”. In: *Nature Communications* 10.1 (2019), p. 3047. DOI: 10.1038/s41467-019-10941-3. URL: https://doi.org/10.1038/s41467-019-10941-3.

[136] T. H. Kim et al. “Polar metals by geometric design”. In: *Nature* 533.7601 (2016), pp. 68–72. DOI: 10.1038/nature17628. URL: https://doi.org/10.1038/nature17628.

[137] Yang Zhang and Liang Fu. “Terahertz detection based on nonlinear Hall effect without magnetic field”. In: *PNAS* 118.21 (2021), e2100736118. ISSN: 0027-8424. DOI: 10.1073/pnas.2100736118. URL: https://doi.org/10.1073/pnas.2100736118.

[138] K. A. Müller and H. Burkard. “$SrTiO_3$: An intrinsic quantum paraelectric below 4 K”. In: *Phys. Rev. B* 19 (7 Apr. 1979), pp. 3593–3602. DOI: 10.1103/PhysRevB.19.3593. URL: https://link.aps.org/doi/10.1103/PhysRevB.19.3593.

[139] S. Thiel et al. “Tunable Quasi-Two-Dimensional Electron Gases in Oxide Heterostructures”. In: *Science* 313.5795 (2006), pp. 1942–1945. DOI: 10.1126/science.1131091. eprint: https://www.science.org/doi/pdf/10.1126/science.1131091.

[140] J. Biscaras et al. “Limit of the electrostatic doping in two-dimensional electron gases of LaXO3(X = Al, Ti)/SrTiO3”. In: *Scientific Reports* 4.1 (Oct. 2014), p. 6788. ISSN: 2045-2322. DOI: 10.1038/srep06788. URL: https://doi.org/10.1038/srep06788.

[141] Shinobu Hikami, Anatoly I. Larkin, and Yosuke Nagaoka. “Spin-Orbit Interaction and Magnetoresistance in the Two Dimensional Random System”. In: *Progress of Theoretical Physics* 63.2 (Feb. 1980), pp. 707–710. ISSN: 0033-068X. DOI: 10.1143/PTP.63.707. URL: https://doi.org/10.1143/PTP.63.707.

[142] Sadamichi Maekawa and Hidetoshi Fukuyama. “Magnetoresistance in Two-Dimensional Disordered Systems: Effects of Zeeman Splitting and Spin-Orbit Scattering”. In: *Journal of the Physical Society of Japan* 50.8 (1981), pp. 2516–2524. DOI: 10.1143/JPSJ.50.2516. URL: https://doi.org/10.1143/JPSJ.50.2516.

[143] Ryan Barnett, G. R. Boyd, and Victor Galitski. “SU(3) Spin-Orbit Coupling in Systems of Ultracold Atoms”. In: *Phys. Rev. Lett.* 109 (23 Dec. 2012), p. 235308. DOI: 10.1103/PhysRevLett.109.235308. URL: https://link.aps.org/doi/10.1103/PhysRevLett.109.235308.

[144] G. M. De Luca et al. “Symmetry breaking at the (111) interfaces of $SrTiO_3$ hosting a two-dimensional electron system”. In: *Phys. Rev. B* 98 (11 Sept. 2018), p. 115143. DOI: 10.1103/PhysRevB.98.115143. URL: https://link.aps.org/doi/10.1103/PhysRevB.98.115143.

[145] Neha Wadehra et al. “Planar Hall effect and anisotropic magnetoresistance in polar-polar interface of LaVO3-KTaO3 with strong spin-orbit coupling”. In: *Nature Communications* 11.1 (Feb. 2020), p. 874. DOI: 10.1038/s41467-020-14689-z. URL: https://doi.org/10.1038/s41467-020-14689-z.

[146] J. Biscaras et al. “Two-Dimensional Superconducting Phase in $LaTiO_3/SrTiO_3$ Heterostructures Induced by High-Mobility Carrier Doping”. In: *Phys. Rev. Lett.* 108 (24 June 2012), p. 247004. DOI: 10.1103/PhysRevLett.108.247004. URL: https://link.aps.org/doi/10.1103/PhysRevLett.108.247004.

[147] Arjun Joshua et al. “A universal critical density underlying the physics of electrons at the LaAlO3/SrTiO3 interface”. In: *Nature Communications* 3.1 (Oct. 2012), p. 1129. ISSN: 2041-1723. DOI: 10.1038/ncomms2116. URL: https://doi.org/10.1038/ncomms2116.

[148] Udit Khanna et al. “Symmetry and Correlation Effects on Band Structure Explain the Anomalous Transport Properties of (111) $LaAlO_3/SrTiO_3$”. In: *Phys. Rev. Lett.* 123 (3 July 2019), p. 036805. DOI: 10.1103/PhysRevLett.123.036805. URL: https://link.aps.org/doi/10.1103/PhysRevLett.123.036805.

[149] T. C. Rödel et al. “Orientational Tuning of the Fermi Sea of Confined Electrons at the $SrTiO_3$ (110) and (111) Surfaces”. In: *Phys. Rev. Applied* 1 (5 June 2014), p. 051002. DOI: 10.1103/PhysRevApplied.1.051002. URL: https://link.aps.org/doi/10.1103/PhysRevApplied.1.051002.

[150] M. I. D’Yakonov and V. I. Perel’. “Possibility of Orienting Electron Spins with Current”. In: *Soviet Journal of Experimental and Theoretical Physics Letters* 13 (June 1971), p. 467. URL: http://jetpletters.ru/ps/1587/article_24366.shtml.

[151] M.I. Dyakonov and V.I. Perel. “Current-induced spin orientation of electrons in semiconductors”. In: *Physics Letters A* 35.6 (1971), pp. 459–460. ISSN: 0375-9601. DOI: https://doi.org/10.1016/0375-9601(71)90196-4. URL: https://www.sciencedirect.com/science/article/pii/0375960171901964.

[152] Gyanendra Singh et al. “Gap suppression at a Lifshitz transition in a multi-condensate superconductor”. In: *Nature materials* 18.9 (2019), pp. 948–954.

[153] S Caprara et al. “Multiband superconductivity and nanoscale inhomogeneity at oxide interfaces”. In: *Physical Review B* 88.2 (2013), p. 020504.

CURRICULUM VITÆ

Yıldız Gözde SAĞLAM

24-10-1990 Born in Ankara, Turkey.

EDUCATION

2008–2013 Bachelors in Physics
Middle East Technical University, Ankara, Turkey

2013–2016 Masters in Mikro and Nanotechnology
Middle East Technical University, Ankara, Turkey

2016 Scientific Researcher
Leibniz Institute for Solid State and Material Research, Dresden, Germany

2016–2023 PhD. in Applied Physics
Delft University of Technology, Delft, The Netherlands
Thesis: A study of two-dimensional superconductivity at oxide interfaces using waveguide resonators
Promotor: Prof. dr. G. Steele , Dr. A. D. Caviglia

LIST OF PUBLICATIONS

2. Manca,N., Bothner, D. and Monteiro, A.MRVL and Davidovikj, D. and **Sağlam, Y.G.** et.al. *Bimodal Phase Diagram of the Superfluid Density in* $LaAlO_3/SrTiO_3$ *Revealed by an Interfacial Waveguide Resonator*, Physical Review Letters **122**, 036801 (2019).

1. Lesne, E., **Sağlam, Y.G.**, Battilomo, R. et al. *Designing spin and orbital sources of Berry curvature at oxide interfaces.* Nature Materials **22**, 576–582 (2023).

7

ACKNOWLEDGEMENTS

I would like to thank my supervisors Gary Steele and Andrea Caviglia for their support throughout my doctoral research journey. Gary, thank you very much for opening the doors of the microwave resonators and teaching me everything related to any subject from theory to practice, coding to cleanroom techniques, and many more. Your continuous support over the years made it possible to finalize the thesis, even though it took longer than we expected. I would like to thank you for giving me the opportunity to work with oxides and allowing me to work with many nice colleagues from the oxide community.

I thank the members of the doctoral committee for their time and valuable comments on my thesis. Over the course of years, I had an opportunity to work with many people from QN department and Kavli Nanolab Cleanroom, with whom our paths crossed along hallways. I would like to thank all of you since the research activities would not have been possible without your collaboration, especially during pandemic times.

My research projects involved two different subjects which brought challenges and benefits. I consider myself lucky to have been involved with two research groups over the years. I definitely owe thanks to those who help me pursue my experimental work in different laboratories. Since the list would be so long, I would like to shout out a big thank you to whomever I had a chance to work together in Steele and Caviglia lab. Yet, I would like to mention a few names which made an extensive contribution to my knowledge on experimental research. I would like to specially thank to Dr. Edouard Lesne, it was pleasure to work with you. Thank you very much for everything you teach me about complex oxides, measurement set-up and fruitful discussions on our research projects. Dr. Nicola Manca, thanks for being my mentor for the first six months of my phd and teach me the first tricks in the cleanroom. Felix, the guru of the cleanroom, thank you very much for answering all of my question and sharing your knowledge on resonators. I hope to see you one day in Germany and meet with your family again. Mark, your willingness to help was a true blessing for new students. I appreciate your effort to help whenever it was needed.

Away from work, my crew at Delft was an essential part of this journey. I am extremely grateful to have their continuous support over the years. Laura, thank you very much for always being there for me and all those amazing memories in the city of Delft.

I am so grateful to have you in my life and looking forward to sharing new moments. Ranko, my partner-in-crime in Rotterdam nights. I will always remember those nights as the highlight of my first years in the Netherlands. Your friendship made this journey easier, thanks for always believing me and motivating me till the end. Nikos, my Greek brother, there are many things to say about you but I will make it short. I always enjoyed our coffee breaks, lunches, and after-work dinners, barbeques and nice conversations. Andrea, thanks for being always open and supportive. I would like to say a big thank you to my Turk Gunu team. I had so many fun moments with you on many occasions. Rishabh, our conversations are always full of joy and inspiring moments. Thank you for being so kind and open.

There are few people in my world, who motivate me to start and finish this journey from far away. My dear Gokce, I can't thank you enough for everything over the last few years. It is time to create new memories in the city of Rotterdam. Osman, I could write hundreds of pages about you yet I need to make it short. I am deeply grateful for having your friendship over those years and thanks again for encouraging me all the time. Our phone calls made it possible to work on my Ph.D. Yucel, we share all the graduation moments from high school to doctorate. I am so happy that we can still walk together on the roads of life and be there for each other.

My dear Grazia, my sister from another mother... Everything started with one offer on that Friday night. I would not imagine that night would bring you to my life. I am deeply thankful to the universe for bringing you to my life. My life in Delft would not be the same without you.

Sevgili annecim ve babacim, bana sundugunuz her sey icin cok tesekkur ederim. Eger bugun buradaysam bu sizin bana olan inanciniz ve desteginiz sayesindedir. Iyi ki varsiniz. Sevgili ablacim, bu surecte ki en buyuk destekcim, senin bana gosterdigin destek olmasaydi bugun burada olmam mumkun bile olamazdi. Beni her zaman dinledigin icin cok tesekkur ederim.

And finally Swasti, you came to my life in the middle of this journey, and afterward, everything became better. You opened my eyes to a world in a way that I could not even imagine. I have enjoyed every step along the way with you. I would not be able to finish it if I did not have you next to me over the last few years. I am so looking forward to the next chapter of our lives and enjoying the "home" we created together. Love you.

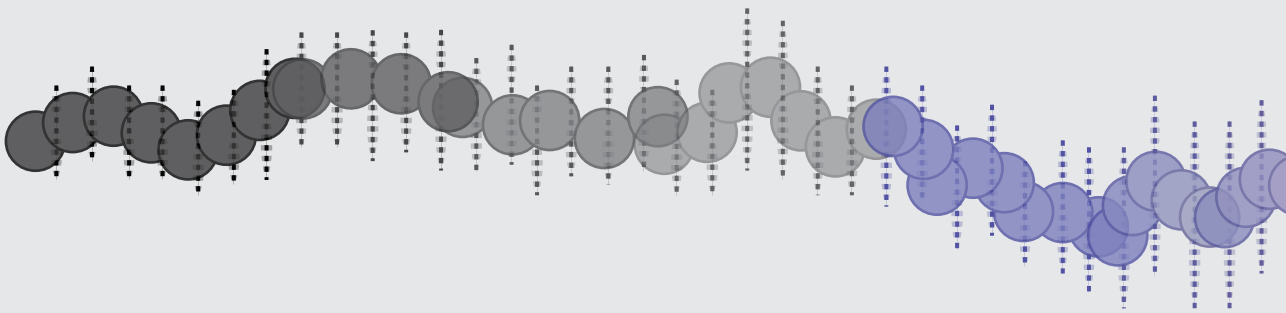

TU Delft

ISBN 978-94-6473-227-6